

Recovery and validation of Odin/SMR measurements of mesospheric CO and H₂O

FRANCESCO GRIECO

Department of Space, Earth and Environment
CHALMERS UNIVERSITY OF TECHNOLOGY
Gothenburg, Sweden 2020

THESIS FOR THE DEGREE OF LICENTIATE OF ENGINEERING

Recovery and validation of Odin/SMR measurements of mesospheric CO and H₂O

Francesco Grieco



Department of Space, Earth and Environment
CHALMERS UNIVERSITY OF TECHNOLOGY
Göteborg, Sweden 2020

Recovery and validation of Odin/SMR measurements of mesospheric CO and H₂O
FRANCESCO GRIECO

© FRANCESCO GRIECO, 2020.

Doktorsavhandlingar vid Chalmers tekniska högskola
Ny serie nr
ISSN 0346-718X

Department of Space, Earth and Environment
Chalmers University of Technology
SE-412 96 Göteborg, Sweden
Telephone + 46 (0) 31 – 772 1000

Cover: Number of scans in Odin/SMR CO L1 and L2 data sets, before and after the recovery, i.e. after the frequency correction that shifted the CO lines of many spectra to their theoretical center frequency, allowing to perform retrievals from scans that were previously discarded.

Typeset by the author using L^AT_EX.

Printed by Chalmers Reproservice
Göteborg, Sweden 2020

Abstract

Although life on Earth is concentrated in the troposphere, not only the processes happening here are of interest, since tropospheric processes are not the only ones that have an impact on the climate. Coupling mechanisms between different layers are such that changes in middle atmospheric dynamics and composition have an effect on what happens at lower altitudes. Therefore there is the need to extend climate models to include higher altitudes and to perform measurements of the middle atmosphere. Among the species that can be observed in the middle atmosphere, carbon monoxide (CO) and water vapour (H₂O) are of high scientific interest thanks to their aptness to being used as circulation tracers. This is due to their long photochemical lifetime which is longer or equal to zonal, meridional and vertical transport time scales. Moreover, H₂O plays a decisive role for O₃ chemistry. In the mesosphere, meridional circulation is driven by momentum deposition from breaking gravity waves. This originates an annual cycle which affects mostly high latitudes: with measurements it can be observed how CO-rich dry air descends towards the lower mesosphere at the winter pole while moist and CO-poor air is uplifted towards upper mesosphere and lower thermosphere at the summer pole. Gravity waves also give rise to the Semi-Annual Oscillation (SAO) in zonal winds resulting in concentration oscillations that can be observed in CO and H₂O measurements, mostly at the tropics. Among the satellite instruments currently performing remote sensing of the middle atmosphere, the Sub-Millimetre Radiometer (SMR) on board the Odin satellite is one of the most long-lived. In fact, SMR has been performing limb sounding of the middle atmosphere for 19 years, providing valuable long term datasets. However, the CO and H₂O datasets are both affected by instrumental artifacts that resulted in a misestimation of the two species' concentration. The two papers included in this thesis focus on identifying the causes and correcting such artifacts. CO observation modes were affected by a malfunctioning of the Phase-Lock Loop (PLL) of the local oscillator (LO) which was causing frequency shifts in the spectra and line broadening. An algorithm that shifts the line back to its theoretical position has been developed and the line broadening has been quantified and taken into account when performing new retrievals. Regarding the H₂O observation modes, underestimation of sideband leakage resulted in artifacts in the spectra that caused the misestimation of the retrieved concentration and temperature. For this reason SMR agreed poorly with other instruments measurements. An improvement was brought by assuming a larger sideband leakage than previously thought. For both species new inversions have been performed using the Optimal Estimation Method (OEM) with the Atmospheric Radiative Transfer Simulator (ARTS) as forward model. The recovery and correction of these products resulted in two new long-term and global data sets that are now available to the scientific community to study middle atmospheric dynamics.

Keywords: microwave limb sounding, mesosphere, CO, H₂O, recovery.

Acknowledgments

First of all, I would like to thank my supervisors Donal Murtagh and Kristell Pérot. To thank them properly would require an amount of text which would not be appropriate for a thesis. Here I limit myself to thanking them for their unwearying passion and dedication and for *always* finding the time to provide me with their support, as well as for their kindness and friendliness which have no equal.

Thanks to Patrick Eriksson for his contribution to the supervision of my work, and for his precious guidance in the use of ARTS. Thanks to Bengt Rydberg and Joakim Möller from Molflow for their readiness in providing assistance with issues in processing Odin/SMR data.

Finally, I would like to thank my family and friends, both old and new, for their endless care without which no goal whatsoever would ever be accomplished.

Francesco Grieco
Göteborg, September 2020

List of Publications

This thesis is based on the following appended papers:

- Paper 1.** Francesco Grieco, Kristell Pérot, Donal Murtagh, Patrick Eriksson, Peter Forkman, Bengt Rydberg, Bernd Funke, Kaley A. Walker, and Hugh C. Pumphrey. *Recovery and validation of Odin/SMR long term measurements of mesospheric carbon monoxide*. Atmos. Meas. Tech., 13, 1-20, <https://doi.org/10.5194/amt-13-1-2020>, accepted, 2020.
- Paper 2.** Francesco Grieco, Kristell Pérot, Donal Murtagh, Patrick Eriksson, Bengt Rydberg, Bernd Funke, and Kaley A. Walker. *Improvement of Odin/SMR water vapour measurements and validation of the obtained dataset*. Manuscript in preparation.

Contents

Abstract	iii
Acknowledgments	v
List of Publications	vii
 I	
Introductory chapters	1
 1	3
Introduction	
1.1 The middle atmosphere	5
 2	
Middle atmospheric chemistry and dynamics: their effect on CO and H₂O distributions	7
2.1 CO and H ₂ O chemistry	7
2.2 Middle atmospheric dynamics	9
 3	
The instrument	13
3.1 Measurement techniques of the middle atmosphere	13
3.2 Odin/SMR	14
3.3 Calibration process	17
3.4 Technical issues related to CO and H ₂ O datasets	19
 4	
Retrieval process	21
4.1 Line broadening	21
4.2 The inverse problem	23
 5	
Summary of appended papers and future outlook	25
5.1 Paper 1	25
5.2 Paper 2	26
5.3 Future outlook	26
 Bibliography	27

II	Appended papers	29
1	Recovery and validation of Odin/SMR long term measurements of mesospheric carbon monoxide	31
2	Improvement of Odin/SMR water vapour measurements and validation of the obtained dataset	53

Part I

Introductory chapters

Chapter 1

Introduction

The Earth's atmosphere can be divided into altitude regions according to different criteria. A common way to do this is to divide the atmosphere in regions characterised by different temperature gradients, with divisions placed in correspondence of reversals of the gradient (Brasseur and Solomon, 2005). Thus four layers are defined, from bottom to top: troposphere, stratosphere, mesosphere and thermosphere (see Figure 1.1). The troposphere ranges from the surface to about 8 km at the poles and to about 17 km at the equator. This layer is characterised by a negative vertical temperature gradient of -6.5 K/km to reach 200 K at the equator and 230 K at the summer pole. These temperatures are reached in correspondence of the tropopause, i.e. where the gradient reverses. On top of it there is the stratosphere which extends up to 50 km altitude. There, the temperature increases with altitude due to the absorption of ultraviolet solar radiation by the ozone layer, which makes up 90% of all ozone present in the atmosphere. At 50 km is the stratopause and above it there is the mesosphere where temperature decreases with altitude by about 3 ± 1 K/km. Minimum temperature is reached at the mesopause which is observed at different altitudes depending on the location: 95 km at the equator, with a minimum temperature of 170 K; 88 km at the summer pole with temperature 130 K. The uppermost layer is the thermosphere where the temperature increases rapidly with altitude to reach temperatures above 1500 K. Here gas density is so low and collisions so infrequent that the species are distributed within different altitudes based on their atomic weight. Moreover, in the thermosphere, energetic ultraviolet and X-ray photons from the sun are responsible for ionisation and dissociation of molecules. Thus, the constituents are mainly atomic oxygen (O), atomic nitrogen (N), and helium (He).

The lower part of the atmosphere, the one where we live and where weather happens, has been object of studies for centuries. However, it was only during the last 40 years that the middle atmosphere (~ 10 to 100 km) could be investigated, thanks to the development of various types of instruments placed on board balloons, airplanes and satellites, performing measurements that were not possible before. Observations in this altitude region are necessary in order to study the atmospheric system as a whole. Some of the knowledge that has been acquired about middle atmospheric dynamics is summarised in Chapter 2.

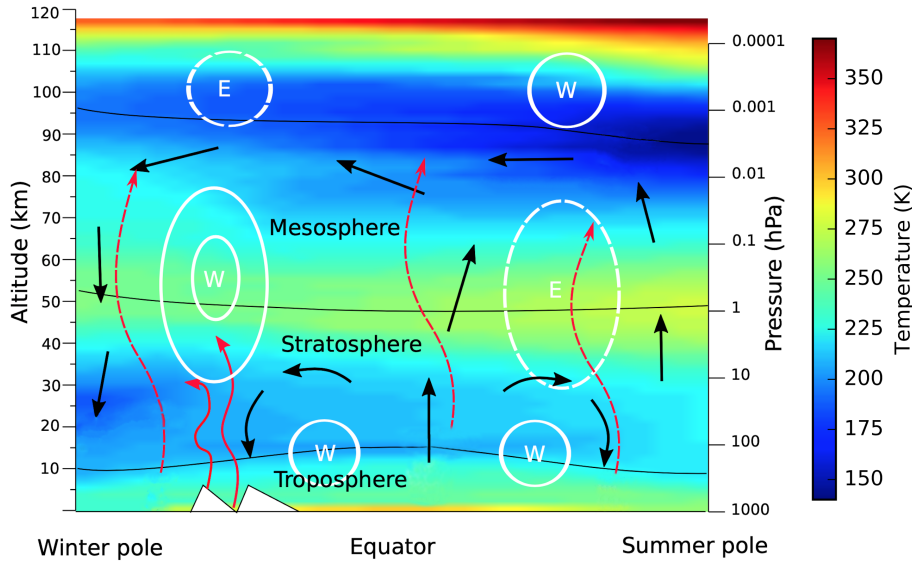


Figure 1.1: Summary picture of circulation in the atmosphere until 120 km altitude, and temperature distribution at the solstice (background colours). White lines represent zonal winds, i.e. westerlies (W) and easterlies (E); dashed and solid red arrows represent the direction of propagation of gravity and Rossby waves respectively; black arrows represent the mean meridional circulation. Figure credit: O.M. Christensen and M.R. Schoeberl.

Molecules undergo three different kinds of energy transition: electronic, vibrational and rotational. An electron of a molecule de-exciting from a higher energy state to a lower one, i.e. passing from a higher to a lower orbit, emits radiation in the ultraviolet and visible range. Lower energy transitions occur when the molecule goes from a vibrational state which is higher - faster vibration - to a lower one - slower vibration -, resulting in emission of infrared radiation. Finally, even lower energies are involved for transitions between rotational states, with emission of radiation in the millimetre and sub-millimetre spectral regions. In the Earth's atmosphere, radiance from molecular emission dominates over solar radiance in the infrared and millimetre/sub-millimetre spectral regions, thus observations of the atmosphere at these wavelengths allow to retrieve molecules' concentration and temperature. Keeping track of how these change in time and space is a source of information about the dynamics and chemical processes occurring. Spaceborne radiometers allow to perform such measurements on a global scale, and the Sub-Millimetre Radiometer (SMR) on board the Odin satellite is one of them (described in Chapter 3). It has been operating for over 19 years and still is today. That is a very long life if one considers that the mission was originally supposed to last 2 years. This particularly long operational period makes the Odin products very valuable for atmospheric science studies (see Figure 1.2).

However, the products of the observations relative to CO and H₂O have been subject to instrumental artifacts and were unusable, as in the case of CO, or presenting important biases, as in the case of H₂O. To make these long term data sets usable, the effects of the instrumental issues have been quantified and corrected. The work

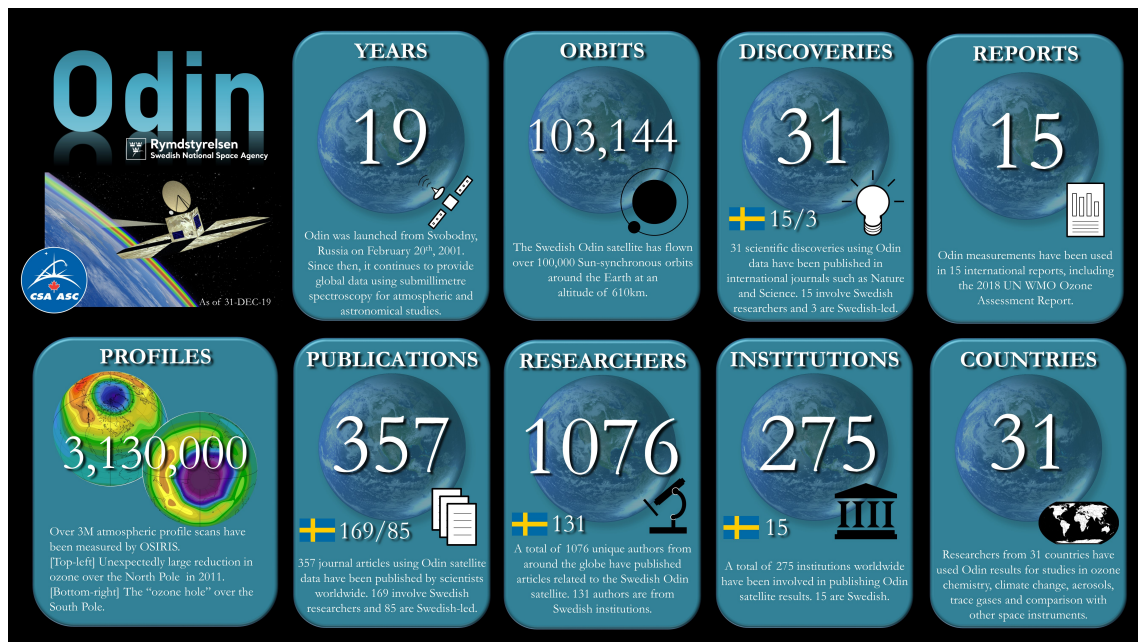


Figure 1.2: Infographics summarising achievements of Odin/SMR and Odin/OSIRIS altogether. Figure credit: Canadian Space Agency.

done to achieve this result constitutes the subject of the two papers summarised in Chapter 5 and included in this thesis. New retrievals from the corrected spectra have been performed and a description of the retrieval process is presented in Chapter 4.

1.1 The middle atmosphere

The region between approximately 10 and 100 km, including the stratosphere, the mesosphere and the lower thermosphere, is also referred to as middle atmosphere. External perturbations affect this region: with increasing altitude photochemical dissociation and ionisation of molecules by solar radiation become more important, so species at higher altitudes are more subject to solar variability; at low altitudes instead, middle atmosphere concentrations are influenced by volcanic eruptions and anthropogenic emissions. One can then see how there are coupling mechanisms linking the different layers. Also, what happens in the middle atmosphere affects lower altitudes, and thus us. The ozone layer is in fact located in the middle atmosphere, absorbing 250-300 nm ultraviolet solar radiation and protecting life on Earth from being exposed to such radiation. Because of these interactions between the middle atmosphere with lower and higher layers it is very important to observe it. Understanding of the processes going on in the middle atmosphere will allow to extend the upper altitude limit of climate models and therefore obtain more accurate climate forecasts. In fact, for a long time, the lower atmosphere was the only region taken into account in climate models but, due to the increasing realisation of interdependence between different layers, high-top models are now thought to be necessary to obtain more accurate climate forecast (Gerber et al., 2012; Marsh et al.,

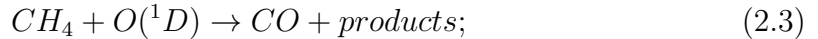
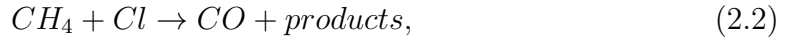
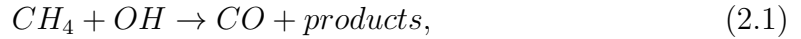
2013). The models used for IPCC (Intergovernmental Panel on Climate Change) climate assessments used to consider only altitudes up till 30 km in 2001 while today they reach up to 80 km and, in the future, they should cover the upper mesosphere and lower thermosphere.

Chapter 2

Middle atmospheric chemistry and dynamics: their effect on CO and H₂O distributions

2.1 CO and H₂O chemistry

The carbon monoxide which is present in the middle atmosphere is produced mainly via methane (CH₄) oxidation, through the following reactions:



and CO₂ photolysis:



Among these two processes, CO₂ photolysis is the dominant one (Minschwaner et al., 2010) and becomes increasingly important with height in the upper mesosphere and lower thermosphere due to incoming solar radiation in the Schumann-Runge continuum and Lyman- α wavelength. Because of this increase in CO₂ photolysis with altitude, CO distribution will result in being characterised by a large vertical concentration gradient, as can be seen in Figure 2.1a. The photochemical lifetime of CO is greater or equal to the zonal, meridional and vertical transport time scales in the middle atmosphere, ranging from a few days in the stratosphere to several hundreds of years at 100 km altitude (Brasseur and Solomon, 2005). Because of this, and due to its large vertical concentration gradient, CO is suitable for being used as a tracer of dynamics in this region (J. N. Lee et al., 2011; de Zafra and Muscari, 2004) (see Section 2.2).

Moreover, H₂O is a useful tracer of mesospheric circulation, due to its long photochemical lifetime which is of the order of months at the stratopause and of a

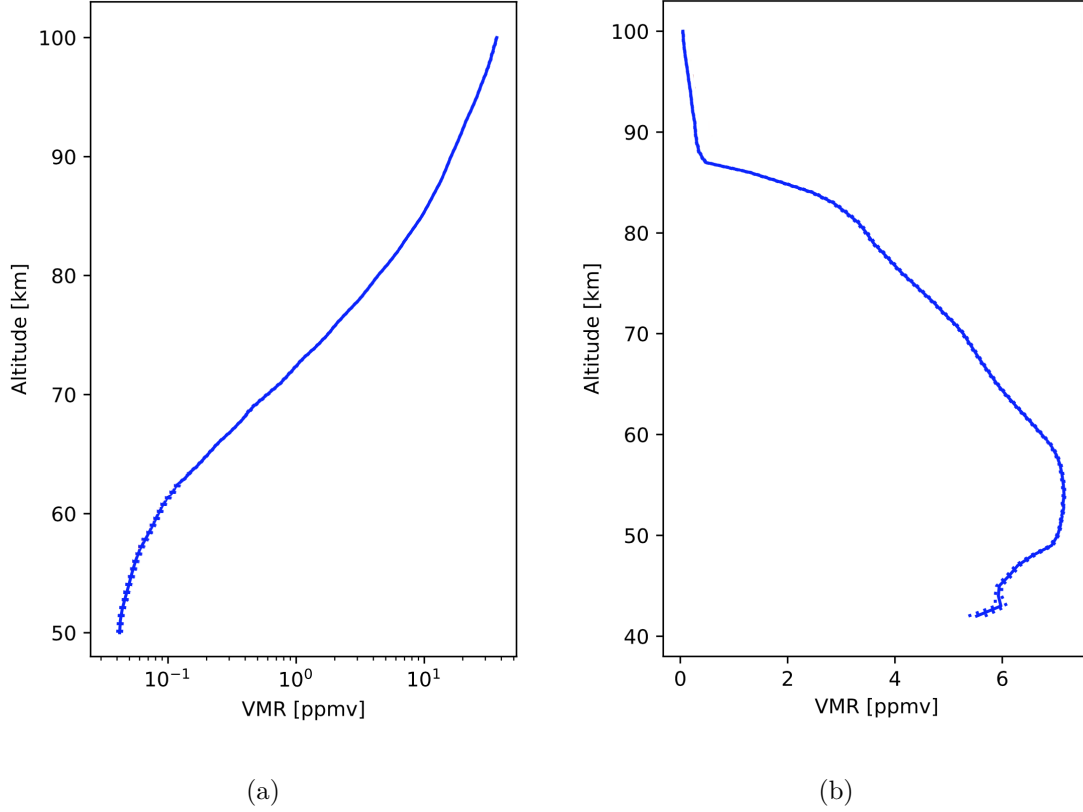


Figure 2.1: Mesospheric concentration profiles of CO (a) and H₂O (b) retrieved from SMR observations. The data are averaged globally and over the whole SMR operational period. The dashed lines represent the standard deviation of the median which, in some cases, is smaller than the thickness of the profile line, causing the dashed line not to be distinguishable.

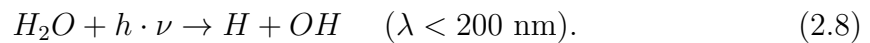
few days at 100 km (Brasseur and Solomon, 2005). Methane oxidation is a source of H₂O in the middle atmosphere which is produced through the following reaction:



CH₄ oxidation is more important in the stratosphere than in the mesosphere, since it decreases with height due to smaller abundances of CH₄, becoming negligible between 60 - 70 km. Above those altitudes, H₂ oxidation is dominant source through the reactions:



Photodissociation is the only major sink of H₂O in the mesosphere:



Due to increasing ultraviolet flux, photodissociation becomes more important with altitude and dominates above 70 km, causing H₂O concentration to decrease with altitude (as can be noted in Figure 2.1b) (Lossow et al., 2019).

2.2 Middle atmospheric dynamics

Middle atmospheric dynamics is driven by heat differences and by momentum deposition of breaking waves. The former are responsible for the formation of zonal winds, the latter is required for the establishing of meridional flows. In Figure 1.1 the zonal flows are represented by the white circles, with letters W and E representing westerlies and easterlies respectively. Zonal winds, at these altitudes, consist of geostrophic winds, i.e. winds that result from the balance between the Coriolis force and the pressure gradient force. Therefore, the vertical gradient of the zonal wind is proportional to the meridional temperature gradient via the thermal wind relation:

$$f \cdot \frac{\partial u}{\partial z} = - \frac{R_{air}}{r_{Earth} \cdot H} \cdot \frac{\partial T}{\partial \phi} \quad (2.9)$$

where f is the Coriolis parameter (positive in the northern hemisphere, negative in the southern hemisphere), u the zonal wind, z the altitude, R_{air} the gas constant for air, r_{Earth} the radius of the Earth, H the scale height and ϕ the latitude (Brasseur and Solomon, 2005). If there is an increase or decrease of zonal winds in intensity with altitude, or if easterlies (negative u) take place rather than westerlies (positive u), this is determined by the signs of f and the meridional temperature gradient.

Atmospheric waves consist of periodic perturbations of atmospheric variables (temperature, pressure, etc.). Waves which are generated at low altitudes propagate upwards and, because of decreasing air density, become unstable and dissipate. Meridional circulation in the middle atmosphere is driven by momentum deposition of breaking waves which are of two types: planetary-scale Rossby waves and smaller scale gravity waves. The former ones drive the circulation in the stratosphere, the latter ones drive it in the mesosphere. Rossby waves (solid red lines in Figure 1.1) are generated in the troposphere due to thermal forcing associated with sea/land contrast, and due to the encountering of obstacles - such as mountains - by air flows. These waves have the Coriolis force as restoring force and are mainly generated in the northern hemisphere, since it is characterized by more landmass than the southern hemisphere. They dissipate in the stratosphere exerting a negative drag that, in northern winter, is responsible for deceleration of the westerlies and, consequently, for the forcing of a poleward flow. Because of mass conservation, the poleward flow causes upwelling in the tropics and downwelling at the extra-tropics, resulting in the so-called Brewer-Dobson circulation (represented by the black arrows in correspondence of the stratosphere in Figure 1.1) (Brewer, 1949). Since Rossby waves are mostly generated in the northern hemisphere, the Brewer-Dobson circulation is more intense in the northern than in the southern hemisphere.

Other waves that drive meridional circulation are gravity waves (dashed red lines in Figure 1.1) which are characterised by significantly shorter wavelengths than Rossby waves (typically 10 to 1000 km) and have buoyancy as restoring force (Shepherd, 2000). They originate when parcels in a stably stratified fluid are displaced vertically and the return to the position of equilibrium gives rise to oscillations.

Displacement of parcels occurs due to different mechanisms such as convection, wave-wave interaction, frontal systems and irregular topography. Gravity waves propagate up to the mesosphere where they dissipate. During propagation they undergo filtering determined by the zonal velocity of the winds encountered on the path. More specifically, a gravity wave is filtered out when its zonal phase velocity equals the zonal velocity of the background wind; therefore only gravity waves with a zonal phase velocity greater than - or opposite to - the mean zonal wind velocity can propagate upward. These waves then break in the mesosphere, driving the air motion out of geostrophic balance. Thus, in the winter hemisphere, when they break they cause a negative drag that weakens the westerlies, forcing a equator-to-pole flow; while in the summer hemisphere they cause a positive drag, weakening the easterlies and forcing a pole-to-equator flow. The combination of these two flows results in a pole-to-pole flow and in an upwelling from the summer pole as well as a downwelling at the winter pole (see black arrows in correspondence of the mesosphere in Figure 1.1). The upwelling and the downwelling cause, respectively, an adiabatic cooling at the summer pole and an adiabatic heating at the winter pole, thus resulting in mesopause temperatures being lower above the summer pole (as mentioned in Section 1.1), despite the higher insulation.

At the poles, during local winter, a polar vortex also takes place, causing a descent of colder air from upper mesosphere to the lower stratosphere. The polar vortex consists of a low-pressure area, around 1000 km of diameter, that rotates counter-clockwise at the north pole and clockwise at the south pole. Due to its dependence on temperature difference between the tropics and the poles it occurs only during local winter, giving rise to a strong meridional temperature gradient across its front. The front separates an area of cold dry air inside the vortex from an area of warm moist air outside of it. These winter polar downward currents result in the descent of CO richer air coming from higher altitudes. The downwelling winter air is also dryer, resulting in lower H₂O concentrations to be observed at the poles during local winter (see Figure 2.2). Moreover, a sink for H₂O in the mesosphere is the formation of ice particles and their sedimentation which occurs only at high latitudes and during local winter. On the other side, in the summer polar region, an uplift causes water vapour to reach the mesopause, resulting in an increase of H₂O concentration (Lossow et al., 2019).

Gravity waves are also responsible of the presence of Semi-Annual Oscillation (SAO) of zonal winds in the tropics (Ray et al., 1998). The easterly phase of stratospheric SAO of zonal winds is driven by meridional advection of easterlies from the summer hemisphere across the equator, together with the breaking of Rossby waves. The westerly phase instead is driven by momentum deposition of gravity waves. Also mesospheric SAOs are driven by gravity waves generated in the troposphere and propagating towards higher altitudes. While travelling through the stratosphere, these waves are filtered by the local zonal wind SAO so only gravity waves with opposite zonal phase velocity reach the mesosphere and break there. This wave filtering does so that mesospheric SAOs have a phase shift of 180° compared to

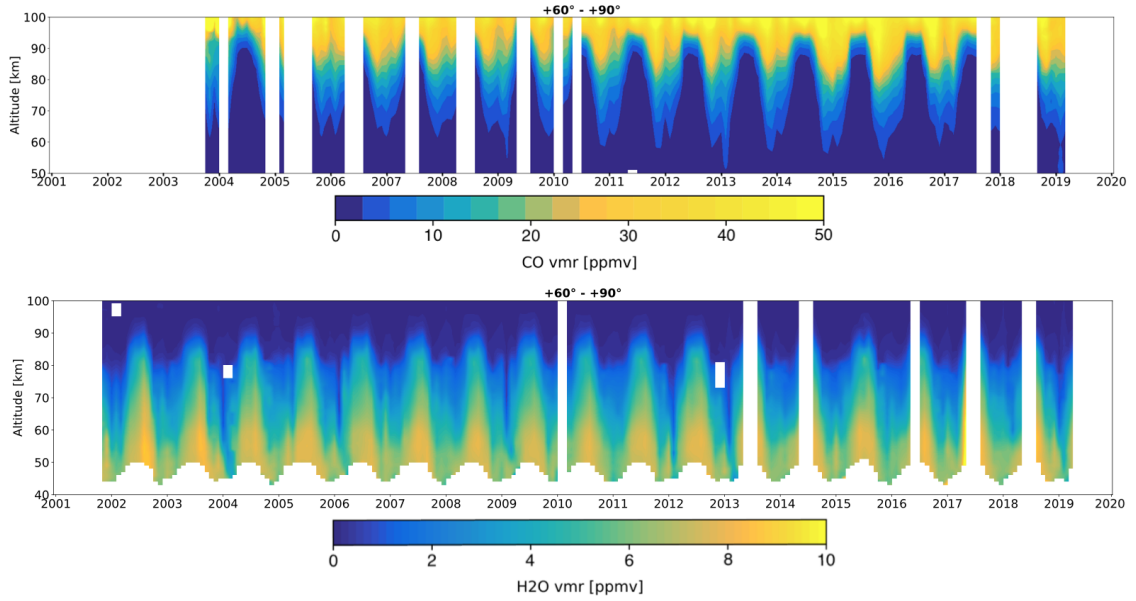


Figure 2.2: Time series of CO (top) and H₂O (bottom) volume mixing ratios measured by SMR for the $+60^{\circ} - +90^{\circ}$ latitude band, taken from Paper 1 and 2 respectively. The white bands indicate periods during which the number of scans in the given latitude band is lower than 10. The ticks on the x-axis correspond to the beginning of each year. Note the two different colour scales.

stratospheric SAOs. SAO of zonal winds lead to SAO in meridional circulation and, consequently, mean vertical motion. In Figure 2.3 it can be noticed how mean vertical motion SAOs have an effect on mesospheric CO and H₂O concentrations above the tropics. In particular, sinking or weak rising motion of air causes the presence of higher CO and lower H₂O concentrations in correspondence of the equinoxes. Viceversa, solstices are characterised by a stronger rising motion, therefore lower CO and higher H₂O concentrations are observed.

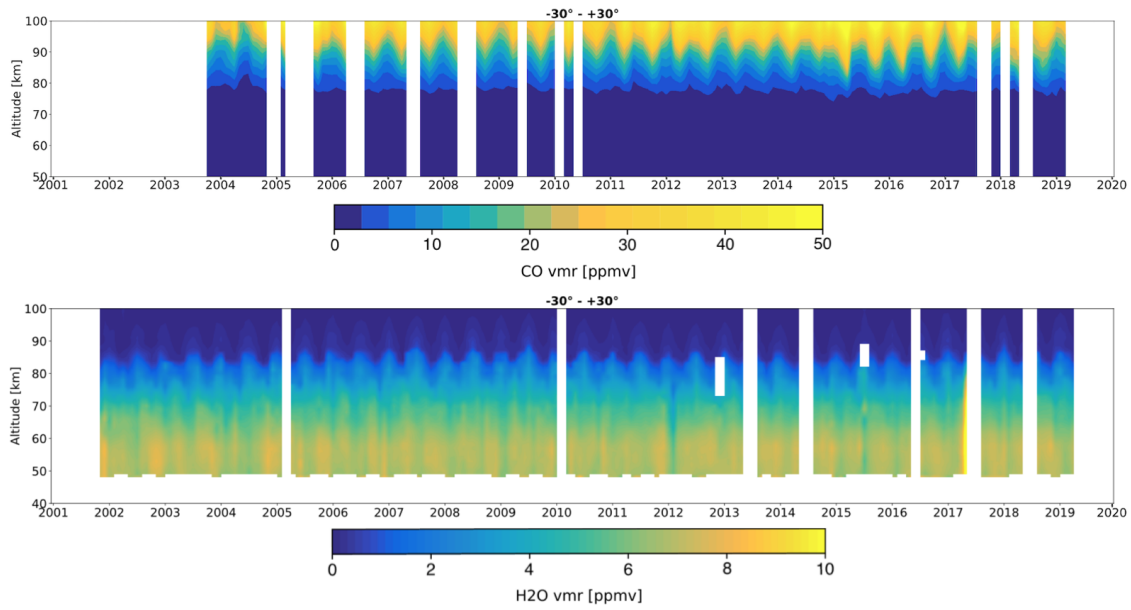


Figure 2.3: Time series of CO (top) and H₂O (bottom) volume mixing ratios measured by SMR for the $-30^{\circ} - +30^{\circ}$ latitude band, taken from Paper 1 and 2 respectively. The white bands indicate periods during which the number of scans in the given latitude band is lower than 10. The ticks on the x-axis correspond to the beginning of each year. Note the two different colour scales.

Chapter 3

The instrument

3.1 Measurement techniques of the middle atmosphere

Throughout the years it has been possible to improve our understanding of all these dynamical and chemical processes through the development of models and through observations of the atmosphere carried out with various kinds of instruments. Probes on board of balloons and airplanes allow us to carry out in-situ measurements, but to observe different altitudes simultaneously and to have global coverage, remote sensing measurements are needed. Different observation geometries and different techniques are implemented to perform remote sensing of the middle atmosphere. One method consists of using ground-based instruments that look upwards into the atmosphere. One of the advantages with these kind of instruments is that they are easier to maintain, compared to satellite instruments, and are therefore better suited for very long term observations. Moreover, they are suitable for performing measurements above a specific location in a continuous way. The main drawback is that they can cover only one geographical region. Again, to cover larger geographical region, as well as the whole globe, satellite measurements are needed. A summary of the different satellite geometries and techniques that can be used are summarised in Figure 3.1. All of them, in contrast with the ground-based instruments, have in common the limitation of not being able to measure local transient phenomena.

There are two types of observing geometries that satellites can operate with: nadir viewing and limb viewing. The former is used to look straight down to the Earth and mainly perform column integrated measurements. The latter has a line of sight that crosses a longer path through the atmosphere and, by performing measurements at different tangent altitudes, facilitates the estimation of the altitude of the emitters. Vertically resolved observational data can thus be obtained. One way to use limb viewing is to observe direct thermal emission from the molecular species in the middle atmosphere, thus being able to measure throughout the whole orbit, as is the case with Odin/SMR. Limb geometry can also be used to measure limb scattered sunlight with instruments which observe in the UV-visible band. One advantage of thermal emission measurements, with respect to scattered sunlight ones,

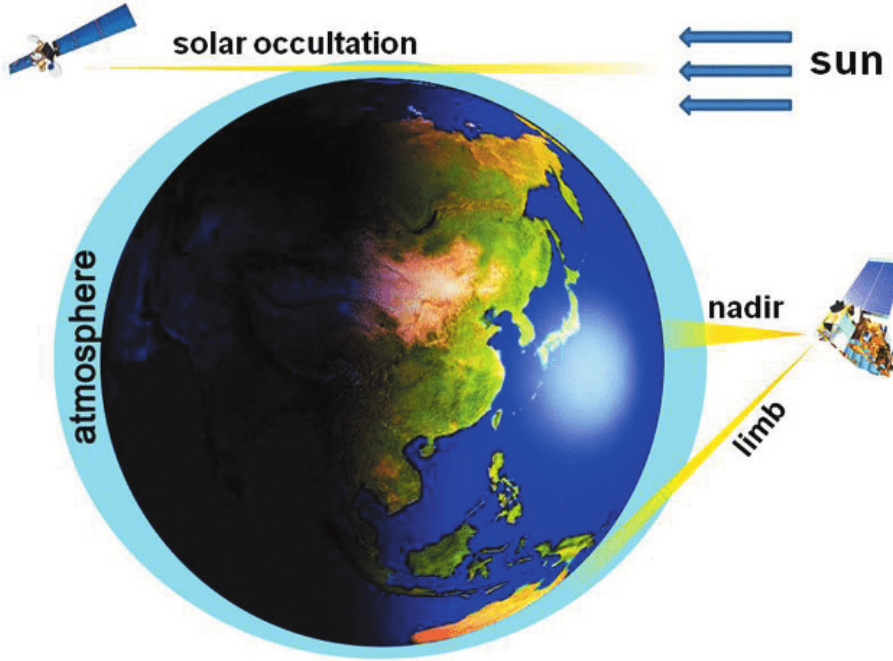


Figure 3.1: Figure summarizing satellite geometries and techniques for atmospheric observations (K. Lee et al., 2009).

is that the former allow to measure both during daytime and nighttime. Another way of implementing the limb viewing geometry is to use occultation instruments. Solar occultation instruments estimate the concentration of gases in the atmosphere by measuring their absorption of the solar radiation during a sunrise/sunset. There are also stellar occultation instruments that measure various stars instead of the Sun as radiation sources. The advantage of this kind of instruments is that their measurements present higher signal to noise ratios, and are therefore characterised by better resolution. Since they can perform measurements only during sunrise/sunset, or only when the star used as a source is in the limb view line of sight, occultation instruments perform much fewer measurements than limb sounding instruments measuring thermal emission or scattered sunlight.

3.2 *Odin/SMR*

The *Odin* satellite was launched on 20 February 2001 into a circa 600 km sun-synchronous orbit with inclination 97.77° and 18:00 hrs ascending node. The project originated from a collaboration between Sweden, Canada, France and Finland with the purpose of using the satellite for both astronomical and atmospheric observations. Both missions were carried out sharing the observation time until 2007, when the astronomical mission ended. After this date, the observation time has been entirely dedicated to the atmospheric mission. There are two instruments on board *Odin*: the Sub-Millimetre Radiometer (SMR), on which this thesis is focused, and OSIRIS (Optical Spectrograph and InfraRed Imaging System). Both instruments perform limb sounding of the atmosphere, measuring while scanning in both upwards and

downwards directions (see Figure 3.2), with a vertical sampling of ~ 1.5 km in the stratosphere to 6 km in the mesosphere depending of the measurement mode. We define a scan as the set of spectra measured between two adjacent turning points. The measured spectrum results from the superimposition of the radiation from all of the emitters enclosed by the beam of the instrument (see Chapter 4) and is assigned a tangent altitude corresponding to the middle of the integration time. The SMR observation schedule features scans that cover different altitude ranges: 7 - 72 km (stratospheric scans), 7 - 110 km (strato-mesospheric scans) and 60 - 110 km (mesospheric scans).



Figure 3.2: Upward and downward scanning of the atmosphere by Odin/SMR.

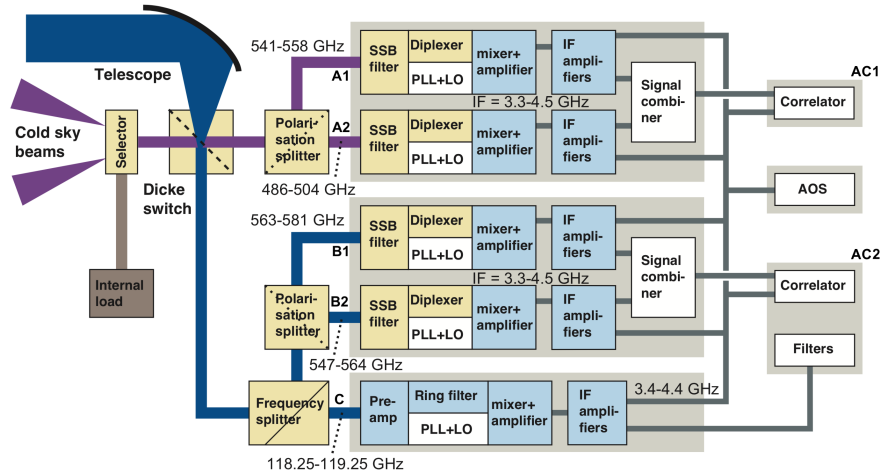


Figure 3.3: Block diagram of the Odin radiometer (Frisk et al., 2003).

A schematic diagram of the major components of SMR is shown in Figure 3.3. SMR has four sub-mm receivers that cover frequencies between 486 - 504 GHz and 541 - 581 GHz allowing us to observe stratospheric and mesospheric O_3 , H_2O , CO , NO , ClO , N_2O , HNO_3 emission from rotational transitions. Moreover SMR also presents a mm-wave receiver to detect O_2 emissions at 118 GHz (Frisk et al., 2003).

A Dicke switch allows rapid changing of the input source radiation between the main beam, a hot load and the cold sky, the latter two being used for calibration purposes (Murtagh et al., 2002). The signal travels through a Martin-Puplett interferometer - an interferometer with wire grid polarizer and rooftops mirrors to reflect the signal. In the interferometer, the signal is split into two beams by the polarizer; subsequently, a frequency dependent phase delay

$$\phi(\nu) = 2\pi \frac{2l\nu}{c} \quad (3.1)$$

is introduced between the two components by moving one of the rooftop mirrors and introducing an extra path length (l) in one of the interferometer arms. The response of the interferometer as a function of ϕ is given by:

$$r = \frac{1}{2}[1 + \cos(\phi)] \quad (3.2)$$

with maximum and minimum interference occurring respectively when

$$2l = n \frac{c}{\nu} \quad (3.3)$$

and

$$2l = \left(n + \frac{1}{2}\right) \frac{c}{\nu} \quad (3.4)$$

where n is the index of maxima and minima. Therefore, if it is desired to obtain a response of 1 at frequency ν_1 and a response of 0 at ν_0 with no other minima and maxima in between, then the extra path length has to be set to:

$$l = \frac{c}{4|\nu_1 - \nu_0|}. \quad (3.5)$$

In SMR, the extra path length is set so as to suppress the sideband signal resulting from combining the source signal with the one from a local oscillator (LO). The LO is also injected through the Martin-Puplett interferometer. The LO frequency is fine-tuned by means of a Phase-Lock Loop (PLL). This combination of signals is carried out to convert the source frequency from the 500 GHz region to a lower one (3.3 - 4.5 GHz). This allows amplification of the signal which would be impossible at the original frequencies, due to technical limitations. The two signals are combined with the use of a Schottky mixer, for which the output signal is a nonlinear function of its input. This implies that the output signal will be a function of the sum and difference of the frequencies of the input signals, therefore consisting of two sidebands: the primary band, including the signal of scientific interest, and the image band. SMR is run in single sideband mode which means that one of the sidebands is suppressed. To avoid the unwanted signal from the image band being included in the measurement, the Martin-Puplett interferometer is used to maximize suppression of those frequencies and maximize transmission of the primary band. However, it is actually not possible to achieve a response of 0, i.e. perfect suppression, and a more correct interferometer response is given by:

$$r = r_0 + \frac{(1 - 2r_0)}{2} \left[1 + \cos \left(\frac{4\pi l\nu}{c} \right) \right] \quad (3.6)$$

where r_0 is the lowest response achieved. Consequently, the sideband leakage will characterize the measurement. It is defined as:

$$p(\nu) = \frac{r(\nu')}{r(\nu) + r(\nu')} \quad (3.7)$$

where ν and ν' are the primary band and image band center frequencies, respectively (Eriksson and Urban, 2006). Note also a linear dependency of l with respect to the satellite temperature, due to thermal expansion, affecting the response of the interferometer. Eventually, the signal is amplified and directed to the autocorrelator spectrometers.

SMR has two autocorrelator spectrometers (denoted as AC1 and AC2 in Figure 3.3) that filter the input signal into eight sub-bands and calculate the autocorrelation function for each of them. Upper and lower sideband of a same oscillator are used for single-sideband filtering, thus the sub-bands are organised in four pairs of 200 MHz each. The two autocorrelators can be connected to two mixers each (namely AC1 is connected to A1 and A2, and AC2 to B1 and B2) allowing to measure a 400 MHz block simultaneously using one spectrometer. The spectrometers have resolutions that can be set between 150 kHz and 1.2 MHz to which correspond spectral coverages of 100 and 800 MHz respectively (Frisk et al., 2003; Murtagh et al., 2002).

To cover different frequencies, the receivers and the spectrometers can be used in different combinations, each one constituting what is called a Frequency Mode (FM).

3.3 Calibration process

The purpose of calibration is to estimate the antenna temperature T_a from the beam signals recorded by the instrument. T_a is defined as the temperature of a hypothetical black body which would result in the same received power at the antenna aperture as in the case of the observed source. Odin/SMR measures three types of beam signals: the cold sky (c_s), the load (c_l) and the main beam signal (c_a). The contributions to such signals for a channel i can be expressed as follows:

$$c_{a,i} = g_i(\eta_a T_{a,i} + T_{rec,i} + (1 - \eta_a) T_{amb,i}), \quad (3.8)$$

$$c_{s,i} = g_i(T_{s,i} + T_{rec,i}) \approx g_i T_{rec,i}, \quad (3.9)$$

$$c_{l,i} = g_i(T_{l,i} + T_{rec,i}), \quad (3.10)$$

where g_i is the receiver gain, η_a is the main beam efficiency (assumed to be equal to 1 for sky beam and the load signals), $T_{amb,i}$ is the receiver ambient temperature and $T_{rec,i}$ is the receiver noise temperature. $T_{a,i}$, $T_{s,i}$ and $T_{l,i}$ are the antenna temperature,

cosmic background temperature and load temperature, respectively. In Eq. 3.9, $T_{s,i}$ is negligible in comparison to $T_{rec,i}$ since the former is equal to 0.003 K at 500 GHz and the latter is 3000 K. From the equations above it is possible to derive the unknown $T_{rec,i}$, g_i , η_i and $T_{a,i}$. In particular, g_i and $T_{a,i}$ will be respectively given by (Rydberg et al., 2017):

$$g_i = \frac{c_{l,i} - c_{s,i}}{T_{l,i} - T_{s,i}} \quad (3.11)$$

and

$$T_{a,i} = \frac{1}{\eta_a} \left(\frac{c_{a,i} - c_{s,i}}{g_i} - (1 - \eta_a)T_{amb} \right) = \frac{1}{\eta_a} \left((c_{a,i} - c_{s,i}) \frac{T_{rec,i}}{c_{s,i}} - (1 - \eta_a)T_{amb} \right), \quad (3.12)$$

where the same value of T_{rec} and T_{amb} is used for all spectra within the same scan.

Small perturbations in $T_{s,i}$ and $T_{l,i}$ will result in unwanted features called “ripples” in the calibrated spectra. It can be demonstrated that, when $T_{a,i}$ is approximately 0 K, there is a maximum sensitivity to the perturbations of the cold sky signal (Rydberg et al., 2017). This happens for measurements at high tangent altitudes, where the spectra should be centered around 0 K but instead present a wave pattern. The artifact is removed by fitting median high tangent altitude spectra with a sinusoidal function - whose phase changes with T_{amb} - and removing this wave pattern from the spectra. Sub-bands that are contaminated by atmospheric information cannot be included in the fit and the corresponding part of the spectra are filtered out, leaving blank spaces in the spectra. On the other hand, sensitivity of $T_{a,i}$ to the perturbations in the load signal is minimum when $T_{a,i}$ is close to 0 K and reaches its maximum when $T_{a,i}$ is close to the load temperature, though this never happens. This artifact is hard to detect as it consists of a weak signal in addition to strong atmospheric signal, and is therefore left unresolved.

Another calibration-related artifact arises due to the presence of non-linear gain variations which are not captured by the interpolation of the reference signals. So, at a given time t_j during which the main beam is detected, there will be a difference between the estimated (\hat{c}_s) and true (c_s) sky beam giving rise to the non-captured gain variation $\Delta g'$:

$$\hat{c}_s(t_j) - c_s(t_j) = \Delta c_s = \Delta g' T_{rec}. \quad (3.13)$$

Note how the gain variation could result in an artifact limited to a sub-band or in a broadband artifact, depending on whether the gain variation originates from a spectrometer or from one of the mixers.

3.4 Technical issues related to CO and H₂O datasets

In Paper 2, causes for artifacts in the SMR H₂O dataset were investigated. In particular, non-linear gain variations were thought to be responsible for the big differences in H₂O observed with SMR with respect to other instruments. An attempt to quantify such gain variations was made by introducing both a broadband correction factor and a sub-band one, but no value could bring an improvement in the comparison between SMR and other instruments. However, the most probable cause for such discrepancies is thought to be an underestimation of sideband leakages, that is an underestimation of r_0 in Eq. 3.6, for both FMs used for H₂O observations (i.e. FM13 and FM19, both centered around 557 GHz). This underestimation resulted in the fact that spurious signal originating from a sideband leakage was considered as part of the signal of interest, causing a misestimation of retrieved concentration and temperature (see Chapter 5 and Part 2).

Moreover, in Paper 1 it was observed how the malfunctioning of the PLL used for CO observations (performed using FMs 14, 22 and 24, centered around 576.5 GHz) leads to a shift of the LO frequency from its nominal value. This causes a frequency shift in the observed spectra that assumes different values within a same scan. In addition, the PLL malfunctioning has even an effect within the integration time causing line broadening. These issues caused data to be unusable to perform retrievals or lead to a misestimation of the CO concentration (see Chapter 5 and Part 2).

Chapter 4

Retrieval process

One scan of Odin/SMR L1 data, i.e. the calibrated spectra, can be represented as a vector

$$\mathbf{y} = \begin{bmatrix} \mathbf{y}_1 \\ \mathbf{y}_2 \\ \vdots \\ \mathbf{y}_s \end{bmatrix}, \quad (4.1)$$

where s is the number of samples in the scan and each element of \mathbf{y} is the spectrum collected at a single tangent altitude, i.e. a brightness temperature value for each frequency bin. An example of a spectrum collected from SMR at 30 km altitude is shown in Figure 4.1. Given the geometry of limb measurements (see Section 3.1), the spectrum, here featuring CO (left) and O₃ (right) emission lines, is the result of the superimposition of emissions from different altitudes. In Figure 4.2 it can be seen how the shape of the emission contribution varies with altitude, hence the shape of the observed line will be determined by how those variously shaped contributions sum up, i.e. a higher concentration at a certain altitude will cause the corresponding line shape to contribute more to the measured line. Note that the ozone lines shown in the two figures correspond to two different ozone transitions and that the shape of the emission presents a different altitude dependence for different frequency bands. The retrieval process consists in understanding how much a certain line shape, i.e. the emission from a certain altitude, has contributed to the observed line so to obtain concentration and temperature profiles.

4.1 Line broadening

What determines the line shape? Molecular emission lines in the atmosphere are subject mainly to two types of broadening processes: pressure broadening and Doppler broadening. Pressure broadening, resulting in a line shape corresponding to Lorentz profile (Lorentz, 1906), occurs because the higher the pressure of a gas the more frequent the collisions between its molecules will be, resulting in a shortening of the life time of the rotational states involved in the transition. This causes a

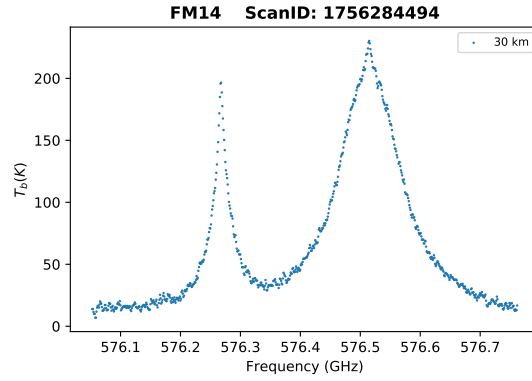


Figure 4.1: 30 km tangent altitude spectrum measured by Odin/SMR featuring CO (left) and O₃ (right) 576 GHz emission lines.

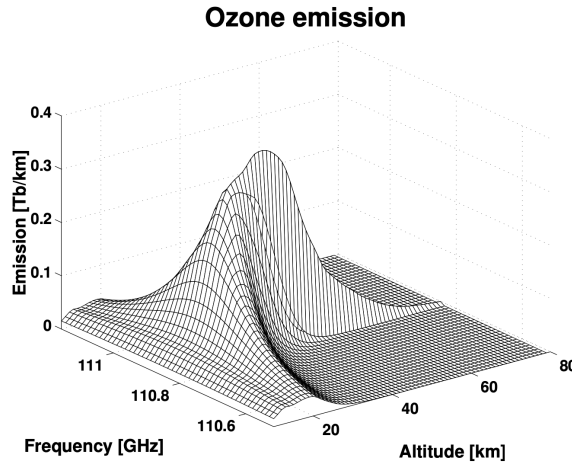


Figure 4.2: Emission from ozone around 110.84 GHz. Note the different line shapes at different altitudes. Figure credit: Patrick Eriksson.

broadening of the line depending on pressure and temperature according to the following equation:

$$2\gamma_p = 2\gamma_0 \frac{P}{P_0} \left(\frac{T_0}{T} \right)^n \quad (4.2)$$

where $2\gamma_p$, which is the full width at half maximum (FWHM) of the line, has a linear dependence to the pressure P . $2\gamma_0$, P_0 and T_0 are respectively the FWHM, pressure and temperature at the reference level (at the ground level it would be $2\gamma_0 = 3 - 6$ GHz and the index $n = 0.5 - 1$). Doppler shift instead is related to the thermal motion of the molecules. If a molecule emits while in motion toward the observer, this person will observe a line shifted toward higher frequencies; vice versa if the molecule is moving away from the observer. If the gas is in thermal equilibrium then the velocity distribution of the molecules is Gaussian, thus will be also the line shape. Moreover, the higher the temperature of the gas the higher will be the

molecules velocity dispersion around the mean velocity, hence the broader the line. The FWHM of the line will be dependent on the temperature T according to the equation:

$$2\gamma_d = 2\frac{\nu_0}{c}\sqrt{\frac{2RT}{M}}, \quad (4.3)$$

where M is the molecular weight in atomic mass and R is the universal gas constant. Pressure broadening dominates at lower altitudes, becoming less and less strong with increasing altitude (i.e. exponentially decreasing pressure), while Doppler broadening dominates at higher altitudes. As an example, for the ozone line at 500 GHz, pressure broadening dominates until 60 km altitude and Doppler broadening dominates above 80 km. The 60 - 80 km range is characterised by a Voigt line shape, given by a convolution of the pressure and Doppler line shapes. So it is possible, from the observed line, to understand how much a single line shape contributed to the total, therefore deducing concentration and temperature of a species at a certain altitude. For limb sounding, the most important source of altitude information is vertical scanning, though. However, note that Doppler broadening is not dependent on pressure but only on temperature which gives very little information about the altitude, since temperature varies less than pressure with altitude; moreover, Doppler broadening has a low dependence on temperature, i.e. \sqrt{T} . So, on the high side, pressure broadening provides information only until a certain altitude; additionally also information about the lowest altitudes is lost, since there the pressure broadening is so big that it causes the line width to be larger than the spectrometer band.

4.2 The inverse problem

Measurements are performed to retrieve the state vector

$$\mathbf{x} = \begin{bmatrix} \mathbf{v}_1 \\ \mathbf{v}_2 \\ \mathbf{t} \\ \Delta\mathbf{o} \\ \Delta\theta \\ \Delta\nu \end{bmatrix} \quad (4.4)$$

which consists of \mathbf{v}_1 and \mathbf{v}_2 , i.e. the concentration profiles of the gas species observed using a certain FM, the temperature profile \mathbf{t} , the brightness temperature offsets $\Delta\mathbf{o}$ (one for each tangent altitude), the pointing offset $\Delta\theta$ and the frequency off-set $\Delta\nu$. The latter two are scalar values which apply to the whole scan. The three offsets are estimated to compensate inaccurate determination of gain (from calibration), pointing of the instrument (from attitude data) and frequency (from the LO-signal nominal frequency) respectively. If the LO-signal is phase-locked, the frequency offset is assumed to be constant throughout the whole scan. However, if there is a failure in the PLL, like the one that affects the FMs used for CO observations (see Paper 1), then a different frequency correction for each spectrum of the scan is needed.

The inverse problem, i.e. the problem of getting the state vector \mathbf{x} from the measurement vector \mathbf{y} is an ill-posed one, meaning that there are more solutions to it. In fact, several combinations of emission line shapes can sum up to the same observed line. How to know which retrieved state vector is closer to the truth?

First, a forward model (\mathcal{F}) with its parameters (\mathbf{b}) has to be chosen. Thus the vector \mathbf{y} is related to \mathbf{x} via the following relation:

$$\mathbf{y} = \mathcal{F}(\mathbf{x}, \hat{\mathbf{b}}) + \varepsilon_b + \varepsilon_n, \quad (4.5)$$

where $\hat{\mathbf{b}}$ is the best estimate of the forward model parameters, ε_n is the measurement noise and ε_b is the uncertainty deriving from not knowing the exact values of \mathbf{b} . The forward model used for Odin/SMR retrievals is the Atmospheric Radiative Transfer Simulator (ARTS) (Eriksson, Buehler, et al., 2011) with the assumptions of lack of scattering (valid for SMR sub-mm wavelengths and strato-mesospheric altitudes), local thermal equilibrium and a 1D atmosphere (atmospheric fields only dependent on pressure). The retrieval process can be summarised as follows:

$$\hat{\mathbf{x}} = \mathcal{I}(\mathbf{y}, \mathbf{x}_a, \hat{\mathbf{b}}, \mathbf{c}), \quad (4.6)$$

where $\hat{\mathbf{x}}$ is the retrieved state vector, \mathcal{I} is the inverse model, \mathbf{c} represents the additional variables introduced by the inverse model, and \mathbf{x}_a is an a priori estimate of \mathbf{x} , usually coming from a model or from climatology of another instrument.

The approach used here to solve the ill-posed problem (Eriksson, 2015) is the Optimal Estimation Method (OEM), an approach that involves the introduction of a regularisation. To explain what this means, we introduce the cost function:

$$C(\mathbf{x}) = (\mathbf{y} - \mathcal{F}(\mathbf{x}, \hat{\mathbf{b}}))^T \mathbf{S}_o^{-1} (\mathbf{y} - \mathcal{F}(\mathbf{x}, \hat{\mathbf{b}})) + (\mathbf{x} - \mathbf{x}_a)^T \mathbf{S}_a^{-1} (\mathbf{x} - \mathbf{x}_a). \quad (4.7)$$

The OEM consists in minimizing $C(\mathbf{x})$. So the retrieved state vector ($\hat{\mathbf{x}}$) will be given by:

$$\hat{\mathbf{x}} = \min_{\mathbf{x}} (C(\mathbf{x})), \quad (4.8)$$

where \mathbf{S}_o is the covariance matrix of the observation system (i.e. combination of instrument and forward model) and \mathbf{S}_a is the a priori uncertainty covariance matrix. The regularisation is present in the second term of Eq. 4.7 which represents how well the solution agrees with the a priori. If this term weren't present, the obtained $\hat{\mathbf{x}}$ would coincide with the standard least squares solution. So the best solution has to be in accordance with both the measurement and the a priori.

When the retrieval problem cannot be considered linear, i.e. when derivatives of \mathcal{F} and \mathcal{I} are not valid over a significant range, as in this case, an iteration process is needed to determine the solution. The iteration starts by first assuming \mathbf{x}_a as a solution, the successive tentative solution is considered valid if its cost is lower than the previous solution, and so on. The iteration scheme used is the one from the Levenberg-Marquardt method, which involves the use of a parameter γ to evaluate the convergence of the iteration (Rodgers, 2000).

Chapter 5

Summary of appended papers and future outlook

5.1 Paper 1

Before this study, of the 18 years of Odin/SMR observations of mesospheric CO only data from a year - October 2003 to October 2004 - was usable for scientific purposes. This was the only part of the dataset that was not affected by a malfunctioning of the PLL used for CO observations. The PLL is used to keep the phase of the LO signal stable, and its malfunctioning results in random and continuous modification of the LO frequency. Thus, when LO is combined to the source signal through the mixer, it results in a signal that is also affected by frequency shift. For this reason, most of the CO L1 data were unusable to perform retrievals because the CO line was shifted away from its theoretical position and, in some cases, it was even shifted away from the observed band. These latter extreme cases could not be recovered. For all the other scans, a correction algorithm was developed which allowed to identify the center of the CO line and shift it back to its theoretical position. Not all spectra within a scan were affected by the same shift, therefore a different correction has been applied to each single spectrum in the scan. The PLL malfunctioning was affecting the spectra also at a time scale smaller than the integration time, resulting in an artificial broadening of the spectral lines. To take this into account during the retrievals, we have used a broader response function. The CO dataset was thus successfully recovered, providing new mesospheric and lower thermospheric CO concentration profiles which extend between 50 - 100 km and over the whole globe. A validation study has been carried out, comparing SMR observations with the ones from OSO, MIPAS, ACE-FTS and MLS. The overall agreement with the other instruments is very good between 60 and 80 km altitude, with relative differences close to zero. Between 50 - 60 km SMR shows a positive bias up to +20%, while between 80 - 100 km the observed bias is negative and reaching up to -20%.

5.2 Paper 2

Comparisons between Odin/SMR H_2O concentrations used to show poor accordance with other instruments. This suggested the presence of an instrumental artifact that was affecting the FMs used for observing H_2O . Different hypotheses have been investigated. Tests to investigate if the pointing offset of the instrument was too far from the nominal value have resulted negative, as well as tests to look for possible non linear gain variation which might have caused errors in the calibration. Finally, the most probable cause of SMR H_2O biases have been identified in having underestimated single sideband leakage. Such an underestimation implies that spurious signal from the image band leaking into the primary band is not recognised as such, causing a misestimation of the retrieved concentrations and temperature. A lower value of the minimum suppression, i.e. a greater leakage, have been assumed and new retrievals have been performed, resulting in a new dataset of almost 19 years of H_2O concentration profiles. The new data are in better accordance with other instruments, compared to the older version. Relative differences in H_2O concentration are always in the -40% - +20% range between 40 - 80 km and diverge at higher altitudes.

5.3 Future outlook

The work presented in this thesis resulted in new long-term and global CO and H_2O data sets. As previously explained, these two species are particularly useful to study the middle atmospheric dynamics. This is what we are planning to do in a second step. CO and H_2O data can be used as tracers to distinguish nitric oxide (NO) produced by energetic particle precipitation in the upper mesosphere and transported downward in winter from NO produced locally in the lower mesosphere by N_2O oxidation. Also, CO and H_2O measured concentrations can be employed to calculate the descent rate of the polar vortex. These two pieces of information together can help us to calculate the amount of NO transported down from the mesosphere and lower thermosphere towards the upper stratosphere, where it plays an important role in the catalytic destruction cycle of ozone. This will help us to get a better understanding of this mechanism, which is currently not well reproduced by the climate models.

Moreover, since temperature is also a retrieval product in the newly processed H_2O dataset, this will provide a valuable source to look for mesospheric temperature trends.

Bibliography

- Brasseur, G.P. and S. Solomon (2005). “Aeronomy of the Middle Atmosphere”. In: *Springer, The Netherlands, 3rd edition* (cit. on pp. 3, 7–9).
- Brewer, A. W. (1949). “Evidence for a world circulation provided by the measurements of helium and water vapour distribution in the stratosphere”. In: *Quarterly Journal of the Royal Meteorological Society* 75.326, pp. 351–363. DOI: 10.1002/qj.49707532603 (cit. on p. 9).
- de Zafra, R.L. and G. Muscari (2004). “CO as an important high-altitude tracer of dynamics in the polar stratosphere and mesosphere”. In: *J. Geophys. Res.* 109.D06105. DOI: doi:10.1029/2004JD005102 (cit. on p. 7).
- Eriksson, P. (2015). “Algorithms Theoretical Basis Document - Level 2 processing”. In: *Technical report, Chalmers University of Technology* (cit. on p. 24).
- Eriksson, P., S. A. Buehler, C. P. Davis, C. Emde, and O. Lemke (2011). “ARTS, the atmospheric radiative transfer simulator, version 2”. In: *Journal of Quantitative Spectroscopy and Radiative Transfer* 112.10, pp. 1551–1558. ISSN: 0022-4073. DOI: 10.1016/j.jqsrt.2011.03.001 (cit. on p. 24).
- Eriksson, P. and J. Urban (2006). “Post launch characterisation of Odin-SMR sideband filter properties”. In: *Technical report, Chalmers University of Technology* (cit. on p. 17).
- Frisk, U. et al. (2003). “The Odin satellite I. Radiometer design and test”. In: *A&A* 402.3, pp. L27–L34. DOI: 10.1051/0004-6361:200303335 (cit. on pp. 15, 17).
- Gerber, E.P. et al. (2012). “Assessing and Understanding the Impact of Stratospheric Dynamics and Variability on the Earth System”. In: *Bulletin of the American Meteorological Society* 93.6, pp. 845–859. DOI: 10.1175/BAMS-D-11-00145.1 (cit. on p. 5).
- Lee, J. N., D.L. Wu, G.L. Manney, M.J. Schwartz, A. Lambert, N.J. Livesey, K.R. Minschwaner, H.C. Pumphrey, and W.G. Read (2011). “Aura Microwave Limb Sounder observations of the polar middle atmosphere: Dynamics and transport of CO and H₂O”. In: *J. Geophys. Res.* 116.D05110. DOI: doi:10.1029/2010JD014608 (cit. on p. 7).
- Lee, K., Z. Li, Y. Kim, and A. Kokhanovsky (2009). “Atmospheric Aerosol Monitoring from Satellite Observations: A History of Three Decades”. In: pp. 13–38. ISBN: 978-1-4020-9673-0. DOI: 10.1007/978-1-4020-9674-7_2 (cit. on p. 14).
- Lorentz, H.A. (1906). “The absorption and emission lines of gaseous bodies”. In: *KNAW, Proceedings, 8 II, 1905-1906, Amsterdam*, pp. 591–611 (cit. on p. 21).
- Lossow, S. et al. (2019). “The SPARC water vapour assessment II: profile-to-profile comparisons of stratospheric and lower mesospheric water vapour data sets

- obtained from satellites”. In: *Atmospheric Measurement Techniques* 12.5, pp. 2693–2732. DOI: 10.5194/amt-12-2693-2019 (cit. on pp. 8, 10).
- Marsh, D.R., M.J. Mills, D.E. Kinnison, J.-F. Lamarque, N. Calvo, and L.M. Polvani (2013). “Climate Change from 1850 to 2005 Simulated in CESM1(WACCM)”. In: *Journal of Climate* 26.19, pp. 7372–7391. DOI: 10.1175/JCLI-D-12-00558.1 (cit. on p. 5).
- Minschwaner, K. et al. (2010). “The photochemistry of carbon monoxide in the stratosphere and mesosphere evaluated from observations by the Microwave Limb Sounder on the Aura satellite”. In: *J. Geophys. Res.* 115.D13303. DOI: doi:10.1029/2009JD012654 (cit. on p. 7).
- Murtagh, D. et al. (2002). “An overview of the Odin atmospheric mission”. In: *Can. J. Phys.* 80.4, pp. 309–319. DOI: 10.1139/p01-157 (cit. on pp. 16, 17).
- Ray, E. A., M. J. Alexander, and J. R. Holton (1998). “An analysis of the structure and forcing of the equatorial semiannual oscillation in zonal wind”. In: *Journal of Geophysical Research: Atmospheres* 103.D2, pp. 1759–1774. DOI: 10.1029/97JD02679 (cit. on p. 10).
- Rodgers, C.D. (2000). “Inverse methods for atmospheric sounding: Theory and practise”. In: *World Scientific Publishing, 1st edition* (cit. on p. 24).
- Rydberg, B., P. Eriksson, J. Kiviranta, J. Ringsby, A. Skyman, and D. Murtagh (2017). “Algorithm Theoretical Basis Document: Level 1 Processing”. In: *Technical report, Chalmers University of Technology* (cit. on p. 18).
- Shepherd, T.G. (2000). “The middle atmosphere”. In: *Journal of Atmospheric and Solar-Terrestrial Physics* 62.17, pp. 1587–1601. ISSN: 1364-6826. DOI: [https://doi.org/10.1016/S1364-6826\(00\)00114-0](https://doi.org/10.1016/S1364-6826(00)00114-0) (cit. on p. 9).

Part II

Appended papers

Paper 1

Recovery and validation of Odin/SMR long term measurements of mesospheric carbon monoxide

Francesco Grieco, Kristell Pérot, Donal Murtagh, Patrick Eriksson, Peter Forkman, Bengt Rydberg, Bernd Funke, Kaley A. Walker, and Hugh C. Pumphrey

Atmospheric Measurement Techniques, 13, 1-20,
<https://doi.org/10.5194/amt-13-1-2020>,
accepted, 2020.



Recovery and validation of Odin/SMR long-term measurements of mesospheric carbon monoxide

Francesco Grieco¹, Kristell Pérot¹, Donal Murtagh¹, Patrick Eriksson¹, Peter Forkman¹, Bengt Rydberg², Bernd Funke³, Kaley A. Walker⁴, and Hugh C. Pumphrey⁵

¹Department of Space, Earth and Environment, Chalmers University of Technology, Gothenburg, 412 96, Sweden

²Molflow, Gråbo, 443 40, Sweden

³Instituto de Astrofísica de Andalucía, CSIC, Granada, Spain

⁴Department of Physics, University of Toronto, Toronto, M5S 1A7, ON, Canada

⁵School of Geosciences, University of Edinburgh, Edinburgh, EH9 3FF, UK

Correspondence: Francesco Grieco (francesco.grieco@chalmers.se)

Received: 19 February 2020 – Discussion started: 4 March 2020

Revised: 7 July 2020 – Accepted: 31 July 2020 – Published:

Abstract. The Sub-Millimetre Radiometer (SMR) on board the Odin satellite performs limb sounding measurements of the middle atmosphere to detect molecular emission from different species. Carbon monoxide (CO) is an important tracer of atmospheric dynamics at these altitudes, due to its long photochemical lifetime and high vertical concentration gradient. In this study, we have successfully recovered over 18 years of SMR observations, providing the only dataset to date being so extended in time and stretching out to the polar regions, with regards to satellite-measured mesospheric CO. This new dataset is part of the Odin/SMR version 3.0 level 2 data. Much of the level 1 dataset – except the October 2003 to October 2004 period – was affected by a malfunctioning of the phase-lock loop (PLL) in the front end used for CO observations. Because of this technical issue, the CO line could be shifted away from its normal frequency location, causing the retrieval to fail or leading to an incorrect estimation of the CO concentration. An algorithm was developed to locate the CO line and shift it to its correct location. Nevertheless, another artefact causing an underestimation of the concentration, i.e. a line broadening, stemmed from the PLL malfunctioning. This was accounted for by using a broader response function. The application of these corrections resulted in the recovery of a large amount of data that was previously being flagged as problematic and therefore not processed. A validation study has been carried out, showing how SMR CO volume mixing ratios are in general in good accordance with the other instruments considered in the study. Overall, the agree-

ment is very good between 60 and 80 km altitude, with relative differences close to zero. A positive bias at low altitudes (50–60 km) up to +20 % and a negative bias up to –20 % at high altitudes (80–100 km) were found with respect to the comparison instruments.

1 Introduction

Of the carbon monoxide (CO) produced at surface level by anthropogenic sources (e.g. industrial activities, biomass burning, transport and heating) as well as by oceans and biogenic sources, very little is transported upwards to the stratosphere, as it is chemically destroyed by reacting with the hydroxyl radical (OH). This causes a sharp gradient in CO concentration from the troposphere to the lower stratosphere (Zander et al., 1981). The CO which can be observed in the middle atmosphere is mainly produced via two processes: methane (CH₄) oxidation and CO₂ photolysis, with the latter being the dominant one (Minschwaner et al., 2010). In particular, high altitudes are characterised by strong fluxes of radiation in the Schumann–Runge bands and continuum and Lyman- α wavelengths which are strongly absorbed by CO₂; therefore, CO₂ photolysis becomes more significant with height in the upper mesosphere and lower thermosphere, providing a major source of CO and resulting in a large vertical gradient in its concentration. CO from high altitudes is transported downwards in the winter hemisphere polar night

region due to advection and vertical eddy mixing (Solomon et al., 1985). In the mesosphere and lower thermosphere, the photochemical lifetime of CO increases with altitude from a minimum of approximately 1 week up to several hundreds of years. This lifetime is greater than the zonal transport timescale and of the same order of magnitude as the meridional and vertical transport timescales in the stratosphere up to the middle mesosphere, while it is significantly greater than all transport timescales in the upper mesosphere (Brasseur and Solomon, 2005). Because of its strong horizontal and vertical concentration gradients and due to its long lifetime, CO is commonly used as a tracer of middle atmospheric dynamics (e.g. Lee et al., 2011; de Zafra and Muscari, 2004).

Measurements of CO in the mesosphere have been carried out since the end of the 1970s using ground-based instruments (Clancy et al., 1982) and later on with satellites such as UARS/ISAMS (Allen et al., 1999). More recent satellite measurements are the ones performed in the microwave band with Aura/MLS (e.g. Froidevaux et al., 2006), as well as in the infrared with Envisat/MIPAS (e.g. Funke et al., 2009) and SCISAT-1/ACE-FTS (e.g. Clerbaux et al., 2008). The first retrieval results from CO measurements obtained with the Sub-Millimetre Radiometer (SMR) on board Odin were presented by Dupuy et al. (2004). They observed seasonal variations of CO concentration related to global circulation and chemical processes as predicted from the Whole Atmosphere Community Climate Model (WACCM), to which they compared their results obtaining an overall agreement within 2 orders of magnitude. Also, good agreement has been obtained comparing with observations from UARS/ISAMS.

There are not many studies about Odin/SMR measurements of CO, although such measurements have been performed from August 2001 until today. This is due to a malfunctioning of the phase-lock loop (PLL) in the front end used for CO observations, which caused the majority of CO data to present artefacts which made them unusable for retrievals. The issue is illustrated in Sect. 2 together with a description of Odin/SMR. In Sect. 3 we explain how we implemented a correction for the artefacts caused by the PLL malfunctioning and other issues which arose during the retrieval process. As a result, retrieval products from over 18 years of Odin/SMR CO observations, between 50 and 100 km altitudes, are now available and presented in Sect. 4. They are part of the Odin/SMR v3.0 L2 dataset. Finally, for validation purposes, in Sect. 5 we compare Odin/SMR profiles with those from Envisat/MIPAS, SCISAT-1/ACE-FTS and Aura/MLS, being the satellite instruments operating at the same time as SMR and observing similar altitudes. We also present comparisons with ground-based measurements from the Onsala Space Observatory.

2 Odin/SMR CO measurements

2.1 The Sub-Millimetre Radiometer

The Odin satellite, a Swedish-led project in collaboration with Canada, France and Finland, was launched on 20 February 2001 into a 600 km sun-synchronous orbit with inclination 97.77° and 18:00 LT ascending node. Its observation time was shared between astronomical and atmospheric observations until 2007, when the astronomical part of Odin's mission was concluded. After that, the instruments on board Odin have been used exclusively for limb sounding of the atmosphere. These instruments are OSIRIS (Optical Spectrograph and InfraRed Imaging System) and SMR. In this article, we are using the latter. The four sub-millimetre receivers in SMR can be tuned to cover frequencies between 486–504 and 541–581 GHz, thus to observe emission due to rotational transitions for species such as O_3 , H_2O , CO, NO, ClO, N_2O and HNO_3 in the stratosphere and mesosphere (e.g. Frisk et al., 2003). There is also a millimetre receiver to observe the 118 GHz O_2 transition. The cold sky and a hot load are repeatedly observed for calibration purposes (see Fig. 1). A Dicke switch allows us to quickly change the source of the signal between the main beam and the calibrators. The signal is thereafter split according to polarisation and injected into the mixer through a Martin–Puplett interferometer. Here the source signal is converted to longer wavelengths by combining it with a local oscillator (LO) signal, also injected through the Martin–Puplett interferometer. The frequency of the LO is fine tuned with the use of a PLL. The output signal of the mixer is a function of the sum and difference of the frequencies of the input signals, therefore consisting of two sidebands. SMR is however run in single sideband mode so, of the two sidebands, only the one containing the signal of interest will be detected and the other one suppressed. This is achieved, before mixing, by accordingly setting the length of the arms of the Martin–Puplett interferometer. The resulting signal can then be amplified and routed to the autocorrelator spectrometers (AC1 and AC2, as indicated in Fig. 1).

Measurements are performed during both upward and downward vertical scanning with a vertical sampling of ~ 6 km in the mesosphere. The scanning is continuous, with a constant speed of 0.75 km s^{-1} . Odin/SMR L1 data are organised in scans, each of them consisting of a group of spectra collected during a single upward (or downward) scanning. Each spectrum corresponds to a single mean tangent altitude in the range 7–72 km (stratospheric scans), 7–110 km (strato-mesospheric scans) or 60–110 km (mesospheric scans) (Dupuy et al., 2004).

2.2 SMR CO operational modes

Odin/SMR measures CO, with a 3–7 km vertical resolution, from the thermal emission line corresponding to the $J = 5 \rightarrow 4$ rotational transition at 576.268 GHz. In Fig. 2a

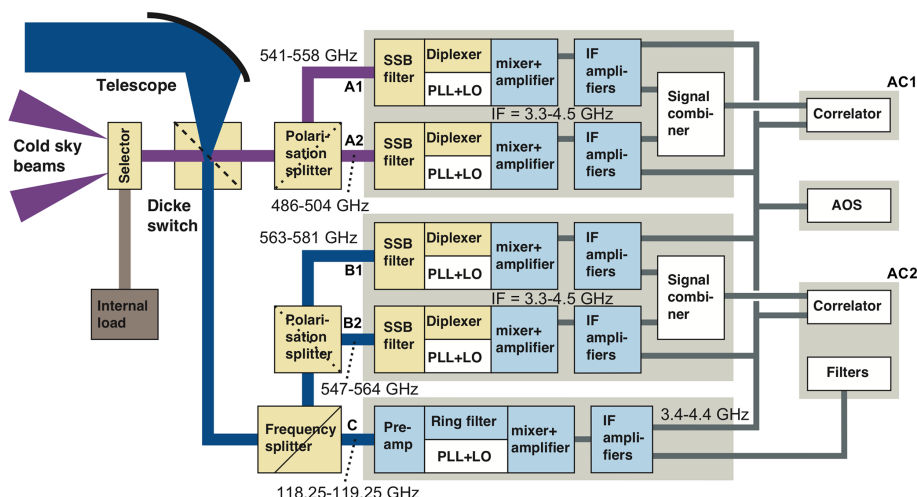


Figure 1. Block diagram of the Odin radiometer. From Frisk et al. (2003).

we show an illustrative scan of spectra obtained in normal conditions where both a CO line and an O₃ line are measured. The SMR receivers can be adjusted to different configurations called frequency modes (FMs), each of which corresponds a certain observed frequency band and a scheduled observation time. There are three FMs that cover bands in which the above-mentioned CO transition is observed. Their characteristics are summarised in Table 1. All these measurements are carried out by using the B1 front end (the set of components thus denoted in Fig. 1), whose PLL element was working correctly for a year only, between 8 October 2003 and 8 October 2004. The measurements made during the rest of the Odin operational time, from 2001 until today, have all been affected by a malfunctioning of this PLL, leading to a shift of the LO frequency from its nominal value (Rydberg et al., 2017). Consequently each scan presents a different frequency shift. In extreme cases like the one shown in Fig. 2b, the frequency shift causes the CO line to fall outside the observed bandwidth, and thus the data are unrecoverable.

3 Recovery and retrieval

We explain here how we developed a frequency correction which was applied to the spectra before the retrieval process, leading to the recovery of a great part of the dataset. This is followed by descriptions of the set-up for the v3.0 CO retrievals and of the method used to estimate line broadening generated by the PLL failure.

3.1 Basic frequency correction

In order to correct the frequency shift, as a first step, the centre frequency of the CO line in the scan's average spectrum has been compared with the theoretical centre frequency. The resulting difference is then applied to the LO frequency. To

do that, the correction algorithm first needs to distinguish the CO line from the O₃ line. In Fig. 3a it is shown how peak brightness temperatures of CO and O₃ lines vary with altitude. Here it can be noticed that the CO and O₃ slopes are most different between 40 and 60 km, allowing us to discern between the two species. In Fig. 3b, averaging of observations during the PLL working period show that, in this altitude range, a $-0.0004 \pm 0.001 \text{ K m}^{-1}$ slope corresponds to the CO line, while the value $-0.009 \pm 0.003 \text{ K m}^{-1}$ identifies the O₃ line, where the uncertainties on slopes correspond to 3σ . Thus, the correction algorithm associates peak T_b gradients with a value higher than -0.0045 K m^{-1} to the CO line. The LO frequency can then be corrected for the whole altitude range under consideration in this study, as explained above. If no line or only the O₃ line is found, the scan is not considered for further processing.

Despite the application of this first correction to the data, they still present artefacts that need to be corrected. In fact, as can be seen in Fig. 4a, all spectra in a single scan, each corresponding to a different altitude, present a different frequency shift. This suggests that the PLL malfunctioning affects the observation at a timescale smaller than the scanning timescale ($\sim 2 \text{ min}$). Thus applying the same correction to each spectrum in a scan is not sufficient. To solve this problem, we modified the pre-correction algorithm by considering each single-altitude spectrum and estimating the observed centre frequency of each CO line by fitting them with a Gaussian function. We then compared these values to the theoretical centre frequency and therefore applied a different shift to each spectrum. An example of result obtained from this correction is shown in Fig. 4b. Including this altitude-dependent correction resulted in a significantly increased amount of data that could be recovered, i.e. from which CO concentration profiles could be derived (as shown in Fig. 7 in Sect. 4). The frequency shifts, of which we pre-

Table 1. FMs for observing CO. From Rydberg et al. (2017).

Frontend	Spectrometer	LO freq. (GHz)	Freq. range (GHz)	Species	FM
572 B1	AC2	572.762	576.062–576.862	CO, O ₃	14
		572.964	576.254–576.654 577.069–577.469	CO, O ₃ HO ₂ , ¹⁸ O ₃	22
	AC1	572.762	576.062–576.862	CO, O ₃	24

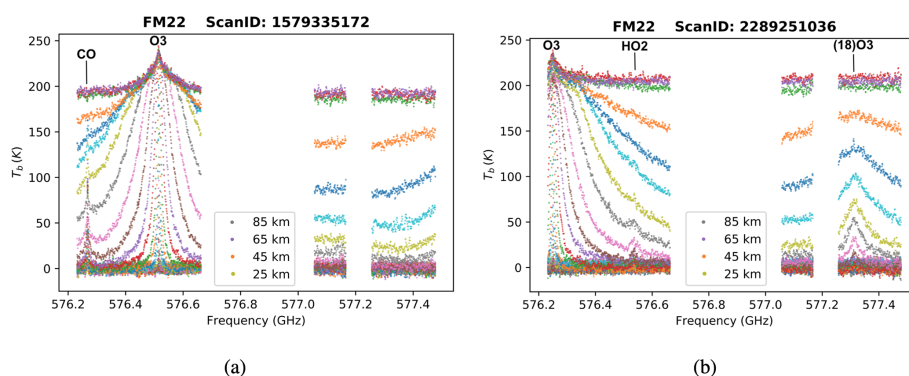


Figure 2. Spectra for altitudes ranging from 7 to 110 km for two scans taken as examples. The bigger gap in the spectra around 576.8 GHz is due to the particular way the bands are arranged to cover the desired frequencies for FM22, while the smaller gap at 577.2 GHz is due to instrumental failure relative to one sub-band. In (a) both CO and O₃ lines are present and at the expected frequency. In (b) the frequency shift is so big that only the O₃ can be observed (shifted), while the CO line is shifted outside of the band and therefore not observed. Colours corresponds to different tangent altitudes within the reported scan. Not all altitudes are indicated in the legend for the sake of readability.

sented the corrections in this section, appear to be random and not follow any trend with time. No dependency on satellite temperature was observed either.

3.2 Retrieval set-up

The Atmospheric Radiative Transfer Simulator (ARTS) retrieval algorithms are based on the optimal estimation method (Rodgers, 2000) from which statistical errors on the retrieved quantities originate. A new version of the ARTS operational processing system has been developed for SMR retrievals. The data produced by this system will be denoted as version 3.x. The new retrieval system will be described in detail in a forthcoming publication, but a summary is provided below. The CO data discussed in this work have been assigned version number 3.0.

The new processing system is based on a MySQL database and is capable of distributing the calculations over multiple clusters. The actual retrievals are based on ARTS (Buehler et al., 2018). For the moment ARTS version 2.3.564 is applied. Besides atmospheric radiative transfer, the forward simulations consider the sensor's antenna response, double-sideband characteristics and spectrometer frequency response, using the approach of Eriksson et al. (2006). ARTS provides the needed weighting functions (mainly using analytical expressions), while the inversion of optimal estima-

tion type is made in MATLAB by code taken from Eriksson et al. (2005).

The L2 data provided contain a characterisation of the retrieval, following Rodgers (2000). As described in Baron et al. (2002), when retrieving multiple quantities in parallel, the “smoothing error” includes terms that describe the interference between the quantities. The retrieval error reported in SMR v3.0 data incorporates this cross-quantity interference but excludes the classical smoothing error internal to the quantity. For example, the error reported for CO considers that the retrieval of instrumental parameters is nonideal but excludes the direct smoothing of the CO profile due to limitations in vertical resolution. In this way, the reported error matches the standard one that would be obtained if the instrumental parameters would instead be treated as forward model uncertainties (though strictly true only for a totally linear inversion problem).

Specifics for the retrievals presented in this paper include that only spectra recorded at tangent altitudes between 40 and 100 km are considered to form a mesospheric retrieval mode. The spectroscopic data for the frequency range of concern is solely taken from HITRAN 2012 (Rothman et al., 2013) (but the system allows us to incorporate data from other sources). The set of variables retrieved is specified for each mode separately. In this case, the CO profile and off-sets for pointing,

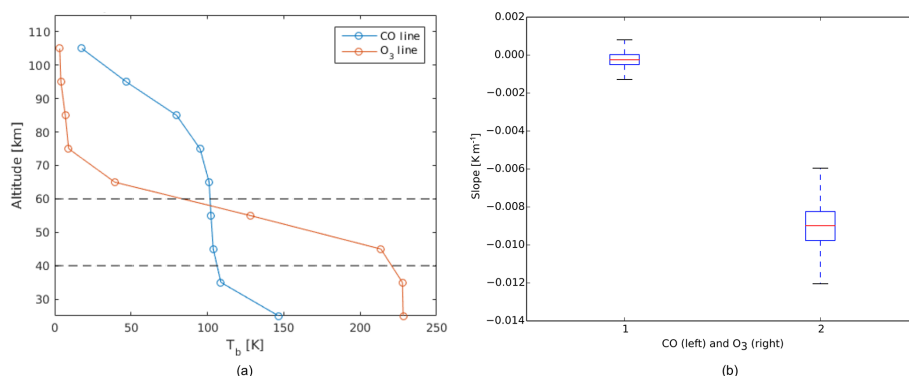


Figure 3. (a) Peak brightness temperatures of CO and O₃ at different altitudes. Average considering all observations performed during the PLL working period, i.e. 14 224 scans. At altitudes between 40 and 60 km, the CO line curve presents a steeper slope. (b) Linear fit of slopes of peak brightness temperatures between 40 and 60 km altitude for CO and O₃. The shown uncertainties on slopes correspond to 3σ .

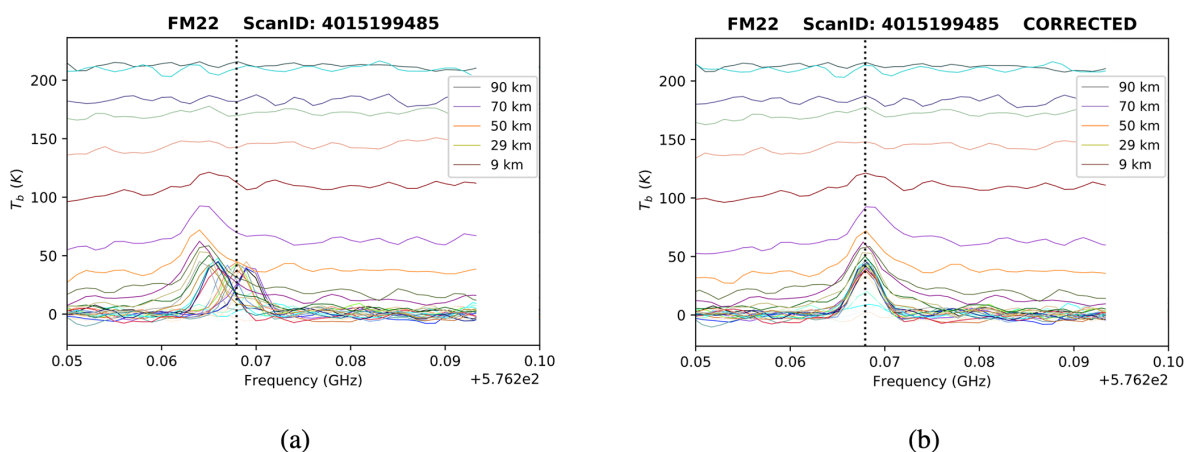


Figure 4. Spectra measured on 2 February 2009 presenting altitude-dependent frequency shifts before (a) and after (b) altitude-dependent correction. Colours corresponds to different tangent altitudes within the reported scan. Not all altitudes are indicated in the legend for the sake of readability.

frequency and brightness temperature zero level (baseline) are retrieved.

The a priori dataset previously used for Odin/SMR CO retrievals was found outdated and inaccurate. As a consequence, for the new inversions, a new CO climatology was formed, based on MIPAS zonal means averaged over the years separately for each month. For this purpose, we are using the product V5R_CO_521, which at the moment is the most recent data version from MIPAS middle atmosphere observation mode (Garcia et al., 2014) (see Sect. 5.1). The monthly a priori is divided into 10° latitude bins. As a temperature model for the retrieval, ERA-Interim reanalysis data (Dee et al., 2011) are used up to 60 km and the Mass Spectrometer Incoherent Scatter model (version NRLMSISE-00; Picone et al., 2002) is used from 70 km upwards. Between 60 and 70 km, a spline interpolation of the two is applied.

In Fig. 5 the retrieval for a typical scan is shown. Despite the fact that spectra above 40 km tangent altitude are considered in the inversion, only measurements above 50 km are re-

liable since at lower altitudes it is not possible to discern the CO line from the noise. Moreover, data with a measurement response lower than 0.75 are discarded, where the measurement response is a measure of the degree to which the result may be contaminated by the a priori. It is defined as the sum over the row of the averaging kernel matrix (Rodgers, 2000). Values lower than 0.75 occur for the retrieved profile above 100 km which is dominated by the a priori and is here shown out of completeness, together with the averaging kernel extending to higher altitudes, to display how retrieved concentrations between 90 and 100 km are also influenced by higher altitudes.

3.3 Broadening correction

The fits of the CO line performed during the inversion process – which have the shape of a Gaussian function due to Doppler broadening – have significantly different amplitude and width compared to the observed line, causing an

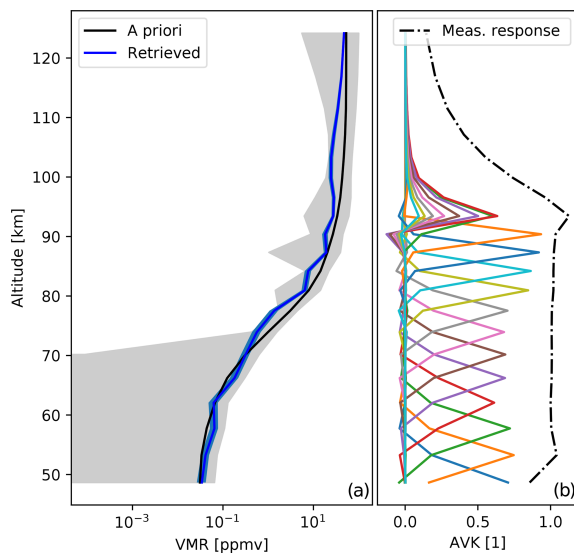


Figure 5. Example retrieval referring to ScanID 1579335172 from FM22. **(a)** Retrieved concentration profile and error (in blue) and a priori including uncertainties (in grey). **(b)** Averaging kernels plotted in a different colour for each altitude (not indicated) and measurement response.

underestimation of the concentration. This suggests that the PLL malfunctioning even has an effect within the integration time, causing the observed line to be broadened with respect to what it would be in normal instrumental conditions. To take into account this broadening issue during the inversion, the original response function, a Gaussian function with $\sigma = 0.8$ MHz, has been replaced with a Gaussian function with a higher σ value. The response function $w_{\text{ch}}^i(\nu)$ of a spectrometer's channel i represents how the power of a signal $I(\nu)$ is weighted:

$$y_i = \int_0^\infty I(\nu) w_{\text{ch}}^i(\nu) d\nu \quad \text{with} \quad \int_0^\infty w_{\text{ch}}^i(\nu) d\nu = 1, \quad (1)$$

where y_i is the final, calibrated antenna temperature of the channel i (Eriksson et al., 2006).

Figure 6a shows the relative difference between the Gaussian area beneath the observed CO line and the Gaussian area beneath the fit, for a scan in the period when the PLL was working. Here there is no need for correction, and the lower values of the relative area difference are obtained with the original response function. As an example, in Fig. 6b the relative area difference for one scan in the PLL malfunctioning period after 8 October 2004 is plotted. During this period, the most suitable response function is a Gaussian function with $\sigma = 1.1$ MHz. This is indeed the one resulting in the lowest overall relative area differences; therefore, this same response function has been used in the whole period aforementioned.

Note that the original response function is still the one giving the best results during the period before 8 October 2003. Consequently, the new response function has been applied only to inversions after 8 October 2004. This suggests that the PLL malfunctioning before 8 October 2003 is of a different nature than the one after 8 October 2004, with the former causing only frequency shifts and the latter causing both line broadenings and frequency shifts, i.e. having effects both within the integration time and at longer timescales.

4 The new dataset

The recovered dataset is part of the Odin/SMR v3.0 L2 data. As mentioned in Sect. 3, the new frequency correction algorithm also helped to recover many data that were previously being erroneously flagged, so that there is a very significant increase in the amount of CO level 2 data that are now available. This can be seen in Fig. 7, showing the temporal distribution of the L1 and L2 datasets before and after the application of the correction algorithm, for the three CO observation modes together. The results are very satisfying, with 63 % of the data being successfully processed (compared to 8 % before the correction) until September 2017. The remaining data are discarded due to other quality flags. After this date, the frequency shift is causing the CO line of almost all the spectra to be outside of the observed band, resulting in the loss of most of the CO data during this time period, hence the almost total absence of L2 data from then on. The very high number of measurements performed with CO FMs during July 2002, July 2003 and August 2004 corresponds to special scheduling of the observation time, set to monitor dynamics in the northern summer mesosphere associated with the study of noctilucent clouds (Karlsson et al., 2004).

The time series shown in Fig. 8 gives an overview of the new CO dataset, extended to cover the whole globe including the polar regions. They consist of monthly zonal means of CO volume mixing ratios over five different latitude bands. The white bands correspond to months during which the number of scans in the given latitude band is lower than 10. No concentrations are shown for some months in the early years of the mission, despite the presence of sufficient L2 data, because of plotting interpolation with adjacent months with no data (see Fig. 7). No significant difference between the various FMs is observed (not shown). CO volume mixing ratios show noticeable variations with altitude, latitude and season, as well as longer-term variations. We observe a sharp increase with height, due to the photodissociation of CO_2 at high altitudes, as explained in Sect. 1. In these plots, it is also possible to notice the temporal variation of CO in the mesosphere throughout the years. In the tropics, maxima appear at equinoxes and minima at solstices. This is explained by the semiannual oscillation (SAO) signal, which dominates at low latitudes (Lee et al., 2018). Although the SAO-induced variations in zonal mean vertical wind are too small to be

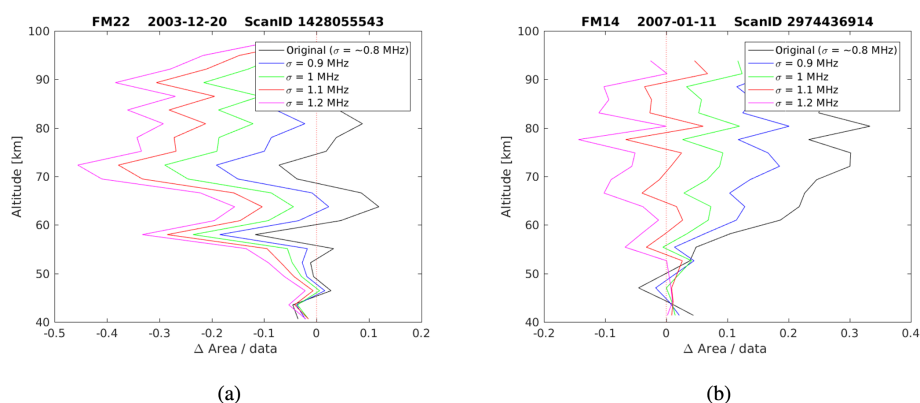


Figure 6. Relative difference between the Gaussian area beneath the observed CO line and the Gaussian area beneath the fit, obtained with different response functions for a scan in the PLL working period (a) and non-working period (b). The best response functions for the two cases are, respectively, the original one (black line) and the one with $\sigma = 1.1$ MHz (red line).

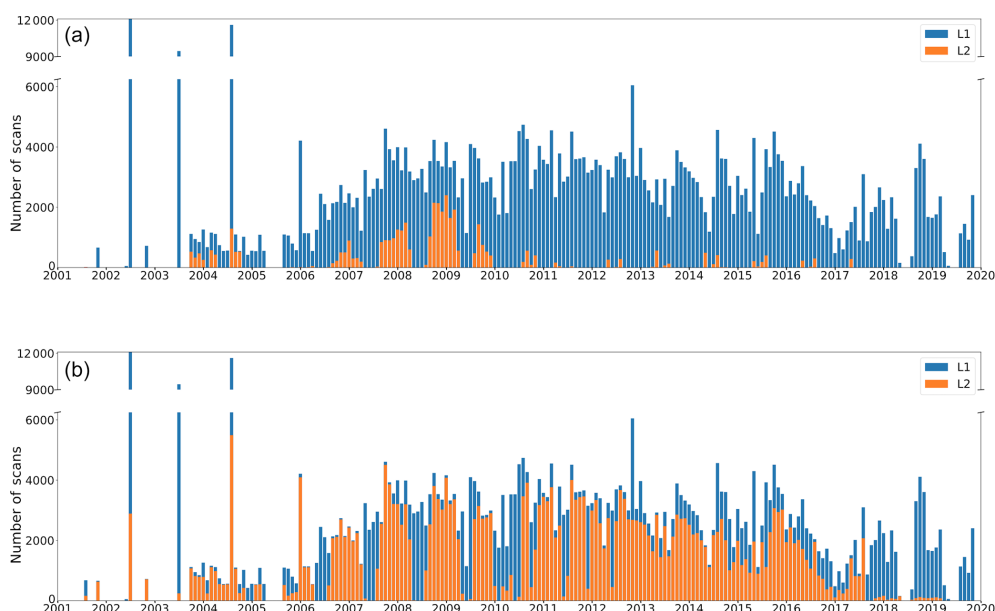


Figure 7. Number of L1 and L2 scans by month for FM14, FM22 and FM24 altogether, before (a) and after (b) the application of the correction algorithm. The ticks on the x axis correspond to 1 January for each year. This figure gives an overview of how much data could be recovered.

measured directly, the accumulated effects can be seen in the distribution of the long-lived constituents like CO (Hamilton, 2005). Sinking of air, or at least anomalously weak rising motion, leads to the observed increase in the CO mixing ratios around the equinoxes. At high latitudes, the seasonal variations are mainly characterised by the downward transport of CO-rich air in winter, from the upper mesosphere to the stratopause, induced by the meridional circulation. The CO volume mixing ratio values measured in summer are lower, due to upward circulation. The SAO signal is noticeable at high latitudes too, explaining the secondary minima that are visible in the middle of the winter (Lee et al., 2018). The seasonal variations at mid-latitudes are similar, though

the effect of the meridional circulation is significantly less pronounced than at high latitudes. Moreover, at high latitudes in the Northern Hemisphere, a particularly strong secondary peak in CO concentration appears during several of the winters. This is observed in particular in 2006, 2009, 2013 and 2019. As seen in Fig. 8, unusually high volume mixing ratio values were measured in the mid- and lower mesosphere, in those years, in late winter. Such a pattern is generated by sudden stratospheric warming (SSW) events followed by an elevated stratopause event. SSWs occur almost entirely in the Northern Hemisphere, during wintertime, and consist of warmings of the stratosphere at high latitudes by several tens of kelvins, occurring within a few days. This is caused

by planetary waves disturbing the polar vortex (e.g. Charlton and Polvani, 2007), thus reducing the descent of CO-rich air from higher altitudes. After such an event, the vortex recovers, and the stratopause sometimes reforms at higher altitudes than normal (Vignon and Mitchell, 2015), as it has already been observed by Odin/SMR (Pérot et al., 2014). In such a case, the downward-transported air will come from higher altitudes (Orsolini et al., 2017), where CO is more abundant, resulting in the above-mentioned higher concentration peak in late winter (Manney et al., 2009). Finally, it can be seen that, in all latitude bands, concentrations are in general higher during the period 2012–2016, in accordance with corresponding more intense solar activity. The described temporal variations are consistent with observations from other satellite instruments, such as MLS (Lee et al., 2018) and MIPAS (Funke et al., 2009; Garcia et al., 2014).

5 Comparison with other instruments

In this section we compare the SMR v3.0 CO dataset with data from other limb sounding satellite-borne instruments, namely MIPAS, ACE-FTS and MLS, and with ground-based measurements made by a radiometer located at the Onsala Space Observatory (OSO). Our goal is to assess the quality of the new dataset described above. With regards to satellite measurements, the comparison is performed between measurements that occurred within a maximum temporal separation of 24 h and a maximum spatial separation of 500 km. It is possible to use such broad coincidence criteria because of CO's long chemical lifetime in the mesosphere (Menschwaner et al., 2010). CO in the mesosphere and lower thermosphere (MLT) is affected by tidal mixing (Garcia et al., 2014), which might contribute to the biases observed in comparisons with such a broad temporal coincidence criterion. To investigate if this is the case, we also carried out comparisons with 3 and 6 h coincidence criteria. When not characterised by the absence of sufficient coincidences (i.e. less than 10), these comparisons do not present biases which are significantly different from the 24 h ones. No plot is shown for the 3 and 6 h comparisons. All the validation plots shown hereafter refer to 24 h coincidences.

CO vertical concentration profiles do not feature particular structures which would justify taking into account the satellite instruments' different vertical resolutions, also considering that such differences are not as marked as the ones between SMR and OSO (coincidence criteria and smoothing process for the SMR–OSO comparison are presented in Sect. 5.4). The comparison between space-borne instruments has therefore been performed simply by linearly interpolating each coincident profile over a common 1 km altitude grid, ranging from 50 to 100 km. Given a couple of coincident measurements denoted with i , the absolute difference of the two at altitude z will be given by

$$\delta_{\text{abs},i}(z) = x_{\text{SMR}} - x_{\text{comp}} \quad (2)$$

and the relative difference

$$\delta_{\text{rel},i}(z) = \frac{x_{\text{SMR}} - x_{\text{comp}}}{(x_{\text{SMR}} + x_{\text{comp}})/2}, \quad (3)$$

where x_{SMR} and x_{comp} are respectively the CO mixing ratios measured from SMR and the comparison instrument at altitude z for the coincidence i . The relative difference has as its denominator the mean of the two concentrations. This is done because, being both satellite measurements, they can both be affected by large uncertainties and none of the two is preferable as a reference (Randall et al., 2003). To minimise the weight of outliers, the median difference $\Delta(z)$ over all the $N(z)$ coincidences at altitude z is calculated. The dispersion of the results is represented by the standard deviation of the median, calculated as follows:

$$\text{SEM}(z) = \frac{1}{\sqrt{N(z)}} \sqrt{\frac{1}{N(z)-1} \sum_{i=1}^{N(z)} (\delta_i(z) - \Delta(z))^2}. \quad (4)$$

This is valid for both absolute and relative difference. The average and standard error of the concentration profiles are calculated using the same method. For the sake of clarity, in the following subsections we only show vertical profiles averaged over all the found coincidences, regardless of time or location. However, figures showing the relative differences between SMR and the other limb sounders as a function of altitude and latitude, for each season, have been included in the appendix and will be regularly referred to throughout the text.

5.1 MIPAS

The Michelson Interferometer for Passive Atmospheric Sounding (MIPAS) is a mid-infrared spectrometer which was launched on board Envisat on 1 March 2002 and was operating until April 2012, when an unexpected loss of contact with the satellite occurred. The satellite travelled at 800 km altitude on a sun-synchronous orbit with a 98.55° inclination and a 22:00 LT ascending node. The concentration profiles that we use for comparison in this study are retrieved from measurements of $^{12}\text{C}^{16}\text{O}$ roto-vibrational emissions in the $v = 1 \rightarrow 0$ band around 4.7 μm , using the retrieving processor developed at the Institute of Meteorology and Climate Research (IMK) in Karlsruhe and the Instituto de Astrofísica de Andalucía (IAA) in Granada (e.g. Funke et al., 2009; Sheese et al., 2016). The forward model used for CO retrieval takes into account non-LTE effects. We consider data from the most recent MIPAS datasets, as specified in Table 2 (Garcia et al., 2014, 2016). All recommendations about the quality filtering of the data have been followed (Kiefer and Lossow, 2017).

5.1.1 Nominal mode

There are two observation modes called “nominal”: one in use during the period before the interferometer in MIPAS

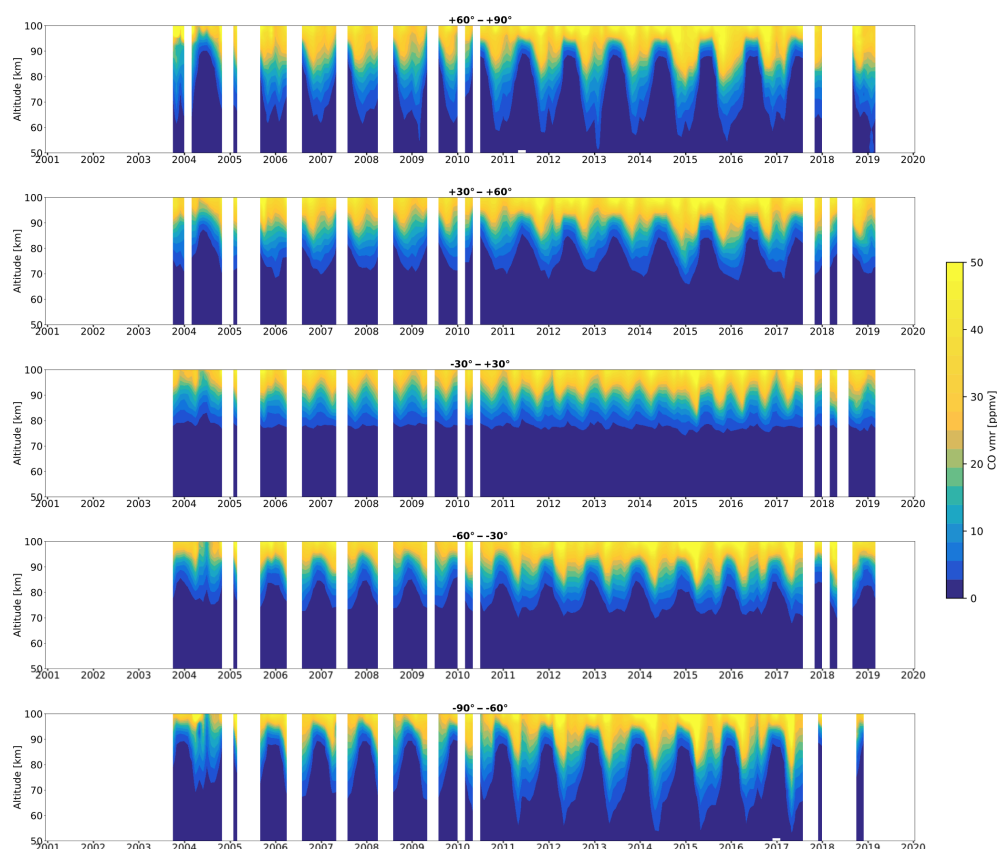


Figure 8. Time series of CO volume mixing ratios measured by SMR for different latitude bands. The white bands indicate periods during which the number of scans in the given latitude band is lower than 10. The ticks on the x axis correspond to the beginning of each year.

Table 2. Characteristics of the MIPAS CO datasets used for comparison. Vertical resolutions refer to the observations in the altitude range 50–100 km considered in this study.

Observation mode	Altitude range	Vertical resolution	Spectral resolution mode	Time period	Version
Nominal (NOM)	10–70 km	5–15 km	Full resolution (FR)	July 2002 → March 2004	V5H_CO_20
		6–16 km	Optimised	January 2005 →	V5R_CO_220
Middle atmosphere (MA)	20–100 km	5–15 km	resolution (OR)	April 2012	V5R_CO_521
Upper atmosphere (UA)	42–150 km	5–12 km			V5R_CO_621

started malfunctioning, when the instrument was being used in full spectral resolution (FR mission); and one in use after the instrument was recovered and brought back to function with a reduced spectral resolution (OR mission) (Oelhaf, 2008).

Regarding the FR-NOM mode, with the above-mentioned coincidence criteria we found 6088 coincident measurements with SMR over the period July 2002–March 2004. The profiles and differences between 50 and 70 km altitude, averaged over the whole time period and over the whole globe, are shown in Fig. 9a. The median relative difference between SMR and MIPAS has a value of +8 % at 50 km which de-

creases to reach –15 % at 60 km and eventually remains constant between 60 and 70 km altitude. No bias characterising a particular latitude or season over time has been identified for this specific comparison, since FR-NOM mode has been operational for only a short period.

Comparing with OR-NOM mode, 88 902 coincident measurements have been found over the period January 2005–April 2012. Figure 9b shows that the median relative difference between SMR and MIPAS remains positive and almost constant with altitude, staying below +15 %. The main contribution to this difference comes from latitudes between –25 and +50° – in particular during northern summer,

around $+25^\circ$, where it reaches values above $+40\%$ between 65 and 70 km. Everywhere else relative difference values remain within $\pm 20\%$ (see Fig. A1). To check if the observed differences are due to differences in vertical resolutions between the two instruments, we compared SMR and MIPAS profiles separately for daytime and nighttime observations. In fact, MIPAS vertical resolutions are similar to SMR's for daytime observations, while they are equal to more than 10 km for nighttime observations, due to lower sensitivity caused by smaller non-LTE emissions (Funke et al., 2009). The average comparison between daytime observations did not show differences that deviate significantly from the ones observed in Fig. 9 (not shown). This suggests that the observed concentration differences are not due to differences in vertical resolution.

5.1.2 Middle atmosphere mode

Another observation mode in use during the OR mission is the middle atmosphere mode, covering a larger altitude range. Its average comparison with SMR over 17 003 coincidences is shown in Fig. 9c. Both datasets are in general in good agreement with each other. It can be seen that the average difference always stays between -20% and $+20\%$. In particular, SMR presents a positive difference of around $+20\%$ at 50 km which decreases with altitude until it becomes null at 60 km. The difference keeps being negligible up until 70 km, and then it becomes negative and keeps decreasing until it reaches a minimum of -20% around 85 km, after which it goes back up to $+5\%$ at 100 km. The observed difference around 85 km is not to be attributed to MIPAS misestimation of non-LTE effects; in fact non-LTE modelling of MIPAS CO has been validated in Funke et al. (2007) and systematic errors due to non-LTE were estimated to be less than 5% . When looking at latitudes separately, the relative differences are mainly within $\pm 20\%$. The most extreme differences are observed around the northern spring equinox. Here we have very negative differences at the Equator between 70 and 80 km altitude reaching peaks of -60% . Differences of -50% can be observed during local summer in both hemispheres at high latitudes between 80 and 90 km. Also peaks of positive difference around $+60\%$ are reached at 50 km altitude at -75° and $+50^\circ$ (see Fig. A2). Considerations about daytime and nighttime comparisons carried out separately are the same as in Sect. 5.1.1.

5.1.3 Upper atmosphere mode

Figure 9d shows the comparison with OR upper atmosphere mode, averaged over 19 084 coincidences. The SMR difference in comparison with this mode is very similar to the one described in Sect. 5.1.2. A small dissimilarity is given at higher altitudes where the difference approaches zero but stays negative. Moreover, as described in Sect. 5.1.2, observed differences around 85 km are thought not to be caused

by MIPAS misestimation of non-LTE effects. At all latitudes and during all seasons, relative difference values are small and generally within $\pm 20\%$. Peaks of almost -50% are reached during the northern spring at the Equator between 70 and 80 km and during local summer in both hemispheres at high latitudes between 80 and 90 km (see Fig. A3). Considerations about daytime and nighttime comparisons carried out separately are the same as in Sect. 5.1.1.

5.2 ACE-FTS

The Fourier Transform Spectrometer (FTS) is an instrument which is part of the Canadian-led Atmospheric Chemistry Experiment (ACE) on board SCISAT-1, launched on 12 August 2003 (and still operating) into a 74° inclination orbit at 650 km altitude (Bernath et al., 2005). ACE-FTS performs solar occultation measurements in the mid-infrared. In particular, CO concentrations are retrieved from the roto-vibrational absorption bands around $4.7\ \mu\text{m}$ ($v = 1 \rightarrow 0$) and $2.3\ \mu\text{m}$ ($v = 2 \rightarrow 0$). CO retrievals are performed between 5 and 105 km altitude, with a 3–4 km vertical resolution (Boone et al., 2005, 2013). In this study we use ACE-FTS v3.6 dataset for comparison. The data have been quality filtered according to the guidelines from the instrument team (Sheese et al., 2015).

A total of 12 925 coincident CO measurements between ACE-FTS and SMR were found between February 2004 (first available ACE-FTS CO measurements) and March 2019. The number of coincidences found is lower compared with any of the MIPAS modes, despite the longer period considered. This is due to the fact that ACE-FTS is a solar occultation instrument, thus scanning the limb only twice per orbit, while both SMR and MIPAS are measuring almost continuously. The spatial and temporal average comparison with ACE-FTS is shown in Fig. 10. The relative difference decreases almost monotonically with altitude, from a maximum of $+15\%$ at 50 km to a minimum of almost -15% at the highest altitudes. In particular, the difference decreases more quickly between 50 and 60 km from 15% to near 0% . SMR and ACE-FTS are in extremely good agreement with each other between 60 and 75 km, with a relative difference close to zero. The difference then slowly decreases with altitude up to about -15% at 90 km and finally increases almost imperceptibly between 90 and 100 km. Looking at seasons separately, the relative differences present generally low values, almost always within $\pm 20\%$. Values only increase to more than $+40\%$ between 60 and 70 km during northern autumn around $+25^\circ$ and during southern winter at the Equator and around -25° . The latter difference is similar to the one observed from ACE with respect to MIPAS (Sheese et al., 2016). Moreover, strong negative differences of about -40% are observed at the Equator at 80 km altitude during northern spring and also at $+25^\circ$ during northern autumn between 80 and 90 km (see Fig. A4). Note that the majority of ACE-FTS measurements occur at latitudes higher than 60° and that the

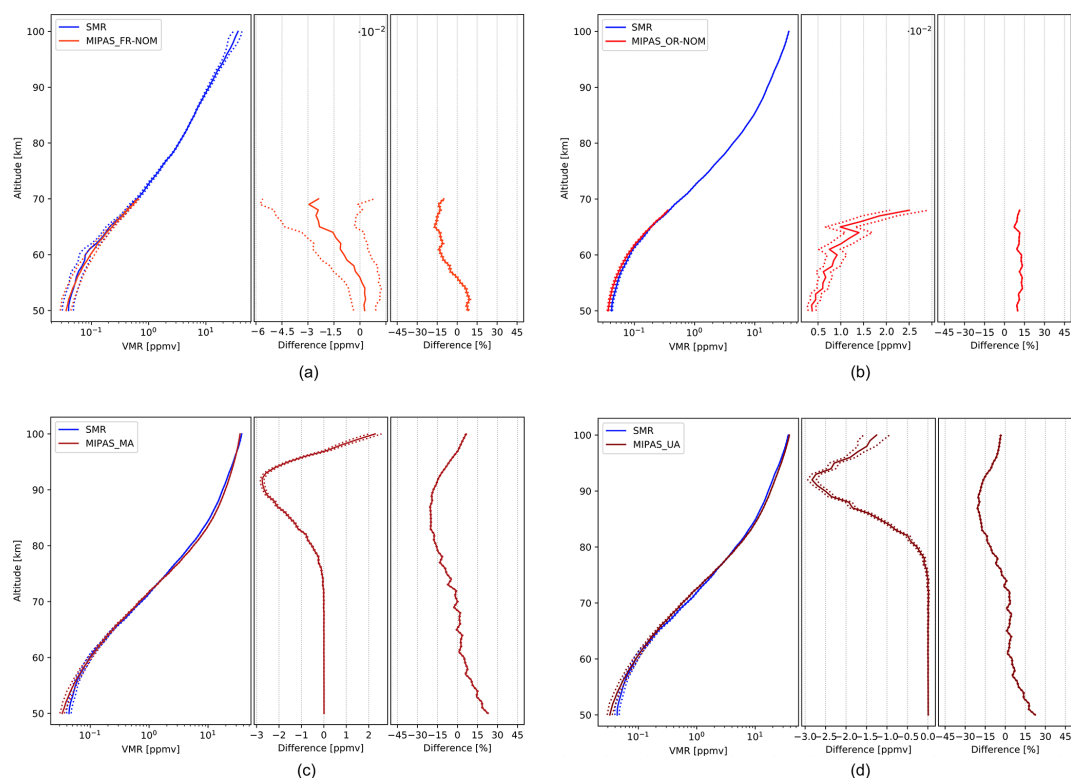


Figure 9. Comparison of SMR CO concentrations with the ones from MIPAS FR-nominal (a), OR-nominal (b), middle atmosphere (c) and upper atmosphere (d) modes. The data plotted are global averages over the whole time periods indicated in Table 2. (Left subpanels) Volume mixing ratios, expressed in parts per million by volume (ppmv). (Center subpanels) Absolute differences, expressed in ppmv. (Right subpanels) Relative differences, expressed in percentage. The dashed lines represent the standard deviation of the median which, in some cases, is smaller than the thickness of the profile line, causing the dashed line not to be distinguishable.

above-mentioned differences at low latitudes are probably related to averaging on a smaller number of coincidences.

5.3 MLS

The Microwave Limb Sounder (MLS) is an instrument on board the Aura satellite, still operating since its launch on 15 July 2004. Aura/MLS was launched on a 98° sun-synchronous orbit with 13:45 LT ascending node at an altitude of 705 km. It performs measurements between 118 GHz and 2.5 THz with a 1.5–3 km vertical resolution (Schoeberl et al., 2006; Waters et al., 2004). In this study we use MLS CO concentrations from the v4 dataset, retrieved from the $J = 2 \rightarrow 1$ rotational transition emission line at 230.5 GHz, which are considered to be reliable between 0.0046 and 215 hPa. Also, the suggested quality filtering has been performed (Livesey et al., 2018). A previous comparison between SMR and MLS CO retrievals was presented in Barret et al. (2006), based on older versions of the datasets. A validation study of the MLS CO v2 dataset has been performed by Pumphrey et al. (2007), and the differences between v2 and v4 datasets are documented in Livesey et al. (2018).

Because MLS uses the same observation technique as SMR, and because it has been functioning since 2004, a great

number of coincident measurements could be used for this validation study. Indeed, 227 820 coincidences were found between the beginning of MLS mission and March 2019. The overall average comparison of these measurements with the ones from SMR is shown in Fig. 11. A negative difference of SMR with respect to MLS characterises all of the altitude range. The relative differences are oscillating between -40% and -10% and are characterised by a significant variability. This is due to MLS CO profiles being rather jagged, as reported in Errera et al. (2019), where the MLS bias described is in accordance with what we obtain in this study. Also, the MLS–ACE bias which is reported in Sheese et al. (2016) – although referring to older versions of the two datasets – is consistent with the one we measure. The difference we measure varies significantly with latitudes and seasons: between -40° and $+40^\circ$ and below 70 km, there are peaks of -150% and -80% during northern spring and autumn, respectively; while marked negative differences are registered during local summertime in both hemispheres, getting more pronounced toward high latitudes, especially around 50 and 70 km altitude with peaks of -120% , as shown in Fig. A5 (this is also observed in the ACE–MLS comparison in Sheese et al., 2016).

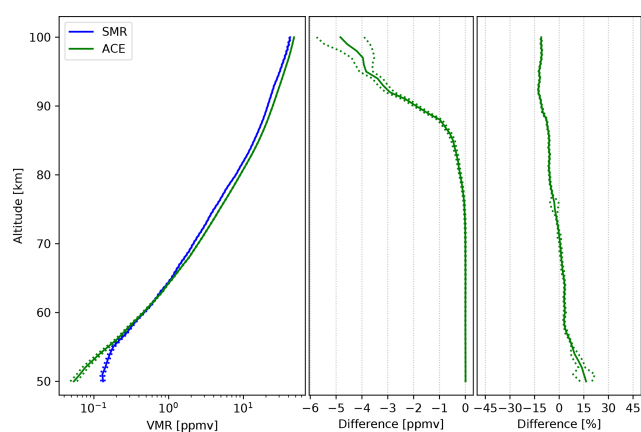


Figure 10. Comparison of SMR CO concentrations with the ones from ACE-FTS retrievals. The data plotted are global averages over the whole time between February 2004 and March 2019. Panels characteristics are the same as in Fig. 9.

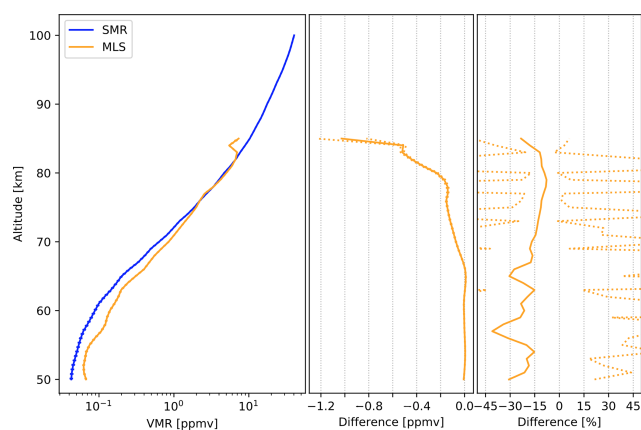


Figure 11. Comparison of SMR CO concentrations with the ones from MLS observations. The data plotted are global averages over the whole time between July 2004 and March 2019. Panels characteristics are the same as in Fig. 9.

5.4 OSO

Odin/SMR CO data are compared with data measured by a ground-based remote-sensing instrument at the Onsala Space Observatory, OSO (57.4° N, 11.9° E), during 2002–2007. The recommended quality filtering has been followed.

The OSO instrument is a frequency-switched microwave radiometer for observations of the CO $1 \rightarrow 0$ transition at 115.27 GHz. During 2002–2007, a cooled Schottky single sideband mixer was used as the first stage. In 2014 the instrument was modified to a double-sideband system with a low-noise amplifier, at ambient temperature, as the first stage. During 2002–2007 a spectrometer with 20 MHz bandwidth and a resolution of 25 kHz was used. The optimal estimation method together with the forward model ARTS, the Atmospheric Radiative Transfer Simulator (Eriksson et al., 2011),

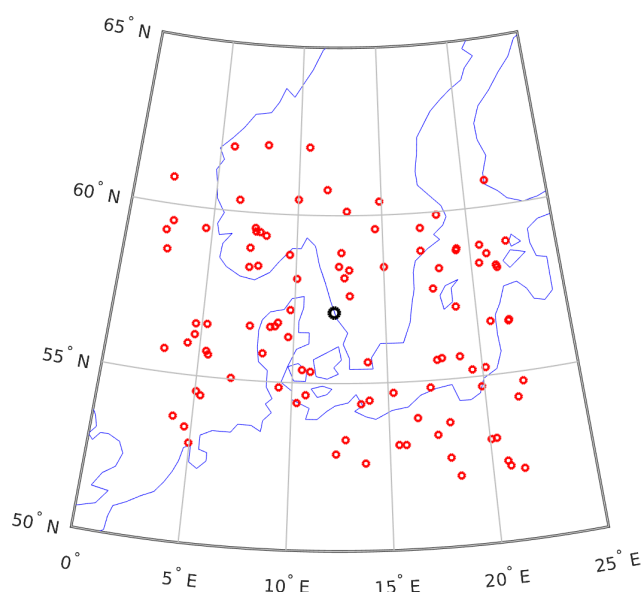


Figure 12. Odin/SMR–OSO coincidences. Red circles show the 89 coincidences during 2002–2007 and the black circle shows the OSO site.

has been used to retrieve vertical CO profiles from the measured spectra. The OSO instrument, the calibration and retrieval methods are described in Forkman et al. (2012, 2016).

Daily averages for 2002–2007 of CO profiles are retrieved from the OSO spectra. Only the 24 h average CO spectra with a signal-to-noise ratio larger than 2 are used in the retrievals. SMR data are regarded as coincident with OSO if the differences in latitude and longitude do not exceed ± 5 and $\pm 10^\circ$ respectively and if the SMR data are taken within the OSO time average periods mentioned above. For the period 2002–2007, there are 89 coincident SMR profiles (see Fig. 12).

Figure 13 shows the mean vertical CO profiles for the coincident SMR and OSO datasets. The limb sounding SMR has a much higher vertical resolution than the upward-looking OSO instrument. To compensate for this difference, the SMR profiles, x_{sat} , were convoluted with the averaging kernels, A , of the OSO instrument (Rodgers, 2000).

$$x_s = x_a + A(x_{\text{sat}} - x_a), \quad (5)$$

where x_a is the OSO a priori and x_s the smoothed SMR profile. The measurement response of SMR is very close to 1 in the 50–100 km range. The altitude range in Fig. 13 is more narrow since it is given by the range where the measurement response of the OSO instrument is > 0.75 .

OSO data from 2002–2007 have been compared to data from the satellite instruments ACE-FTS, MIPAS and MLS in a previous study (Forkman et al., 2012). As seen in Fig. 13, during this period, the difference between SMR data and the coincident averaged data from OSO was found to be of 30 % at 50 km, decreasing with altitude to reach -10 % at 60 km and remaining constant up until 90 km altitude. The standard

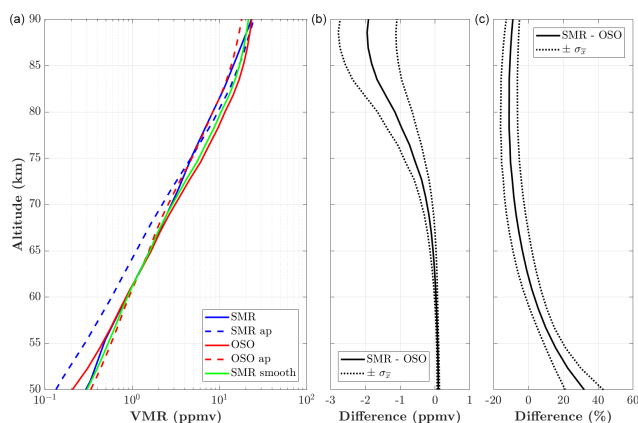


Figure 13. SMR–OSO comparison for 2002–2007. (a) Blue solid/dashed are the average SMR retrieved/a priori profiles, red solid/dashed are the average OSO retrieved/a priori profiles and green is the smoothed SMR profile. (b, c) The average difference between the smoothed SMR and OSO profiles, solid, together with the standard error of the mean, $\sigma_{\bar{x}}$, dotted, is shown in parts per million by volume and percent, respectively.

error of the mean, $\sigma_{\bar{x}}$, for the average difference between SMR and OSO is about 5 % above 55 km (see Fig. 13).

6 Conclusions

Before the application of the corrections described in this study, almost the whole Odin/SMR CO dataset was unusable due to line shifts and broadening of instrumental origin, due to the phase-lock loop malfunctioning. Line displacement resulted in the failure of inversions or inaccurate retrievals, while the instrumental broadening caused underestimation of the concentration values. We estimated and corrected the different impacts of the PLL malfunctioning on SMR CO measurements. Line shifts were addressed by developing a correction algorithm which allowed the CO lines to be repositioned to their theoretical centre, also considering different frequency shifts for each tangent altitude within a scan. This resulted in the recovery of a great part of the dataset. Line broadening was taken into account using a broader response function for the retrievals. That led to a new, good-quality, Odin/SMR v3.0 mesospheric CO dataset, covering more than 18 years of observations. Time series of the retrieved volume mixing ratios reveal variations consistent with known mesospheric dynamical patterns, such as the annual cycle of the meridional circulation, SAO, and SSWs, as well as a clear 11-year solar cycle signal. The validation study shows, on average, a good agreement with both the ground-based radiometer OSO and the three satellite-borne instruments (MIPAS, ACE-FTS, MLS) considered for comparison (see Fig. 14). In particular, between 60 and 80 km SMR agrees very well with almost all instruments, presenting relative differences close to zero. Comparisons with MI-

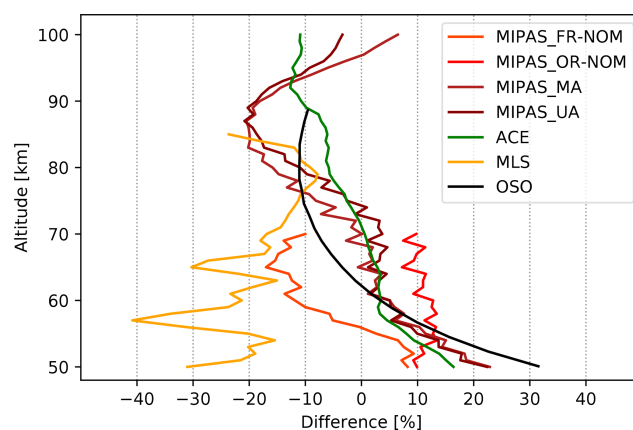


Figure 14. Summary of relative differences between SMR CO concentrations and the ones measured by all other instruments considered in this study. For the sake of clarity, errors are not shown.

PAS, ACE-FTS and OSO show a positive bias of SMR of up to +20 % at low altitudes (50–60 km) and a negative bias of up to –20 % at high altitudes (80–100 km). Something different is found with regards to MLS – i.e. negative difference at all altitudes, ranging from –40 % to –10 % – which is in accordance with the stated MLS bias (Errera et al., 2019).

To investigate if the reason for the observed differences is to be attributed to differences in vertical resolution, we smoothed SMR and comparison instrument profiles using Gaussian filters with various FWHMs. This test did not show any improvement in concentration differences (not shown), suggesting that differences in vertical resolution are not the cause of the observed biases. Other evidence for this, regarding comparisons with MIPAS modes, is given by the fact that comparisons of daytime measurements (which are characterised by similar vertical resolutions for SMR and MIPAS) do not show differences in concentration that vary from what is observed when comparing measurements all together. Moreover, systematic errors from non-LTE modelling in MIPAS measurements amount to less than 5 % (Funke et al., 2007) and are therefore not thought to be the cause for the observed SMR–MIPAS differences at high altitudes. Thus, the causes for the observed concentration differences between SMR and the comparison instruments, both globally and for different latitudes and seasons, are unknown at the moment and require further investigation.

Given its unique extension in time and geographical coverage, this new mesospheric CO dataset provides a valuable tool for further studies of mesosphere dynamics.

Appendix A

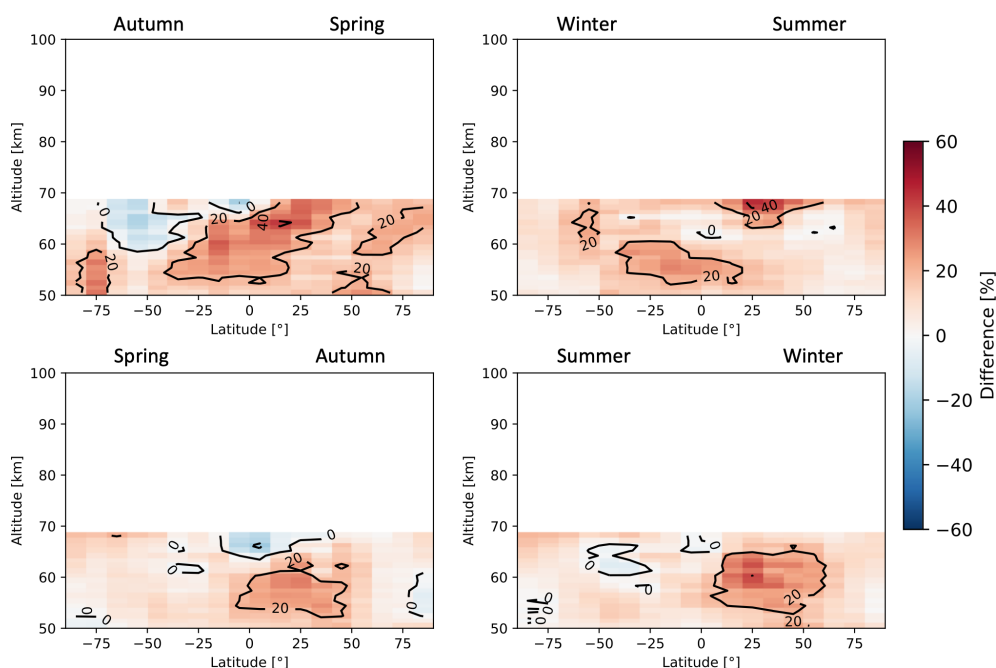


Figure A1. Seasonal zonal means of SMR–MIPAS OR–NOM relative differences averaged over the time period indicated in Table 2. The seasons are intended as the time between the solstice and the equinox.

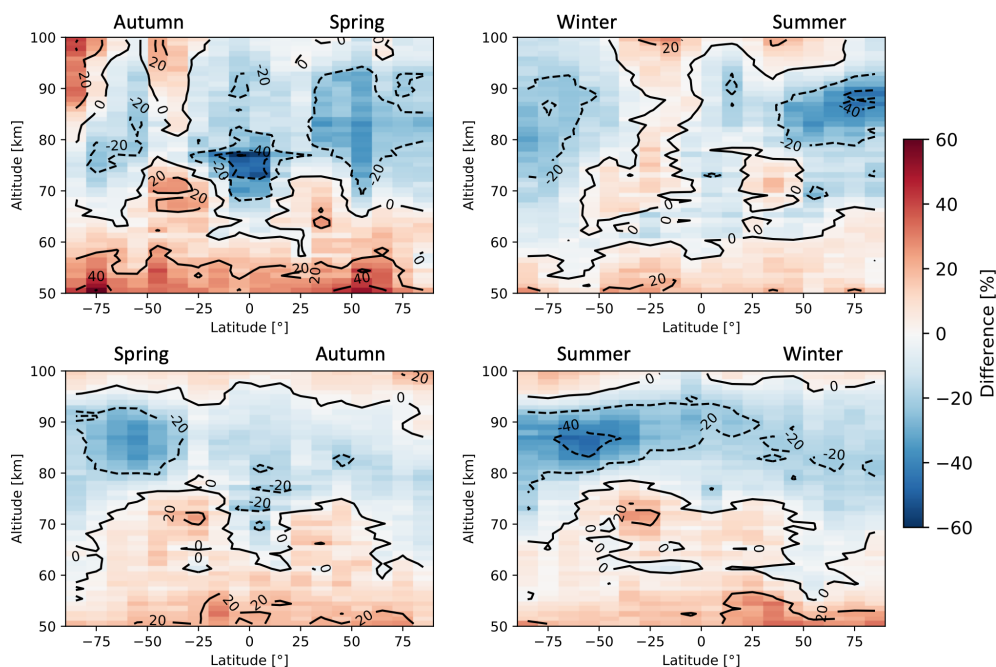


Figure A2. Seasonal zonal means of SMR–MIPAS middle atmosphere relative differences averaged over the time period indicated in Table 2. The seasons are intended as the time between the solstice and the equinox.

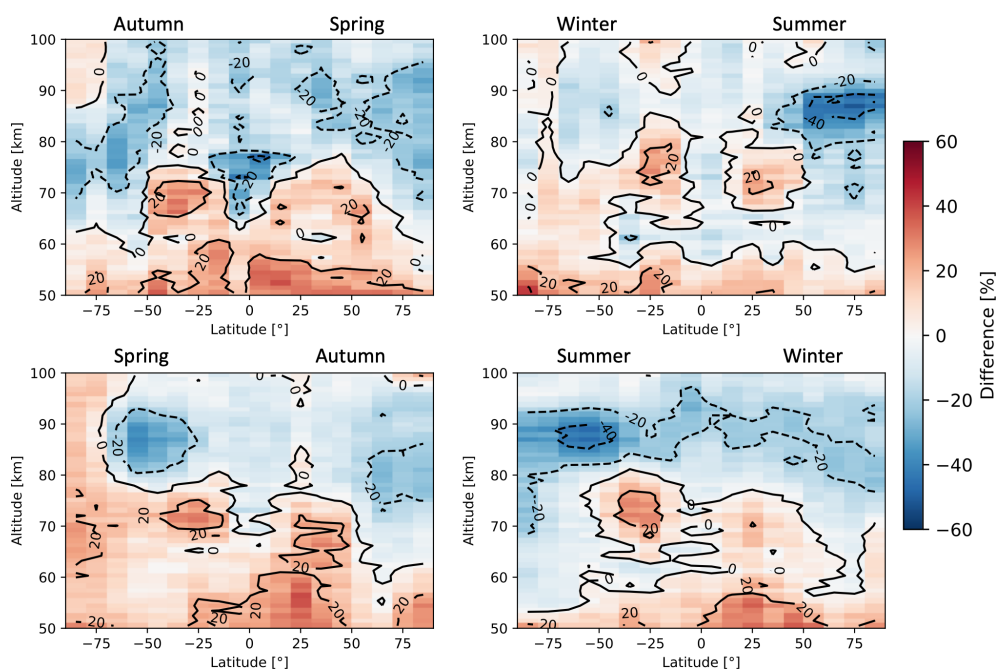


Figure A3. Seasonal zonal means of SMR–MIPAS upper atmosphere relative differences averaged over the time period indicated in Table 2. The seasons are intended as the time between the solstice and the equinox.

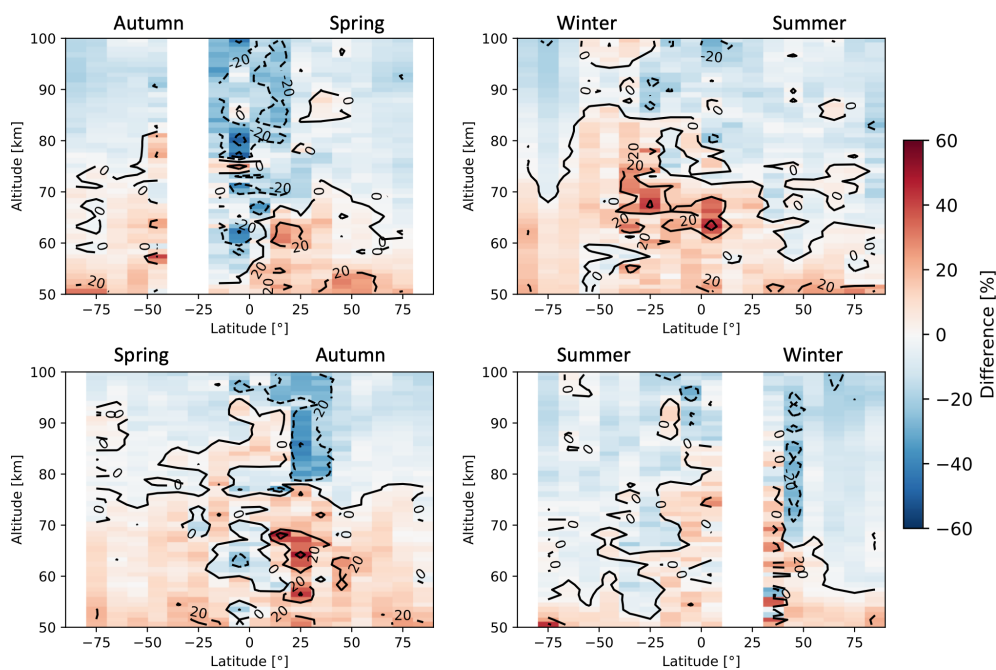


Figure A4. Seasonal zonal means of SMR–ACE relative differences averaged over the whole time between February 2004 and March 2019. The seasons are intended as the time between the solstice and the equinox.

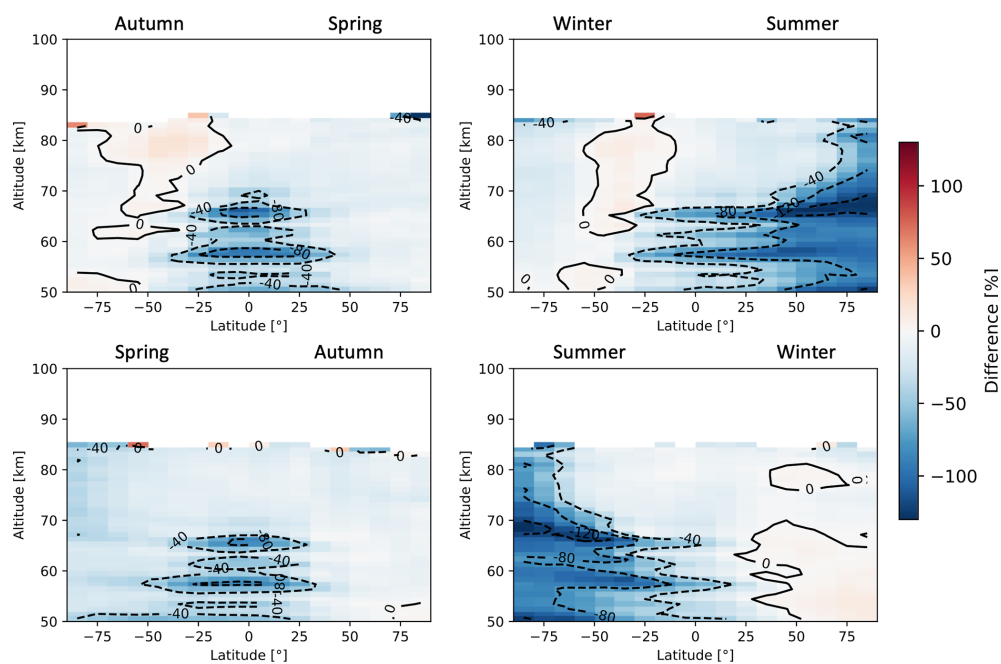


Figure A5. Seasonal zonal means of SMR–MLS relative differences averaged over the whole time between July 2004 and March 2019. The seasons are intended as the time between the solstice and the equinox. Note the different colour scale compared to the previous figures.

Data availability. Odin/SMR v3.0 L2 data are publicly accessible at <http://odin.rss.chalmers.se/level2> (last access: 8 September 2020; OdinSMR, 2020); MIPAS IMK/IAA L2 data (both NOM and MA/UA) can be downloaded upon registration at <http://www.imk-asf.kit.edu/english/308.php> (last access: 8 September 2020; KIT, 2020); ACE-FTS L2 data are available upon request at <https://database.scisat.ca/l2signup.php> (last access: 8 September 2020; ACE/SCISAT, 2020); MLS L2 data are available at <https://doi.org/10.5067/Aura/MLS/DATA2005> (Schwartz et al., 2015).

Author contributions. FG developed the correction algorithm, processed the CO data, made most of the plots and wrote most of the text. KP, DM and PE initiated the project and supported FG throughout it. KP contributed to the writing of the text. PF performed the comparison study between SMR and the OSO radiometer and wrote the corresponding section. BR helped with the processing of the data. All co-authors contributed to the interpretation of the results and proofread the text.

Competing interests. The authors declare that they have no conflict of interest.

Acknowledgements. The Chalmers team acknowledges support from the Swedish National Space Agency (grant no. Dnr 88/14 and 72/17). Odin is a Swedish-led satellite mission and is also part of the European Space Agency's (ESA) third-party mission programme. The reprocessing of the SMR data was supported by ESA (MesosphEO and Odin/SMR reprocessing projects). The authors would like to thank Julia Ringsby for her contribution to the correction algorithm. Bernd Funke acknowledges support by the Spanish MCINN (ESP2017-87143-R) and EC FEDER funds. The Atmospheric Chemistry Experiment is a Canadian-led mission mainly supported by the Canadian Space Agency. MLS research in Edinburgh was funded by NERC. The authors also thank the two anonymous reviewers for their helpful comments.

Financial support. This research has been supported by the Swedish National Space Agency (grant nos. Dnr 88/14 and Dnr 72/17) and the European Space Agency (Odin reprocessing, MesosphEO grant).

Review statement. This paper was edited by Helen Worden and reviewed by two anonymous referees.

References

- ACE/SCISAT: ACE/SCISAT Database, Level 2 Data Access, available at: <https://database.scisat.ca/l2signup.php>, last access: 8 September 2020.
- Allen, D. R., Stanford, J. L., López-Valverde, M. A., Nakamura, N., Lary, D. J., Douglass, A. R., Cerniglia, M. C., Remedios, J. J.,

- and Taylor, F. W.: Observations of Middle Atmosphere CO from the UARS ISAMS during the Early Northern Winter 1991/92, *J. Atmos. Sci.*, 56, 563–583, [https://doi.org/10.1175/1520-0469\(1999\)056<0563:OOMACF>2.0.CO;2](https://doi.org/10.1175/1520-0469(1999)056<0563:OOMACF>2.0.CO;2), 1999.
- Baron, Ph., Ricaud, Ph., de la Noë, J., Eriksson, J. E. P., Merino, F., Ridal, M., and Murtagh, D. P.: Studies for the Odin sub-millimetre radiometer. II. Retrieval methodologies, *Can. J. Phys.*, 80, 341–356, <https://doi.org/10.1139/p01-150>, 2002.
- Barret, B., Ricaud, P., Santee, M. L., Attié, J.-L., Urban, J., Le Flochmoën, E., Berthet, G., Murtagh, D., Eriksson, P., Jones, A., de La Noë, J., Dupuy, E., Froidevaux, L., Livesey, N. J., Waters, J. W., and Filipiak, M. J.: Inter-comparisons of trace gases profiles from the Odin/SMR and Aura/MLS limb sounders, *J. Geophys. Res.*, 111, D21302, <https://doi.org/10.1029/2006JD007305>, 2006.
- Bernath, P. F., McElroy, C. T., Abrams, M. C., Boone, C. D., Butler, M., Camy-Peyret, C., Carleer, M., Clerbaux, C., Coheur, P.-F., Colin, R., DeCola, P., DeMazière, M., Drummond, J. R., Dufour, D., Evans, W. F. J., Fast, H., Fussen, D., Gilbert, K., Jennings, D. E., Llewellyn, E. J., Lowe, R. P., Mahieu, E., McConnell, J. C., McHugh, M., McLeod, S. D., Michaud, R., Midwinter, C., Nassar, R., Nichitiu, F., Nowlan, C., Rinsland, C. P., Rochon, Y. J., Rowlands, N., Semeniuk, K., Simon, P., Skelton, R., Sloan, J. J., Soucy, M.-A., Strong, K., Tremblay, P., Turnbull, D., Walker, K. A., Walkty, I., Wardle, D. A., Wehrle, V., Zander, R., and Zou, J.: Atmospheric Chemistry Experiment (ACE): Mission overview, *Geophys. Res. Lett.*, 32, L15S01, <https://doi.org/10.1029/2005GL022386>, 2005.
- Boone, C. D., Nassar, R., Walker, K. A., Rochon, Y., McLeod, S. D., Rinsland, C. P., and Bernath, P. F.: Retrievals for the Atmospheric Chemistry Experiment Fourier-Transform Spectrometer, *Appl. Opt.*, 44, 7218–7231, <https://doi.org/10.1364/AO.44.007218>, 2005.
- Boone, C. D., Walker, K. A., and Bernath, P. F.: Version 3 Retrievals for the Atmospheric Chemistry Experiment Fourier Transform Spectrometer (ACE-FTS), *The Atmospheric Chemistry Experiment ACE at 10: A Solar Occultation Anthology*, pp. 103–127 A. Deepak Publishing, Hampton, Va., 2013.
- Brasseur, G. P. and Solomon, S.: *Aeronomy of the Middle Atmosphere*, Springer, The Netherlands, 3rd Edition, 2005.
- Buehler, S. A., Mendrok, J., Eriksson, P., Perrin, A., Larsson, R., and Lemke, O.: ARTS, the Atmospheric Radiative Transfer Simulator – version 2.2, the planetary toolbox edition, *Geosci. Model Dev.*, 11, 1537–1556, <https://doi.org/10.5194/gmd-11-1537-2018>, 2018.
- Charlton, A. J. and Polvani, L. M.: A New Look at Stratospheric Sudden Warmings. Part I: Climatology and Modeling Benchmarks, *J. Climate*, 20, 449–469, <https://doi.org/10.1175/JCLI3996.1>, 2007.
- Clancy, R. T., Muhleman, D. O., and Berge, G. L.: Microwave spectra of terrestrial mesospheric CO, *J. Geophys. Res.*, 87, 5009, <https://doi.org/10.1029/JC087iC07p05009>, 1982.
- Clerbaux, C., George, M., Turquety, S., Walker, K. A., Barret, B., Bernath, P., Boone, C., Borsdorff, T., Cammas, J. P., Catoire, V., Coffey, M., Coheur, P.-F., Deeter, M., De Mazière, M., Drummond, J., Duchatelet, P., Dupuy, E., de Zafra, R., Eddounia, F., Edwards, D. P., Emmons, L., Funke, B., Gille, J., Griffith, D. W. T., Hannigan, J., Hase, F., Höpfner, M., Jones, N., Kagawa, A., Kasai, Y., Kramer, I., Le Flochmoën, E., Livesey,

- N. J., López-Puertas, M., Luo, M., Mahieu, E., Murtagh, D., Nédélec, P., Pazmino, A., Pumphrey, H., Ricaud, P., Rinsland, C. P., Robert, C., Schneider, M., Senten, C., Stiller, G., Strandberg, A., Strong, K., Sussmann, R., Thouret, V., Urban, J., and Wiacek, A.: CO measurements from the ACE-FTS satellite instrument: data analysis and validation using ground-based, airborne and spaceborne observations, *Atmos. Chem. Phys.*, 8, 2569–2594, <https://doi.org/10.5194/acp-8-2569-2008>, 2008.
- Dee, D. P., Uppala, S. M., Simmons, A. J., Berrisford, P., Poli, P., Kobayashi, S., Andrae, U., Balmaseda, M. A., Balsamo, G., Bauer, P., Bechtold, P., Beljaars, A. C. M., van de Berg, L., Bidlot, J., Bormann, N., Delsol, C., Dragani, R., Fuentes, M., Geer, A. J., Haimberger, L., Healy, S. B., Hersbach, H., Hólm, E. V., Isaksen, I., Kållberg, P., Köhler, M., Matricardi, M., McNally, A. P., Monge-Sanz, B. M., Morcrette, J.-J., Park, B.-K., Peubey, C., de Rosnay, P., Tavolato, C., Thépaut, J.-N., and Vitart, F.: The ERA-Interim reanalysis: configuration and performance of the data assimilation system, *Q. J. Roy. Meteorol. Soc.*, 137, 553–597, <https://doi.org/10.1002/qj.828>, 2011.
- de Zafra, R. L. and Muscari, G.: CO as an important high-altitude tracer of dynamics in the polar stratosphere and mesosphere, *J. Geophys. Res.*, 109, D06105, <https://doi.org/10.1029/2004JD005102>, 2004.
- Dupuy, É., Urban, J., Ricaud, P., Le Flochmoën, É., Lautié, N., Murtagh, D., De La Noë, J., El Amraoui, L., Eriksson, P., Forkman, P., Frisk, U., Jégou, F., Jiménez, C., and Olberg, M.: Stratospheric measurements of carbon monoxide with the Odin Sub-Millimetre Radiometer: Retrieval and first results, *Geophys. Res. Lett.*, 31, L20101, <https://doi.org/10.1029/2004GL020558>, 2004.
- Eriksson, P., Jiménez, C., and Buehler, S. A.: Qpack, a general tool for instrument simulation and retrieval work, *J. Quant. Spectrosc. Ra.*, 91, 47–64, <https://doi.org/10.1016/j.jqsrt.2004.05.050>, 2005.
- Eriksson, P., Ekström, M., Melsheimer, C., and Buehler, S.: Efficient forward modelling by matrix representation of sensor responses, *Int. J. Remote Sens.*, 27, 1793–1808, <https://doi.org/10.1080/01431160500447254>, 2006.
- Eriksson, P., Buehler, S. A., Davis, C. P., Emde, C., and Lemke, O.: ARTS, the atmospheric radiative transfer simulator, Version 2, *J. Quant. Spectrosc. Ra.*, 112, 1551–1558, <https://doi.org/10.1016/j.jqsrt.2011.03.001>, 2011.
- Errera, Q., Chabrilat, S., Christophe, Y., Deboscher, J., Hubert, D., Lahoz, W., Santee, M. L., Shiotani, M., Skachko, S., von Clarmann, T., and Walker, K.: Technical note: Reanalysis of Aura MLS chemical observations, *Atmos. Chem. Phys.*, 19, 13647–13679, <https://doi.org/10.5194/acp-19-13647-2019>, 2019.
- Forkman, P., Christensen, O. M., Eriksson, P., Urban, J., and Funke, B.: Six years of mesospheric CO estimated from ground-based frequency-switched microwave radiometry at 57° N compared with satellite instruments, *Atmos. Meas. Tech.*, 5, 2827–2841, <https://doi.org/10.5194/amt-5-2827-2012>, 2012.
- Forkman, P., Christensen, O. M., Eriksson, P., Billade, B., Vassilev, V., and Shulga, V. M.: A compact receiver system for simultaneous measurements of mesospheric CO and O₃, *Geosci. Instrum. Method. Data Syst.*, 5, 27–44, <https://doi.org/10.5194/gi-5-27-2016>, 2016.
- Frisk, U., Hagström, M., Ala-Laurinaho, J., Andersson, S., Berges, J.-C., Chabaud, J.-P., Dahlgren, M., Emrich, A., Florén, H.-G., Florin, G., Fredrixon, M., Gaier, T., Haas, R., Hirvonen, T., Hjalmarsson, Å., Jakobsson, B., Jukkala, P., Kildal, P. S., Kollberg, E., Lassing, J., Lecacheux, A., Lehtikainen, P., Lehto, A., Mallet, J., Marty, C., Michet, D., Narbonne, J., Nexon, M., Olberg, M., Olofsson, A. O. H., Olofsson, G., Origné, A., Petersson, M., Piironen, P., Pons, R., Pouliquen, D., Ristorelli, I., Rosolen, C., Rouaix, G., Räisänen, A. V., Serra, G., Sjöberg, F., Stenmark, L., Torchinsky, S., Tuovinen, J., Ullberg, C., Vinterhav, E., Wade-falk, N., Zirath, H., Zimmermann, P., and Zimmermann, R.: The Odin satellite I. Radiometer design and test, *A&A*, 402, L27–L34, <https://doi.org/10.1051/0004-6361:20030335>, 2003.
- Froidevaux, L., Livesey, N. J., Read, W. G., Jiang, Y. B., Jimenez, C., Filipiak, M. J., Schwartz, M. J., Santee, M. L., Pumphrey, H. C., Jiang, J. H., Wu, D. L., Manney, G. L., Drouin, B. J., Waters, J. W., Fetzer, E. J., Bernath, P. F., Boone, C. D., Walker, K. A., Jucks, K. W., Toon, G. C., Margitan, J. J., Sen, B., Webster, C. R., Christensen, L. E., Elkins, J. W., Atlas, E., Lueb, R. A., and Hendershot, R.: Early validation analyses of atmospheric profiles from EOS MLS on the Aura Satellite, *IEEE Trans. Geosci. Rem. Sens.*, 44, 1106–1121, <https://doi.org/10.1109/TGRS.2006.864366>, 2006.
- Funke, B., López-Puertas, M., Bermejo-Pantaleón, D., von Clarmann, T., Stiller, G. P., Höpfner, M., Grabowski, U., and Kaufmann, M.: Analysis of nonlocal thermodynamic equilibrium CO 4.7 μ m fundamental, isotopic, and hot band emissions measured by the Michelson Interferometer for Passive Atmospheric Sounding on Envisat, *J. Geophys. Res.*, 112, D11305, <https://doi.org/10.1029/2006JD007933>, 2007.
- Funke, B., López-Puertas, M., García-Comas, M., Stiller, G. P., von Clarmann, T., Höpfner, M., Glatthor, N., Grabowski, U., Kellmann, S., and Linden, A.: Carbon monoxide distributions from the upper troposphere to the mesosphere inferred from 4.7 μ m non-local thermal equilibrium emissions measured by MIPAS on Envisat, *Atmos. Chem. Phys.*, 9, 2387–2411, <https://doi.org/10.5194/acp-9-2387-2009>, 2009.
- García, R. R., López-Puertas, M., Funke, B., Marsh, D. R., Kinnison, D. E., Smith, A. K., and González-Galindo, F.: On the distribution of CO₂ and CO in the mesosphere and lower thermosphere, *J. Geophys. Res.-Atmos.*, 119, 5700–5718, <https://doi.org/10.1002/2013JD021208>, 2014.
- García, R. R., López-Puertas, M., Funke, B., Kinnison, D. E., Marsh, D. R., and Qian, L.: On the secular trend of CO_x and CO₂ in the lower thermosphere, *J. Geophys. Res. Atmos.*, 121, 3634–3644, <https://doi.org/10.1002/2015JD024553>, 2016.
- Hamilton, K.: MIDDLE ATMOSPHERE|Semiannual Oscillation, *Encyclopedia of Atmospheric Sciences (Second Edition)*, Academic Press, pp. 26–29, <https://doi.org/10.1016/B978-0-12-382225-3.00233-4>, 2015.
- Karlsson, B., Gumbel, J., Stegman, J., Lautier, N., Murtagh, D., and Odin, Team: Studies of Noctilucent Clouds by the Odin Satellite, in: *Proceedings of the 35th COSPAR Scientific Assembly*, 35, 1921, 2004.
- Kiefer, M. and Lossow, S.: MIPAS-IMK/IAA L2 Data ReadMe, FMI-TN-MesosphEO-WP4-003, Version 1.0, 2017.
- KIT: Available Data, Karlsruhe Institute of Technology, available at: <http://www.imk-asf.kit.edu/english/308.php>, last access: 8 September 2020.
- Lee, J. N., Wu, D. L., Manney, G. L., Schwartz, M. J., Lambert, A., Livesey, N. J., Minschwaner, K. R., Pumphrey, H. C., and Read, W. G.: Aura Microwave Limb Sounder ob-

- servations of the polar middle atmosphere: Dynamics and transport of CO and H₂O, *J. Geophys. Res.*, 116, D05110, <https://doi.org/10.1029/2010JD014608>, 2011.
- Lee, J. N., Wu, D. L., Ruzmaikin, A., and Fontenla, J.: Solar cycle variations in mesospheric carbon monoxide, *J. Atmos. Solar-Terrest. Phys.*, 170, 21–34, <https://doi.org/10.1016/j.jastp.2018.02.001>, 2018.
- Livesey, N. J., Read, W. G., Wagner, P. A., Froidevaux, L., Lambert, A., Manney, G. L., Millán Valle, L. F., Pumphrey, H. C., Santee, M. L., Schwartz, M. J., Wang, S., Fuller, R. A., Jarnot, R. F., Knosp, B. W., Martinez, E., and Lay, R. R.: Earth Observing System (EOS) Aura Microwave Limb Sounder (MLS) Version 4.2x Level 2 data quality and description document, Tech. Rep. D-33509 Rev. D, JPL, 2018.
- Manney, G. L., Harwood, R. S., MacKenzie, I. A., Minschwaner, K., Allen, D. R., Santee, M. L., Walker, K. A., Hegglin, M. I., Lambert, A., Pumphrey, H. C., Bernath, P. F., Boone, C. D., Schwartz, M. J., Livesey, N. J., Daffer, W. H., and Fuller, R. A.: Satellite observations and modeling of transport in the upper troposphere through the lower mesosphere during the 2006 major stratospheric sudden warming, *Atmos. Chem. Phys.*, 9, 4775–4795, <https://doi.org/10.5194/acp-9-4775-2009>, 2009.
- Minschwaner, K., Manney, G. L., Livesey, N. J., Pumphrey, H. C., Pickett, H. M., Froidevaux, L., Lambert, A., Schwartz, M. J., Bernath, P. F., Walker, K. A., and Boone, C. D.: The photochemistry of carbon monoxide in the stratosphere and mesosphere evaluated from observations by the Microwave Limb Sounder on the Aura satellite, *J. Geophys. Res.*, 115, D13303, <https://doi.org/10.1029/2009JD012654>, 2010.
- OdinSMR: Level2 data dashboard, available at: <http://odin.rss.chalmers.se/level2>, last access: 8 September 2020.
- Oelhaf, H.: MIPAS Mission Plan, Issue 4, Version 3, ESA Technical Note ENVI-SPPA-EOPG-TN-07-0073, 2008.
- Orsolini, Y. J., Limpasuvan, V., Pérot, K., Espy, P., Hibbins, R., Lossow, S., Raaholt Larsson, K., and Murtagh, D.: Modelling the descent of nitric oxide during the elevated stratopause event of January 2013, *J. Atmos. Solar-Terrest. Phys.*, 155, 50–61, <https://doi.org/10.1016/j.jastp.2017.01.006>, 2017.
- Pérot, K., Urban, J., and Murtagh, D. P.: Unusually strong nitric oxide descent in the Arctic middle atmosphere in early 2013 as observed by Odin/SMR, *Atmos. Chem. Phys.*, 14, 8009–8015, <https://doi.org/10.5194/acp-14-8009-2014>, 2014.
- Picone, J. M., Hedin, A. E., Drob, D. P., and Aikin, A. C.: NRLMSISE-00 empirical model of the atmosphere: Statistical comparisons and scientific issues, *J. Geophys. Res.*, 107, 1468, <https://doi.org/10.1029/2002JA009430>, 2002.
- Pumphrey, H. C., Filipiak, M. J., Livesey, N. J., Schwartz, M. J., Boone, C., Walker, K. A., Bernath, P., Ricaud, P., Barret, B., Clerbaux, C., Jarnot, R. F., Manney, G. L., and Waters, J. W.: Validation of middle-atmosphere carbon monoxide retrievals from the Microwave Limb Sounder on Aura, *J. Geophys. Res.*, 112, D24S38, <https://doi.org/10.1029/2007JD008723>, 2007.
- Randall, C. E., Rusch, D. W., Bevilacqua, R. M., Hoppel, K. W., Lumpe, J. D., Shettle, E., Thompson, E., Deaver, L., Zawodny, J., Kyrö, E., Johnson, B., Kelder, H., Dorokhov, V. M., König-Langlo, G., and Gil, M.: Validation of POAM III ozone: comparison with ozonesonde and satellite data, *J. Geophys. Res.*, 108, 4367, <https://doi.org/10.1029/2002JD002944>, 2003.
- Rodgers, C. D.: Inverse methods for atmospheric sounding: Theory and practise, World Scientific Publishing, 1st Edition, 2000.
- Rothman, L. S., Gordon, I. E., Babikov, Y., Barbe, A., Chris Benner, D., Bernath, P. F., Birk, M., Bizzocchi, L., Boudon, V., Brown, L. R., Campargue, A., Chance, K., Cohen, E. A., Coudert, L. H., Devi, V. M., Drouin, B. J., Fayt, A., Flaud, J.-M., Gamache, R. R., Harrison, J. J., Hartmann, J.-M., Hill, C., Hodges, J. T., Jacquemart, D., Jolly, A., Lamouroux, J., Le Roy, R. J., Li, G., Long, D. A., Lyulin, O. M., Mackie, C. J., Massie, S. T., Mikhailenko, S., Müller, H. S. P., Naumenko, O. V., Nikitin, A. V., Orphal, J., Perevalov, V., Perrin, A., Polovtseva, E. R., Richard, C., Smith, M. A. H., Starikova, E., Sung, K., Tashkun, S., Tennyson, J., Toon, G. C., Tyuterev, V. I., and Wagner, G.: The HITRAN2012 molecular spectroscopic database, *J. Quant. Spectrosc. Ra.*, 130, 4–50, <https://doi.org/10.1016/j.jqsrt.2013.07.002>, 2013.
- Rydberg, B., Eriksson, P., Kiviranta, J., Ringsby, J., Skyman, A., and Murtagh, D.: Odin/SMR Algorithm Theoretical Basis Document: Level 1 Processing, Technical Report, Chalmers University of Technology, Department of Space, Earth and Environment, available at: <http://odin.rss.chalmers.se/#documents> (last access: 8 September 2020), 2017.
- Schoeberl, M. R., Douglass, A. R., Hilsenrath, E., Bhartia, P. K., Beer, R., Waters, J. W., Gunson, M. R., Froidevaux, L., Gille, J. C., Barnett, J. J., Levelt, P. F., and DeCola, P.: Overview of the EOS Aura Mission, *IEEE Trans. Geosci. Remote Sensing*, 44, 1066–1074, <https://doi.org/10.1109/TGRS.2005.861950>, 2006.
- Schwartz, M., Pumphrey, H., Livesey, N., and Read, W.: MLS/Aura Level 2 Carbon Monoxide (CO) Mixing Ratio V004, Green-belt, MD, USA, Goddard Earth Sciences Data and Information Services Center (GES DISC), <https://doi.org/10.5067/Aura/MLS/DATA2005>, 2015.
- Sheese, P. E., Boone, C. D., and Walker, K. A.: Detecting physically unrealistic outliers in ACE-FTS atmospheric measurements, *Atmos. Meas. Tech.*, 8, 741–750, <https://doi.org/10.5194/amt-8-741-2015>, 2015.
- Sheese, P. E., Walker, K. A., Boone, C. D., Bernath, P. F., Froidevaux, L., Funke, B., Raspollini, P., and von Clarman, T.: ACE-FTS ozone, water vapour, nitrous oxide, nitric acid, and carbon monoxide profile intercomparisons with MIPAS and MLS, *J. Quant. Spectrosc. Ra.*, 186, 63–80, <https://doi.org/10.1016/j.jqsrt.2016.06.026>, 2016.
- Solomon, S., Garcia, R. R., Olivero, J. J., Bevilacqua, R. M., Schwartz, P. R., Clancy, R. T., and Muhleman, D. O.: Photochemistry and Transport of Carbon Monoxide in the Middle Atmosphere, *J. Atmos. Sci.*, 42, 10721083, [https://doi.org/10.1175/1520-0469\(1985\)042<1072:PATOCM>2.0.CO;2](https://doi.org/10.1175/1520-0469(1985)042<1072:PATOCM>2.0.CO;2), 1985.
- Vignon, E. and Mitchell, D. M.: The stratopause evolution during different types of sudden stratospheric warming event, *Clim. Dynam.*, 44, 3323, <https://doi.org/10.1007/s00382-014-2292-4>, 2015.
- Waters, J. W., Froidevaux, L., Jarnot, R. F., Read, W. G., Pickett, H. M., Harwood, R. S., Cofield, R. E., Filipiak, M. J., Flower, D. A., Livesey, N. J., Manney, G. L., Pumphrey, H. C., Santee, M. L., Siegel, P. H., and Wu, D. L.: An Overview of the EOS MLS Experiment, version 2.0, JPL D-15745, ATBD-MLS-01, 2004.

Zander R., Leclercq H., and Kaplan L.D.: Concentration of carbon monoxide in the upper stratosphere, *Geophys. Res. Lett.*, 8, 365–368, <https://doi.org/10.1029/GL008i004p00365>, 1981.

Paper 2

Improvement of Odin/SMR water vapour measurements and validation of the obtained dataset

Francesco Grieco, Kristell Pérot, Donal Murtagh, Patrick Eriksson, Bengt Rydberg, Bernd Funke, and Kaley A. Walker

Manuscript in preparation.

Improvement of Odin/SMR water vapour measurements and validation of the obtained dataset

Francesco Grieco¹, Kristell Pérot¹, Donal Murtagh¹, Patrick Eriksson¹, Bengt Rydberg², Bernd Funke³, and Kaley A. Walker⁴

¹Department of Space, Earth and Environment, Chalmers University of Technology, Gothenburg, 412 96, Sweden

²Molflow, Gråbo, 443 40, Sweden

³Instituto de Astrofísica de Andalucía, CSIC, Granada, Spain

⁴Department of Physics, University of Toronto, Toronto, M5S 1A7, ON, Canada

Correspondence: Francesco Grieco (francesco.grieco@chalmers.se)

Abstract.

Its long photochemical lifetime make H₂O a good tracer of mesospheric dynamics. In this study we present the reprocessing of 18 years of H₂O measurements from the Sub-Millimetre Radiometer (SMR) on board Odin satellite, constituting part of the SMR version 3.0 level 2 data. The previous version of the dataset showed poor accordance with measurements from other instruments, which suggested that the retrieved concentrations and temperature were subject to instrumental artifacts. Different hypothesis have been explored, and the idea of having underestimated the single sideband leakage turned out to be the most reasonable one. Therefore the value of the lowest transmission achievable have been raised to account for greater sideband leakage, and new retrievals have been performed with the new settings. The retrieved profiles extend between 40 - 100 km altitude and cover all latitudes to reach polar regions. A new validation study has been produced revealing an overall better accordance with the compared instruments, with respect to the older version. In particular, relative differences in H₂O concentration are always in the -40% - +20% range between 40 - 80 km and diverge at higher altitudes.

1 Introduction

With a lifetime of the order of months at the stratopause and of a few days at 100 km, H₂O is an important tracer of mesospheric circulation. It is also a main source of hydrogen radicals (such as OH, H, HO₂) which are responsible of destroying ozone in the middle atmosphere (Brasseur and Solomon, 2005). A source of H₂O in the mesosphere is methane oxidation:



which, mostly important in the stratosphere, declines with altitude due to smaller abundances of methane and stops between 60 - 70 km. Above that, another source is oxidation of molecular hydrogen through two reactions:



The only major sink of H_2O in the mesosphere is photodissociation:



which becomes more important with altitude and dominates above 70 km, also due to lack of a major source, resulting in a decrease of H_2O concentration with increasing altitude. Moreover, solely at high latitudes and during local winter, another sink consists in the freezing of water and removal by sedimentation; while high latitudes summers are characterised by a convective uplift of ice particles that reach the stratosphere and evaporate, increasing local H_2O concentration (Lossow et al., 2019).

Satellite observations of H_2O in the middle atmosphere have been performed since 1970s with the launch of Nimbus-7 satellite and the activity of two instruments on board: LIMS (Limb Infrared Monitor of the Stratosphere) (Remsberg et al., 1984) and SAMS (Stratospheric and Mesospheric Sounder) (Munro and Rodgers, 1994). Various instruments have followed through the years, the most recent ones being SABER (Sounding of the Atmosphere using Broadband Emission Radiometry) (Feofilov et al., 2009) launched on board TIMED (Thermosphere-Ionosphere-Mesosphere Energetics and Dynamics) in 2001, ACE-FTS (Atmospheric Chemistry Experiment - Fourier Transform Spectrometer) (Nassar et al., 2005) and MAESTRO (Measurement of Aerosol Extinction in the Stratosphere and Troposphere Retrieved by Occultation) (Sioris et al., 2010) launched on board Scisat-1 in 2003, and MLS (Microwave Limb Sounder) (Waters et al., 2006) launched on board the Aura satellite in 2004. All of these instruments are still operating. Moreover, in 2002 three satellites performing middle atmospheric H_2O observations were launched on board the Envisat satellite: GOMOS (Global Ozone Monitoring by Occultation of Stars) (Montoux et al., 2009), MIPAS (Michelson Interferometer for Passive Atmospheric Sounding (e.g., Wetzel et al., 2013) and SCIAMACHY (Scanning Imaging Absorption Spectrometer for Atmospheric Cartography) (e.g., Weigel et al., 2016). Their activity stopped in April 2012 due to loss of contact with the satellite.

The Sub-Millimetre Radiometer (SMR) on board the Odin satellite has been performing H_2O measurements in the middle atmosphere since its launch in 2001 and is still operating. Previous studies relative to SMR H_2O observations have been carried out by Lossow et al. (2007, 2008, 2009) and Urban et al. (2007). These studies refer to SMR v2 L2 data which, in the mesosphere, present high biases compared to other instruments, i.e. around -20% between 40 - 70 km and greater than -50% between 70 - 100 km (Lossow et al., 2019; Murtagh et al., 2018). The Odin/SMR data set has undergone a full reprocessing, leading to a new version (v3.0). The present study, carried out to identify the instrumental origins of the above-mentioned biases, is part of this extensive reprocessing work and led to the conclusion that an underestimation of the sideband leakage was originating the biases (see Section 2). A new value of the sideband leakage has been found and new retrievals have been performed. The resulting dataset, which is part of SMR v3.0 L2 data, is presented in Section 3 and validated in Section 4 by comparing it with satellite measurements from MIPAS, ACE-FTS and MLS.

2 Odin/SMR H₂O measurements

2.1 The sub-mm radiometer

The Sub-Millimeter Radiometer (SMR) is an instrument on board the Odin satellite performing limb sounding of the middle atmosphere. The measurements cover the whole globe including the polar regions. Odin was launched on 20 February 2001 as a Swedish-led project in collaboration with Canada, France and Finland. Its 600 km sun-synchronous orbit has an inclination of 97.77° and a 18:00 hrs ascending node. SMR has four sub-millimeter receivers covering frequencies between 486 - 504 GHz and 541 - 581 GHz and a millimeter receiver measuring radiation around 118 GHz, so that emissions from O₃, H₂O, CO, NO, ClO, N₂O, HNO₃ and O₂ due to rotational transitions can be detected (Frisk et al., 2003). SMR components are schematised in Figure 1. A Dicke switch allows to rapidly change the source of input radiation between the main beam and calibrators (cold sky and hot load); the radiation is then split according to polarisation and collected by different receivers where it is combined with a local oscillator (LO) signal by means of a mixer, converting the signal to lower frequencies (3.3 - 4.5 GHz) and maintaining only the contribution from two sidebands. Since SMR is a single sideband instrument, the resulting spectra would be given by the sum of the two sidebands: the primary band, including the signal of scientific interest, and the image band; however, the signal also propagates in a Martin-Puplett interferometer whose arms length is tuned so to maximize suppression of the image band and optimize transmission of the primary band. The response of the interferometer with regards to frequency ν is equal to:

$$r = r_0 + \frac{(1 - 2r_0)}{2} \left[1 + \cos \left(\frac{4\pi l\nu}{c} \right) \right], \quad (5)$$

where l is the interferometer length, and r_0 is the lowest transmission value achieved (Eriksson and Urban, 2006) which is not zero because it is not possible to achieve perfect suppression. The linear dependency of l with respect to the temperature on board the satellite is also taken into account:

$$l(T) = l_0 + \frac{l_{sb}}{2} + c_T(T - T_0) \quad (6)$$

where T is the temperature of the satellite, l_0 is the interferometer length at the reference temperature T_0 , l_{sb} the nominal sideband path tuning length (expressed for both arms altogether, hence the division by 2), and c_T is the coefficient of thermal expansion. l_0 , T_0 and c_T values have been estimated by Eriksson and Urban (2006) from fits based on various observations. Since it is impossible to completely suppress the image band contribution, a sideband leakage (p) is included in the measurement, where p is defined as:

$$p(\nu) = \frac{r(\nu')}{r(\nu) + r(\nu')} \quad (7)$$

with ν and ν' being, respectively, the primary band and image band center frequencies. Eventually, the signal is amplified and directed to the spectrometers.

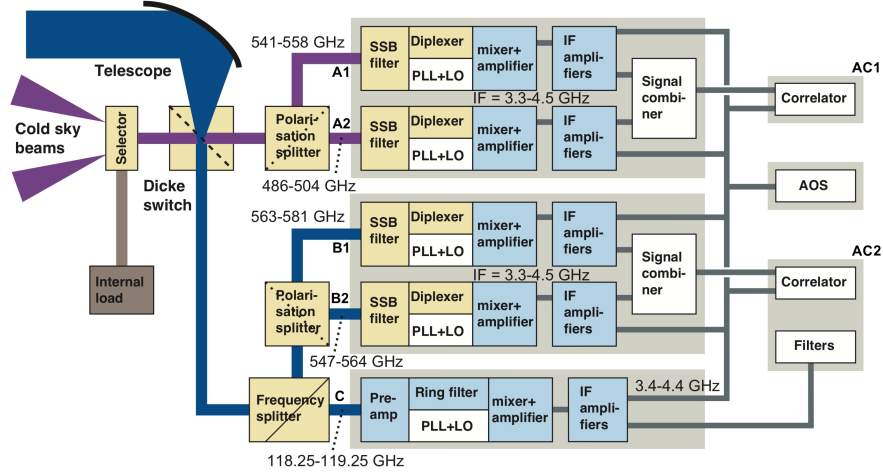


Figure 1. Block diagram of the Odin radiometer. From Frisk et al. (2003).

The observation time of the instrument has been equally shared between astronomical and atmospheric observations until 2007. After that, the astronomical mission was concluded and the instrument has been exclusively employed to perform atmospheric measurements. SMR measures spectra during upward and downward vertical scanning, with single tangent altitudes ranging between 7 - 72 km (stratospheric scans), 7 - 110 km (strato-mesospheric scans) or 60 - 110 km (mesospheric scans).

5 2.2 SMR H₂O measurements: description and recovery

SMR receivers can be set up to cover different frequency bands. To each of these configurations, called frequency modes (FM), are assigned scheduled observation times. In this study we focus on mesospheric observations of H₂O emissions from rotational transitions. They are performed with a 3 - 4 km vertical resolution, using FMs 13 and 19 (while stratospheric observations are performed using other FMs) whose characteristics are summarised in Table 1. Also O₃ emissions are observed in the frequency bands covered by these two FMs, therefore O₃ concentration, as well as temperature, are retrieved simultaneously. The two FMs use different frontends, that is the set of components denoted by B2 and A1 in Figure 1. The retrievals were carried out using the Atmospheric Radiative Transfer Simulator (ARTS) which is a software package for long wavelength radiative transfer simulations, with a focus on passive microwave observations, incorporating effects of sensor characteristic (e.g. Eriksson et al., 2011). ARTS retrieval algorithms are based on the Optimal Estimation Method (e.g. Rodgers, 2000). In this study, a mesospheric inversion mode was used, performing retrievals from measurements with tangent altitudes between 40 and 100 km.

In the previous data version, H₂O, O₃ profiles retrieved from FMs 13 and 19 showed big differences from measurements of other satellites, presenting a bias in H₂O concentration around -20% between 40 - 70 km and greater than -50% between 70 - 100 km, as well as a O₃ concentration bias of -20% at 45 km increasing to less than -45% at 70 km and then steeply

Table 1. FMs for observing H₂O. From Rydberg et al. (2017).

Spectrometer	Frontend	LO Freq. [GHz]	Freq. Range [GHz]	Species	FM
AC1	555 B2	553.298	556.598 - 557.398	H ₂ ¹⁶ O, O ₃	13
	549 A1	553.050	556.550 - 557.350	H ₂ O, O ₃	19

going to high positive values (more than +45%) between 80 - 90 km. Temperature biases were also observed: in particular, for FM 19, the bias was equal to -5 K at 45 km and gradually increasing to -20 K at 100 km; while, for FM 13, the bias was equal to -20 K at 45 km and increasing to values lower than -45 K at high altitudes (Murtagh et al., 2018). This suggested the presence of instrumental artifacts. We investigated for possible non linearity in the spectra and for erroneous estimations of the pointing offset of the instrument, however an underestimation of r_0 turned out to be the most likely cause of the retrieved incongruous quantities. Sideband leakages greater than the nominal value have been already observed in spectra in Eriksson and Urban (2006). A r_0 of -14 dB had previously been assumed for both frontends used in the two FMs under consideration: an underestimation that caused spurious signal originated from the sideband leakage to be considered as part of the signal of interest, leading to misestimation of retrieved concentration and temperature. Setting the r_0 value to -13 dB for FM 13 and to -11 dB for FM 19 gave the best results in terms of minimizing differences from other instruments measurements (see Section 4).

H₂O retrieval for an exemplary scan is shown in Figure 2. Together with H₂O, also O₃ and Temperature are retrieved (not shown). A measure of how much a retrieved quantity is contaminated by the a priori is given by the measurement response, a quantity defined as the sum over the row of the averaging kernel matrix (Rodgers, 2000). Data with a measurement response lower than 0.75 are discarded. This is the case for the retrieved profile above 100 km which is, nevertheless, shown here out of completeness as well as high altitudes averaging kernels.

3 The new dataset

In this section we present the new H₂O products retrieved from FMs 13 and 19 measurements, which are part of the SMR v3.0 L2 dataset. In particular we describe H₂O concentration time series and compare H₂O profiles to the older v2.1 dataset, as well as the profiles from the other retrieval products from these FMs, i.e. O₃ and Temperature.

In Figure 3 it is shown a histogram summarising the number of L1 and L2 products available for FM13 and FM19 during the whole Odin operational time period. While from 2006 the two FMs have been used in the same proportion for H₂O measurements, in the early years of Odin FM13 has been used only occasionally, with a particularly high number of measurements performed during July 2002, July 2003 and August 2004. These are associated to a special scheduling set to study dynamics in the northern summer mesosphere related to the presence of noctilucent clouds (Karlsson et al., 2004).

Figures 4 and 5 show time series of H₂O volume mixing ratios corresponding to FM13 and FM19, respectively, in form of monthly zonal means over 5 latitude bands covering the whole globe. The gaps in the data set observed globally every northern

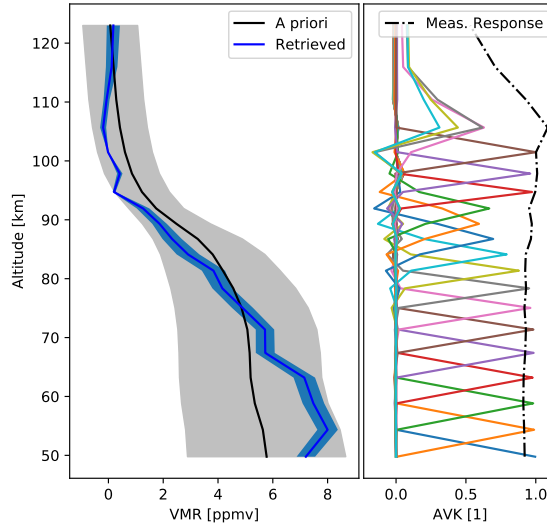


Figure 2. Example retrieval referring to ScanID 7286190262 from FM 19. Left: Retrieved concentration profile and error (in blue) and a priori including uncertainties (in grey). Right: Averaging kernels plotted in a different colour for each altitude (not indicated) and measurement response.

summer from 2013 are due to the fact that the instrument is put in stand by mode during the eclipse season, in order to save the batteries. At the tropics it is clear, from 80 km above, the presence of a Semi-Annual Oscillation (SAO) with maxima and minima in correspondence of solstices and equinoxes, respectively. This phenomenon is caused by SAO of the zonal winds in the mesosphere which is driven by momentum deposition from gravity and Kelvin waves coming from lower altitudes. Zonal winds SAO in turn give rise to SAO in meridional and vertical advection (Hamilton, 2015). In particular, in correspondence of equinoxes, a sinking or weak rising motion of air at the tropics causes the presence of lower H_2O concentrations in the mesosphere; while stronger rising motion, occurring during solstices, cause higher H_2O concentrations (e.g., Lossow et al., 2017). High latitudes are instead characterised by an annual cycle that features, at all altitudes and for both hemispheres: higher concentrations during local summertime, coming from dehydration of the polar regions and methane oxidation due to the greater amount of received sun radiation, and lower concentrations during local wintertime, due to the descent of dry air from the upper mesosphere via the downward branch of the mesospheric residual circulation. The amplitude of this oscillation is bigger in the southern hemisphere, where the descent of air is stronger and more stable (Schoeberl and Newman, 2015). Secondary maxima or plateaus can also be observed during local wintertime, as a consequence of two different processes in the two hemispheres. In the northern hemisphere they are due to Sudden Stratospheric Warmings (SSW) during which planetary waves disturb the polar vortex (e.g., Charlton and Polvani, 2007), causing moister air to be transported from lower altitudes and latitudes. Following some of the SSW events, during late winter, tongues of dry air which correspond to enhanced downward

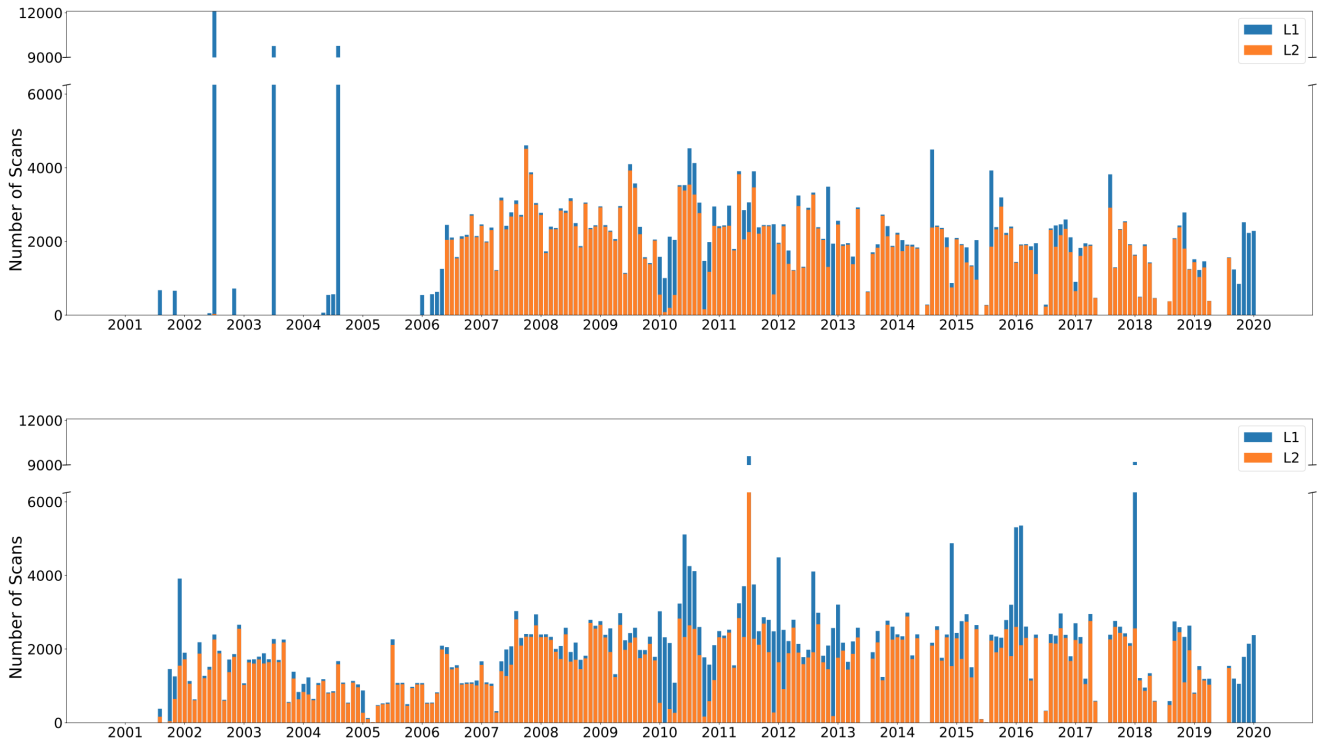


Figure 3. Number of L1 and L2 scans by month for FM13 (top) and FM19 (bottom). The ticks on the x-axis correspond to January 1st for each year.

motion can be observed. In fact, as the polar vortex recovers, the stratopause is reformed sometimes at higher altitudes than normal (Vignon and Mitchell, 2015; Pérot et al., 2014) from which dry air is transported downward. Regarding the southern hemisphere, the cause is to be attributed to pole-to-pole mesospheric circulation but the details of how this occurs are still under investigation (Lossow et al., 2017). Mid latitudes show, in a less pronounced way, both effects of SAO and annual cycle.

- 5 Finally, at all latitudes, higher H_2O concentrations can be observed during the period 2012-2016 which are related to a stronger solar activity.

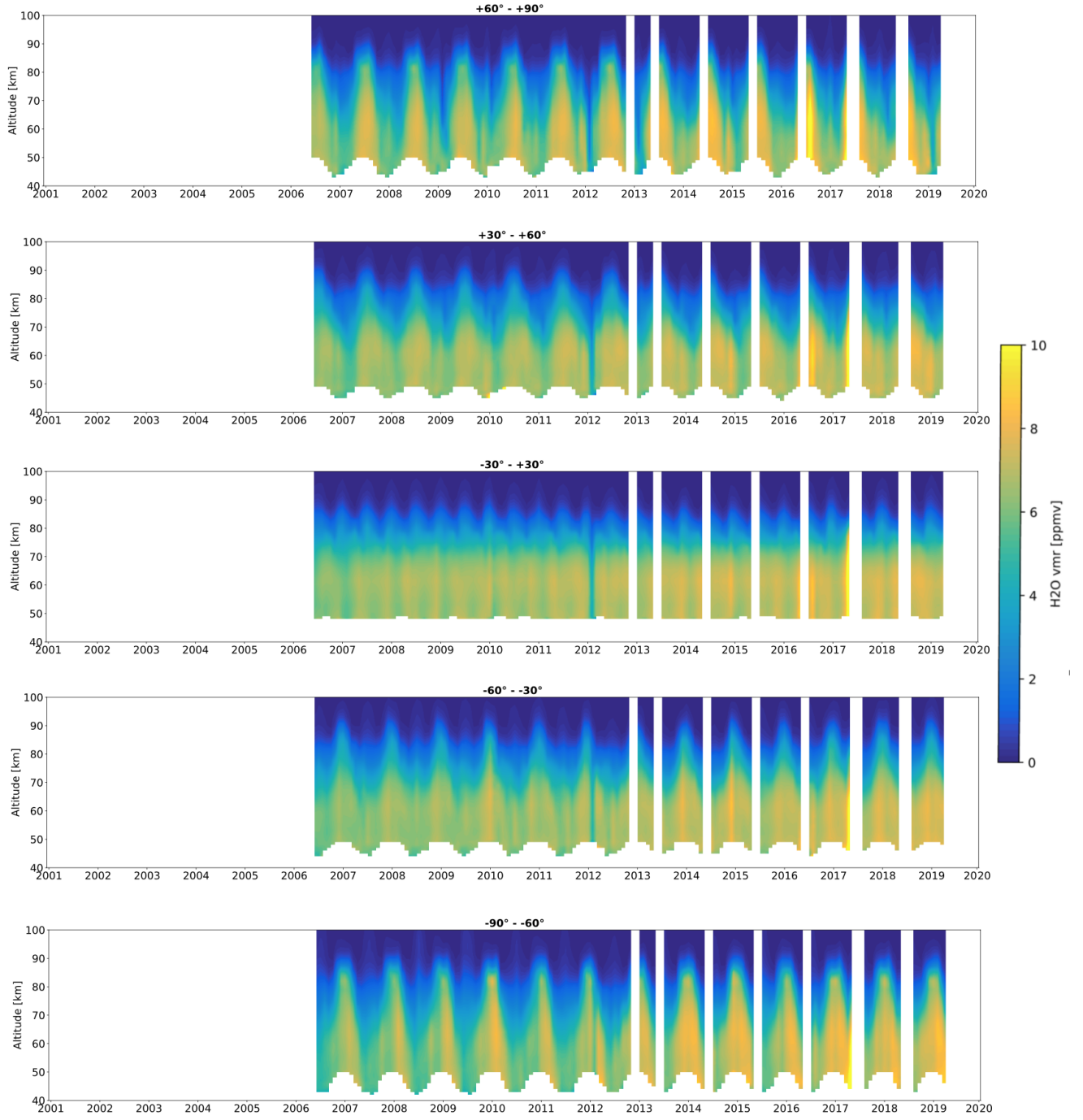


Figure 4. Time series of FM13 H₂O volume mixing ratios measured by SMR for different latitude bands. The white bands indicate periods during which the number of scans in the given latitude band is lower than 10. The ticks on the x-axis correspond to the beginning of each year.

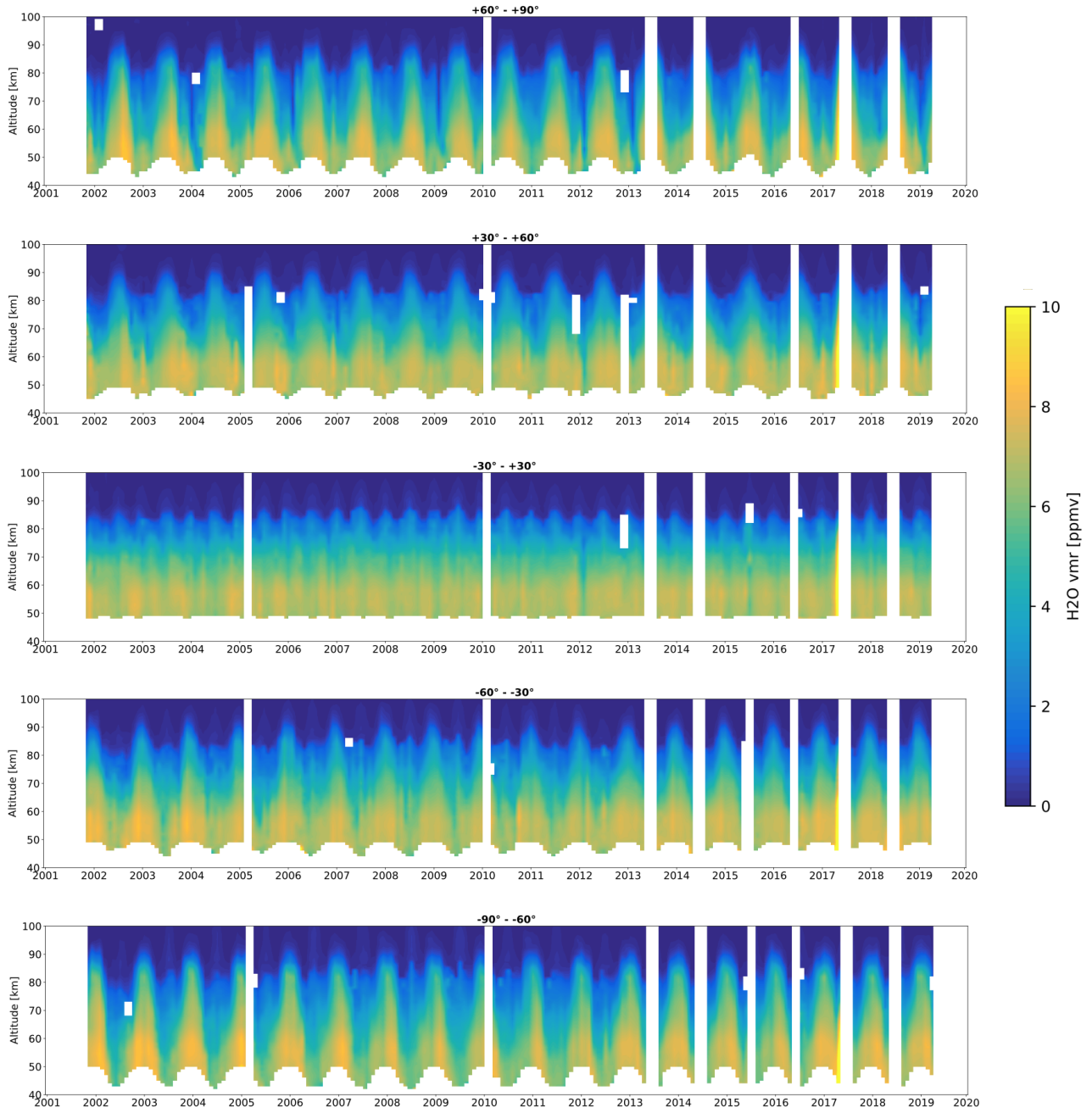


Figure 5. Time series of FM19 H₂O volume mixing ratios measured by SMR for different latitude bands. The white bands indicate periods during which the number of scans in the given latitude band is lower than 10. The ticks on the x-axis correspond to the beginning of each year.

Comparison with the older SMR v2.1 H₂O dataset (e.g., Urban et al., 2007) shows, for FM13, a relative difference of -25% around 40 km which goes down to reach 0% at 65 km. The value stays around 0% until 80 km and then increases up to +20% at 90 km, to finally decrease to -7% at 100 km (Figure 6a). Zonal mean plots of difference values averaged over the whole SMR operating time period, for different latitudes and seasons, are shown in the Appendix. Peaks of +30% are registered during northern spring and summer, as well as during southern summer and during local autumn in both hemispheres, at high latitudes between 80 - 100 km. Moreover, the highest negative values, of -60%, are observed during local autumn in both hemispheres, in an area within the tropics and the autumn pole between 90 - 100 km (Figure A1). Comparison of FM19 H₂O retrievals shows instead a relative difference of 0% between 40 - 45 km and of +10% between 50 - 60 km. Then the difference goes down to -15% at 80 km, back up to -5% between 85 - 90 km and then down again to -30% at 100 km (Figure 6b). Peaks of -40% are observed during northern spring and summer at high latitudes around 100 km altitude (Figure A2). O₃ and Temperature profile comparisons, and the zonal means showing differences for the various latitude and seasons, are described below and shown in the Appendix. FM13 O₃ v3.0–v2.1 profile comparison reveals a relative difference of +15% at 45 km which steeply approaches 0% and stays constant with altitude up until 60 km altitude. The difference then increases to +45% at 70 km, goes down to -15% between 70 - 75 km, then back up to +15% at 80 km. Above 80 km the relative difference reaches very negative values, with a peak of -160% at 85 km (out of shown scale) (Figure A3a). Regarding FM19, O₃ v3.0 profile shows, in comparison to v2.1, a relative difference of 0% at 40 km which slowly increases with altitude to reach +30% at 75 km. The value then increases rapidly to reach +80% at 80 km, it goes back down to 0% at 85 km and then up to +200% at 90 km (Figure A3b). The retrieved Temperature for FM13 is generally lower for v3 compared to v2, with the only exception of higher altitudes: we observe an absolute difference oscillating between -2.5 and -5 K in the 40 - 90 km altitude range, while between 90 - 100 km the value increases to reach + 5 K (Figure A6a). FM19 v3 Temperature is instead generally higher than measured in v2, with the absolute difference being equal to +7 K at 40 km, then oscillating between +2.5 and +5 K in the 45 - 90 km altitude range, and finally oscillating between 0 K and +6 K above 90 km (Figure A6b).

4 Comparison with other instruments

To evaluate the quality of the new FM13 and FM19 data, in this section we compare the SMR v3.0 H₂O retrievals from these FMs with coincident measurements from other limb-sounding satellite-borne instruments, that is MIPAS, ACE-FTS and MLS. Moreover, we also look at how the other two retrieved products, O₃ and temperature, compare to the other instruments.

Regarding H₂O, measurements are considered coincident if they occur within a maximum temporal separation of 9 hours and maximum spatial separation of 800 km, while for O₃ the criteria are 5 hours and 400 km, and for temperature 4 hours and 1000 km. Moreover, O₃ comparisons are carried out considering daytime and nighttime observations separately, due to the high variability of ozone between day and night. While ACE-FTS and MLS profiles have similar vertical resolutions to SMR, MIPAS profiles are characterised by more coarse resolutions. To verify if this needs to be taken into account when performing SMR–MIPAS comparisons, we carried out tests by smoothing SMR profiles with a Gaussian filter characterised by a FWHM equal to MIPAS vertical resolution. The smoothed SMR profiles resulted almost unaltered with respect to the original ones

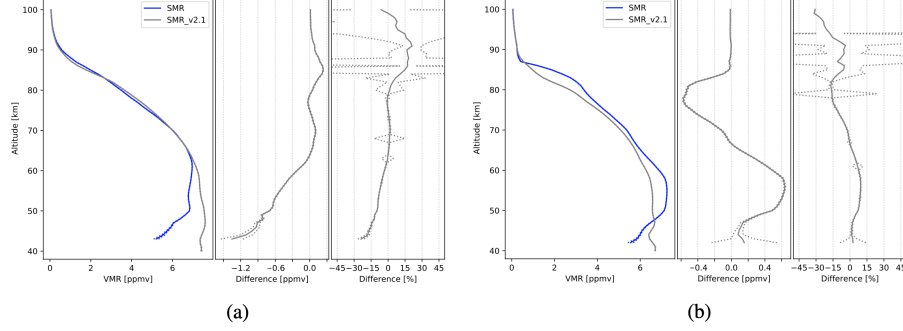


Figure 6. Comparison between SMR v3.0 and v2.1 H₂O concentrations, from FM13 (a) and FM19 (b). The data plotted are global averages over the whole time period between February 2001 and April 2019. Each subfigure consists of three panels. Left panels: volume mixing ratios, expressed in ppmv. Center panels: absolute differences, expressed in ppmv. Right panels: relative differences, expressed in percentage. The dashed lines represent the standard deviation of the median which, in some cases, is smaller than the thickness of the profile line, causing the dashed line not to be distinguishable.

(not shown). Moreover, none of the profiles of the retrieved products present structures characterised by particular features. Therefore it is possible to carry out comparisons just by interpolating the profiles over a common 40 - 100 km altitude grid with a 1 km resolution. Denoting with i a couple of coincident measurements, the absolute and relative difference of the retrieved product will be, respectively:

$$\delta_{abs,i}(z) = x_{SMR} - x_{comp} \quad (8)$$

$$\delta_{rel,i}(z) = \frac{x_{SMR} - x_{comp}}{(x_{SMR} + x_{comp})/2}. \quad (9)$$

x_{SMR} and x_{comp} are the retrieved H₂O or O₃ mixing ratios or temperature at altitude z for the coincidence i , from SMR and the instrument considered for the comparison, respectively. Measurements done by satellite instruments are in general affected by large uncertainties, so when comparing measurements of two satellites their relative difference is referred to the mean of the two, not to prefer any instrument as a reference (Randall et al., 2003). Being $\Delta(z)$ the median of the $N(z)$ differences (absolute or relative) measured at altitude z , the dispersion of the measurements is represented by the standard deviation of the median:

$$SEM(z) = \frac{1}{\sqrt{N(z)}} \sqrt{\frac{1}{N(z)-1} \sum_{i=1}^{N(z)} (\delta_i(z) - \Delta(z))^2}. \quad (10)$$

The median is used, instead of the mean, to minimize the impact of outliers data. Below we present the results of the comparisons in form of profiles averaged over the totality of the coincidences, regardless of time or location. This is done for H₂O but not for O₃ and Temperature, whose plots are however shown in the appendix and referred to in the text. For greater clarity,

no monthly or seasonal average profiles are shown, but seasonal zonal means of VMR relative differences and temperature absolute differences are also included in the appendix and referred to.

4.1 MIPAS

The Michelson Interferometer for Passive Atmospheric Sounding (MIPAS) on board Envisat performed mid-infrared limb sounding of the atmosphere between March 2002 and April 2012, when contact with the satellite was lost. Envisat was on a 98.55° inclination and 22:00 hrs ascending node sun-synchronous orbit at 800 km altitude. The retrieval products used for comparison in this study are obtained with the retrieving processor developed at the Karlsruhe Institute of Meteorology and Climate Research (IMK) and the Instituto de Astrofísica de Andalucía (IAA) (e.g., Sheese et al., 2017), whose forward model includes non-LTE effects. The characteristics of the MIPAS V5 datasets being used are summarized in Table 2. Quality filtering of the data, as indicated in Kiefer and Lossow (2017), has been performed. In March 2004, MIPAS underwent a malfunctioning and was made again operative in January 2005. During the first period, the instrument was being used in full spectral resolution (FR mission) while, in the second period, it was made again operative with a reduced spectral resolution (OR mission) (Oelhaf, 2008).

Table 2. Characteristics of the MIPAS H₂O, O₃ and temperature datasets used for comparison. Vertical resolutions refer to the observations in the altitude range 40 - 100 km considered in this study.

Observation Mode	Altitude Range	Product	Vertical Resolution	Spectral Resolution Mode	Time Period	Version
Nominal (NOM)	10 - 70 km	H ₂ O	5 - 15 km	Full Resolution (FR)	July 2002 → March 2004	V5H_H2O_20
		O ₃	5 - 15 km			V5H_O3_21
		T	/			/
		H ₂ O	5 - 16 km	Optimized Resolution (OR)	January 2005 → April 2012	V5R_H2O_220
		O ₃	4 - 13 km			V5R_O3_224
		T	/			/
Middle Atmosphere (MA)	20 - 100 km	H ₂ O	4 - 10 km	Optimized Resolution (OR)	January 2005 → April 2012	V5R_H2O_522
		O ₃	3 - 11 km			V5R_O3_522
		T	3 - 9 km			V5R_T_521
Upper Atmosphere (UA)	42 - 150 km	H ₂ O	3 - 10 km	Optimized Resolution (OR)	January 2005 → April 2012	V5R_H2O_622
		O ₃	3 - 11 km			V5R_O3_622
		T	3 - 9 km			V5R_T_621

4.1.1 Nominal mode

Both Nominal Mode datasets altogether (from FR and OR missions) are here considered for comparison with SMR. The FR and OR data sets are not presented separately since SMR–MIPAS H₂O relative differences are similar in the two cases, with

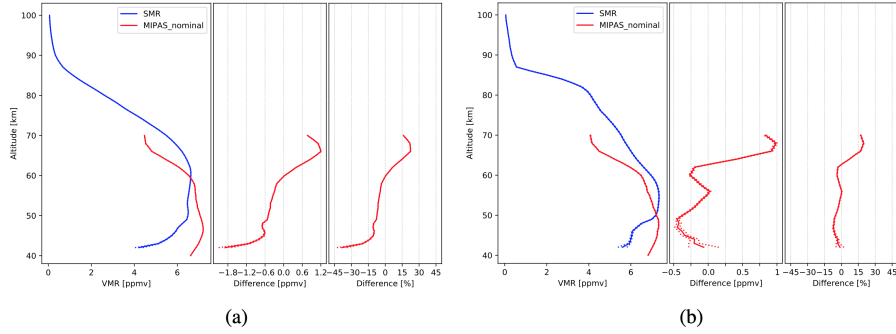


Figure 7. Comparison of SMR H_2O concentrations, from FM13 (a) and FM19 (b), with the ones from MIPAS Nominal Mode retrievals. The data plotted are global averages over the whole time between periods indicated in Table 2. Figures characteristics are the same as in Figure 6.

only a variation of 10% between FR and OR for comparisons with SMR FM19, between 45 - 50 km altitude (not shown). For comparisons with SMR FM13, no variations between FR and OR are to be reported since only a small quantity of SMR FM13 measurements have been performed during the period of MIPAS FR mission (see Figure 3). SMR H_2O average profiles for FM13 and FM19, averaged over all the coincidences found, show different agreement with MIPAS. FM19 relative difference (see Figure 7:b) is very low between 40 - 60 km altitude staying close to 0%, assuming low negative values that peak at -5% at 45 and 60 km. Between 60 - 70 km the difference increases with altitude to reach +15% at 70 km. Looking at latitudes and seasons specifically (Figure A10), a peak of +30% is observed around 65 km at -20° during northern spring; while -20% relative differences are observed between 50-70 km during southern winter and autumn at high latitudes. FM13 instead (Figure 7:a) presents a major negative difference of -40% at 40 km, decreasing to -10% at 45 km. Between 45 - 70 km, the difference value increase and reaches +20%. The highest positive differences, of +40% are registered between 60 - 70 km during local summer and spring in both hemispheres (Figure A9) at high latitudes. Regarding O_3 daytime concentrations (Figure A19), for both FM13 and FM19, SMR-MIPAS relative differences are on average of -60% (out of shown scale) at 70 km and increase in value with decreasing altitudes to reach roughly 0% at 50 km and then go down to -15% at 45 km. Seasonal zonal means (Figures A31 and A33) show, for both FMs, peaks of -120% at 70 km in both hemispheres at 50° latitude during all seasons. Nighttime SMR O_3 concentrations show, for FM13, a relative difference of +15% at 40 km which goes to about -10% at 45 km, stays constant up to 60 km and then decreases to -20% at 70 km (Figure A20a). Peaks of -90% are observed in both hemispheres during local spring and summer at 70 km, at mid latitudes (Figure A32). FM19 O_3 relative difference instead has a value of -15% at 40 km which goes to 0% at 55 km and then back again to -15% at 70 km (Figure A20b). Looking at seasons and latitudes separately (Figure A34), we observe peaks of -100% at 70 km in both hemispheres at mid latitudes during all seasons.

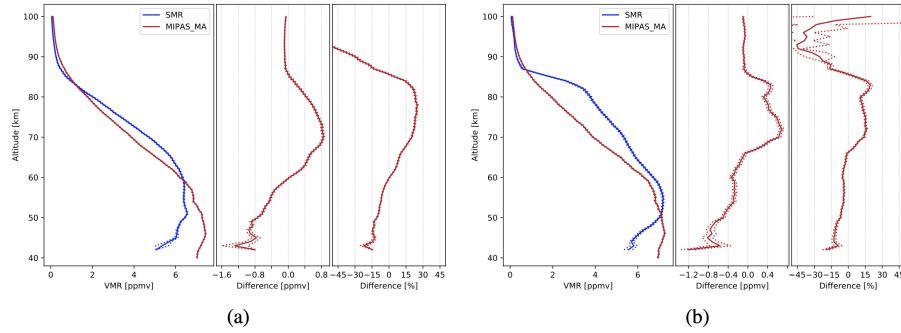


Figure 8. Comparison of SMR H₂O concentrations, from FM13 (a) and FM19 (b), with the ones from MIPAS Middle Atmosphere Mode retrievals. The data plotted are global averages over the whole time periods indicated in Table 2. Figures characteristics are the same as in Figure 6.

4.1.2 Middle atmosphere mode

H₂O profile comparison with OR Middle Atmosphere mode, shown, presents for both FMs a relative difference of -15% at 40 km which goes toward 0% with altitude until 60 km. Regarding FM19 (Figure 8:b), it then increases up to +15% at 80 km and decreases to -45% between 80 - 90 km; finally, it increases again to reach +15% at 100 km. For FM13 instead (Figure 8:a), the relative difference increases up to almost 30% between 60 - 80 km and then it decreases up to -120% (out of shown scale) towards high altitudes. For both FMs, peaks of -150% are observed for all seasons between 90 and 100 km at low latitudes. Moreover, regarding FM19, high values of relative difference, with peaks of +100%, are registered between 90 - 100 km during southern autumn and winter at high latitudes (Figures A11 and A12). O₃ daytime profiles (Figure A21) are very similar for the two FMs, with relative differences close to 0% between 40 - 50 km which then decrease up to -15% between 50 - 70 km. Differences then increase quickly to +70% between 70 - 80 km and subsequently steeply decrease to -150% at higher altitudes. O₃ nighttime relative differences (Figure A22) have, for both FMs, a value of -15% at 40 km and then stays around 0% between 45 - 70 km. The trend of the profile above 70 km is similar to the one from daytime O₃. These high differences above 70 km are to be attributed to the weakness of the SMR O₃ line observed with FMs 13 and 19 at such altitudes. This causes the measurement response of the retrieval to often be higher than the 0.75 threshold, resulting in the measurement to be discarded. Thus significantly fewer and more fluctuating measurements are considered in the global average at those altitudes, so that the average is characterised by high uncertainties. Temperature absolute differences are close to 0 K between 40 - 80 km and decrease up to -45 K at higher altitudes, for both FMs (Figure A51).

4.1.3 Upper atmosphere mode

H₂O average relative differences between SMR and MIPAS OR Upper Atmosphere profiles present a value of -30% at 40 km for FM13 (Figure 9:a) which gets smaller with altitude to reach 0% at 65 km. The value keeps increasing with altitude until 80 km where it reaches +20% and then decreases to about -100% at higher altitudes. Relative difference regarding FM19 (Figure

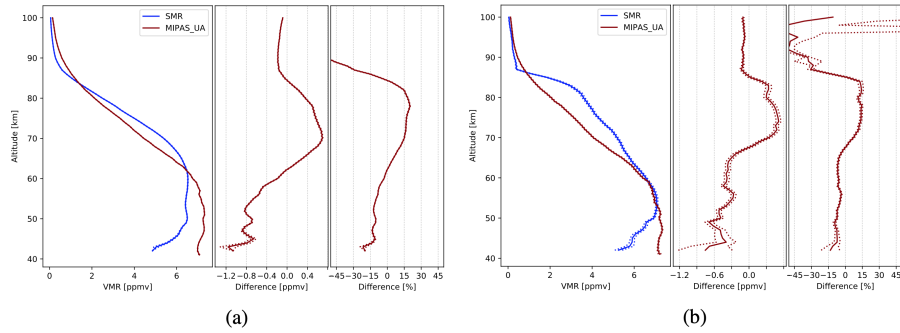


Figure 9. Comparison of SMR H_2O concentrations, from FM13 (a) and FM19 (b), with the ones from MIPAS Upper Atmosphere Mode retrievals. The data plotted are global averages over the whole time periods indicated in Table 2. Figures characteristics are the same as in Figure 6.

9:b) is equal to -15% at 40 km and keeps being roughly constant with altitude until it goes to 0% a little below 70 km, it then increases to 15%, a value observed unvaryingly between 70 - 85 km. The difference then decreases between 85 - 95 km and reaches values of about -60% to increase again up to -10% at 100 km. Peaks of -150% are registered between 90 - 100 km at low latitudes during all seasons except, for both FMs (Figures A13 and A13). Moreover, FM19 shows also a peak of +100% during southern winter at high latitudes. O_3 daytime relative difference profiles (Figure A23) show similar trends for both FMs, with a 0% value registered at 40 km which goes to -15% at 45 km and then back to 0% at 50 km. The difference then slowly decreases with altitude and reaches -20% at 70 km. Nighttime relative differences (Figure A24) show, for both FMs, a value of +20% at 40 km, decreasing to about -10% at 45 km. The value then stays constant with altitude up till 70 km. All considerations about O_3 profiles above 70 km are the same as in Section 4.1.2. Temperature absolute difference is similar to what is observed for comparison with the Middle Atmosphere mode.

4.2 ACE-FTS

The Fourier Transform Spectrometer (FTS), an instrument which is part of the Canadian-led Atmospheric Chemistry Experiment (ACE), was launched on board Scisat-1 on 12 August 2003 and it is still operating today. The satellite travels at 650 km altitude, with an orbit characterised by a 74° inclination. The instrument measures H_2O and O_3 concentrations between 5 - 100 km, and temperature up till 125 km, with a 3 - 4 km vertical resolution. For comparison, we use here the ACE-FTS v3.6 dataset (Sheese et al., 2017), quality filtered as indicated by the instrument team (Sheese et al., 2015).

SMR-ACE H_2O profile comparison, with regards to FM13 (Figure 10:a), shows a -60% relative difference at 40 km, then the value goes steeply to 0% and stays almost constant between 45 - 80 km altitude. Between 80 - 100 km the relative difference value goes down and reaches values of -140%. For FM19 (Figure 10:b), the measured relative difference is -15% below 45 km and 0% between 45 - 50 km; it then decreases slowly with altitude until 80 km where it is equal to -30%. Between 80 - 100 km

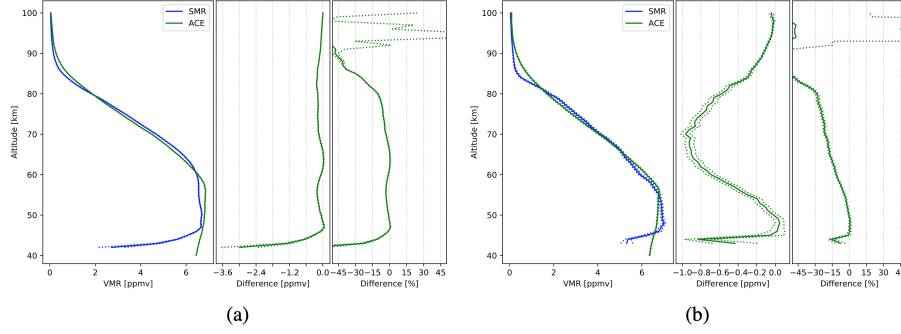


Figure 10. Comparison of SMR H_2O concentrations, from FM13 (a) and FM19 (b), with the ones from ACE-FTS retrievals. The data plotted are global averages over the whole time between February 2004 and April 2019. Figures characteristics are the same as in Figure 6.

it decreases more rapidly to about -60%. With regards to O_3 daytime measurements (Figure A25), for both FMs, SMR–ACE relative difference amounts to -15% between 40 - 50 km (with the exception of FM13 at 40 km being equal to +15%) to then decrease to -30% at 60 km. It then increases to 0% at 70 km. Nighttime O_3 relative differences (Figure A26), for both FMs, have a value of -15% between 40 - 55 km and then increase to +150% at 70 km. All considerations about O_3 profiles above 70 km are the same as in Section 4.1.2. O_3 SMR coincidences with ACE are limited to mid and high latitudes (Figures A43, A45, A44 and A44). Regarding temperature (Figure A53), FM13 absolute difference stays between 0 and 4 K until 80 km altitude, and at higher altitudes it oscillates between lower values within 0 and - 16 K. For FM19 instead, it assumes values between 0 and 7 K until 50 km, then it slowly decreases up to -15 K at 90 km, and between 90 - 100 km the difference is characterised by considerably lower values with a minimum of -60 K.

4.3 MLS

The Microwave Limb Sounder (MLS) operates on board Aura satellite since 15 July 2004, on a 705 km sun-synchronous orbit characterized by a 98° inclination and a 13:45 hrs ascending node. Aura/MLS observes between 118 GHz and 2.5 THz with a 1.5 - 3 km vertical resolution (Schoeberl et al., 2006). We use MLS measurements of temperature, as well as H_2O and O_3 concentrations, from the v4 dataset to which the recommended quality filtering has been applied (Livesey et al., 2018), excluding data above 75 km altitude, with regards to H_2O and O_3 concentrations, and above 95 km for the retrieved temperature.

Comparing SMR H_2O profiles from FM13 with MLS (Figure 11:a), we observe a relative difference of -45% at 40 km which rapidly goes to -15% at 45 km. It then slowly decreases to 0% between 45 - 60 km and, specularly, goes back to -15% between 60 - 80 km. Above 80 km, it decreases more quickly with altitude and reaches -110%. Regarding comparison with FM19 profile, the difference is equal to -15% at 40 km, gets smaller between 40 - 55 km reaching 0%, and between 55 - 100 km it goes down up to -160%. Peaks of -150% are observed at 90 km during local winter and autumn in both hemispheres for both FMs (Figures A17 and A18). O_3 daytime relative difference profiles show, for FM13 (Figure A27a), a value of -30% at 40 km

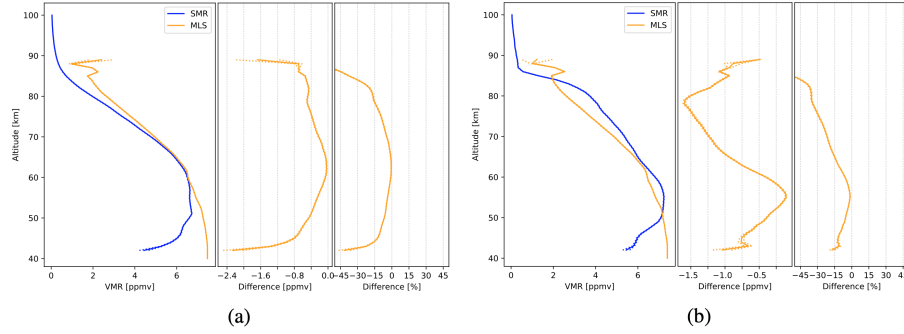


Figure 11. Comparison of SMR H₂O concentrations, from FM13 (a) and FM19 (b), with the ones from MLS retrievals. The data plotted are global averages over the whole time between July 2004 and April 2019. Figures characteristics are the same as in Figure 6.

which decreases to -10% at 45 km. Between 45 - 55 km, the value stays constant, then it goes to -60% at 70 km and to 0% at 75 km. FM19 (Figure A27b) presents an average relative difference of 0% at 40 km which decreases to -15% at 45 km and then goes back to 0% at 50 km. The goes down up to -60% at 70 km and then it goes up to -15% around 75 km. Nighttime FM13 O₃ profiles show a relative difference of +30% at 40 km which goes down to - 10% at 45 km and then gradually increases to reach +30% at 70 km (Figure A28a). FM19 presents a relative difference of -15% at 40 km which gradually increases to +15% at 70 km (Figure A28b). For both FMs, nighttime relative differences show positive values above 50 km during local autumn and winter, for both hemispheres, from low to high latitudes, with peaks of +30% around 70 km. Negative differences with peaks of -90% are observed at 70 km during local spring and summer at mid latitudes in both hemispheres (Figures A48 and A50). All considerations about O₃ relative differences between 70 -75 km are the same as in Section 4.1.2. Temperature absolute difference for FM13 (Figure A54) is equal to 8 K at 40 km, goes to 0 K, increases back up to 8 K at 50 km. The values is constant with altitude between 50 - 70 km. The difference then decreases up to 0 K between 70 - 90 km and subsequently drops to -32 K at 95 km. FM19 shows a decrease in temperature from 8 K at 40 km to -8 K at 90 km, and eventually drops to -32 K at 95 km.

5 Conclusions

The previous version (v2.1) of SMR H₂O retrievals presented high biases compared to other instruments. After investigating different possible causes, we identified the origin of these biases in the mistaking of spurious signal from sideband leakage for actual signal of interest. This was caused by having overestimated the capability of image band suppression performed by the frontends employed for H₂O measurements. A lower suppression has therefore been assumed and retrievals with the new settings have been performed. This resulted in a new dataset (v3.0) covering 18 years of observations from 40 to 100 km altitude, across all latitudes. Time series of H₂O concentration show signals of known semi-annual oscillation and annual cycle, as well as signals of the 11-year solar cycle. The validation study, performed by comparing with satellite measurements from MIPAS, ACE-FTS and MLS, shows that globally averaged SMR v3.0 FM13 H₂O concentrations (Figure 12) present

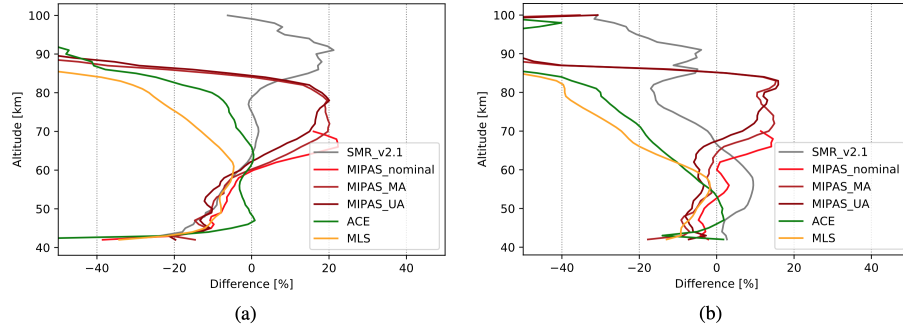


Figure 12. Summary of relative differences between SMR v3.0 H₂O concentrations and SMR v2.1 ones as well as those retrieved by all other instruments considered in this study. For the sake of clarity, errors are not shown. Panel a: FM13 comparison. Panel b: FM19 comparison.

relative differences within $\pm 20\%$ between 45 - 80 km altitude. In particular SMR and ACE-FTS are in very good agreement in this altitude range, with relative differences within 0% and -5%. Relative differences between v3.0 FM19 and all instruments are within $\pm 20\%$ between 40 - 70 km, this being true for comparison with MIPAS up till 80 km. In Figure 12b it can also be seen how between SMR v3.0 and v2.1, for FM19, between 40 - 70 km, there is an improvement of about 10% in the relative differences with regards to all the compared instruments. For both FMs, outside the above mentioned altitude ranges, relative differences reach highly negative values, to a minimum of -160%. Regarding the other retrieval products of these FMs: compared to the other instruments' measurements, temperature shows (Figure A67) an improvement of about 5 K in absolute difference at all observed altitudes with respect to the old version, for both FMs. Only FM19 in the 40 - 60 km is an exception, where v2.1 agreed better with the other instruments. Temperature from v3.0 FM13 agrees very well with all MIPAS modes and with ACE-FTS between 40 - 85 km, presenting absolute differences within ± 3 K. In the same altitude range, SMR-MLS difference instead oscillates between +8 K and 0 K. SMR v3.0 FM19 Temperature absolute difference from all other instruments is equal to +8 K at 40 km and gradually decreases to reach - 8 K at 85 km. For both FMs, altitudes above 85 km are characterised by lower absolute differences, reaching - 60 K at 100 km. Daytime O₃ v3.0 retrieved concentrations (Figure A65) present relative differences between +5% and -30% between 40 - 70 km, for both FMs, with respect to ACE-FTS and the MIPAS MA and UA modes. Difference with respect to MLS and MIPAS Nominal mode instead decreases up to -60% at 70 km. In particular, FM19 shows an improvement respect to v2.1 that increases with altitude in this range (Figure A65b). The agreement between average nighttime SMR v3.0 O₃ and the other instruments (Figure A66) is better compared to the daytime average, due to lower variability of O₃ during the night, especially compared to MIPAS. The relative difference compared to all MIPAS modes is around -10% between 45 - 70 km, while SMR-ACE and SMR -MLS differences have values within $\pm 30\%$ at 40 - 70 km altitude. Above 70 km the O₃ line observed with these FMs is weaker, causing the average retrieved concentration to be characterised by higher variability. Hence the very high relative differences measured above 70 km. There is improvement with respect to v2.1 only for SMR-MIPAS comparisons, but not for SMR-ACE or SMR-MLS. These high differences above 70 km are to be attributed to the weakness of the SMR O₃ line observed with FMs 13 and 19 at such altitudes. This causes the measurement response of the retrieval to often be higher than the 0.75 threshold, resulting in the measurement to be discarded.

Thus significantly fewer and more fluctuating measurements are considered in the global average at those altitudes, so that the average is characterised by high uncertainties.

The improvement of this SMR H₂O dataset will be of great value for the study of mesospheric dynamics and H₂O-related chemical processes, given the big time and space extension of the dataset.

5 Appendix A

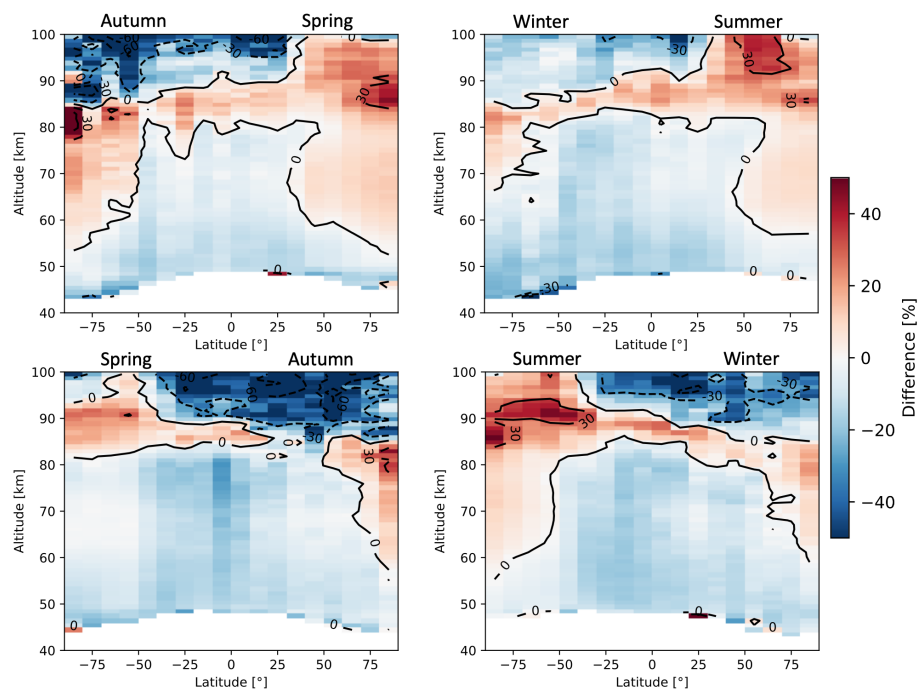


Figure A1. Seasonal zonal means of H_2O FM13 SMR v3.0–v2.1 relative differences averaged over the whole time period between February 2001 and April 2019. The seasons are intended as the time between solstice and equinox.

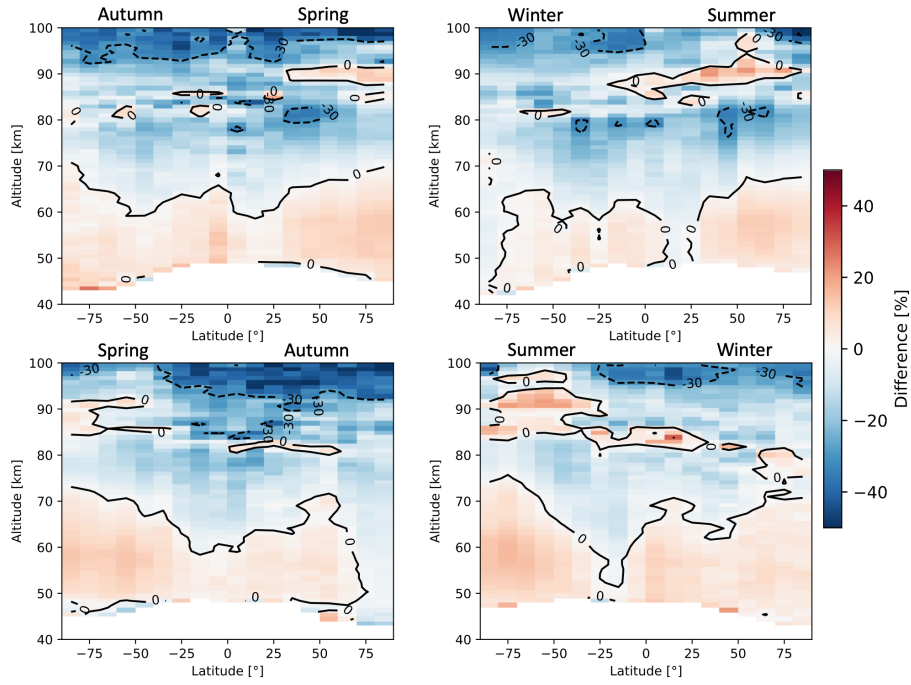


Figure A2. Seasonal zonal means of H_2O FM19 SMR v3.0–v2.1 relative differences averaged over the whole time period between February 2001 and April 2019. The seasons are intended as the time between solstice and equinox.

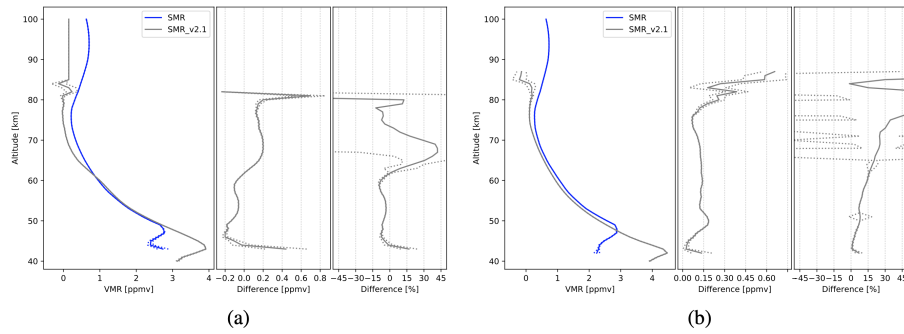


Figure A3. Comparison of SMR v3.0 and v2.1 O_3 concentrations, from FM13 (a) and FM19 (b). The data plotted are global averages over the whole time period between February 2001 and April 2019. Figures characteristics are the same as in Figure 6.

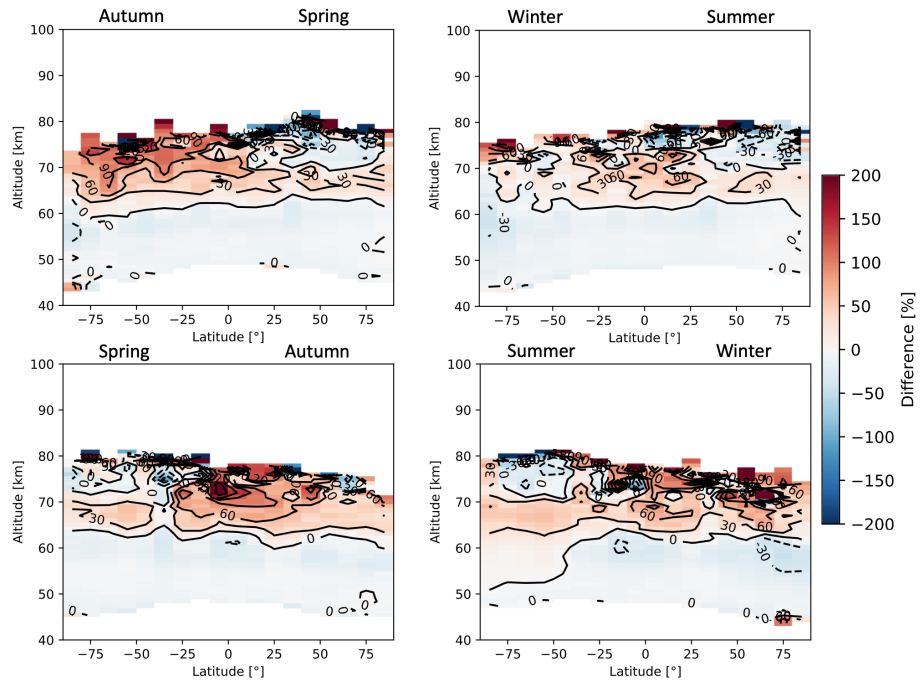


Figure A4. Seasonal zonal means of O₃ FM13 SMR v3.0–v2.1 relative differences averaged over the whole time period between February 2001 and April 2019. The seasons are intended as the time between solstice and equinox.

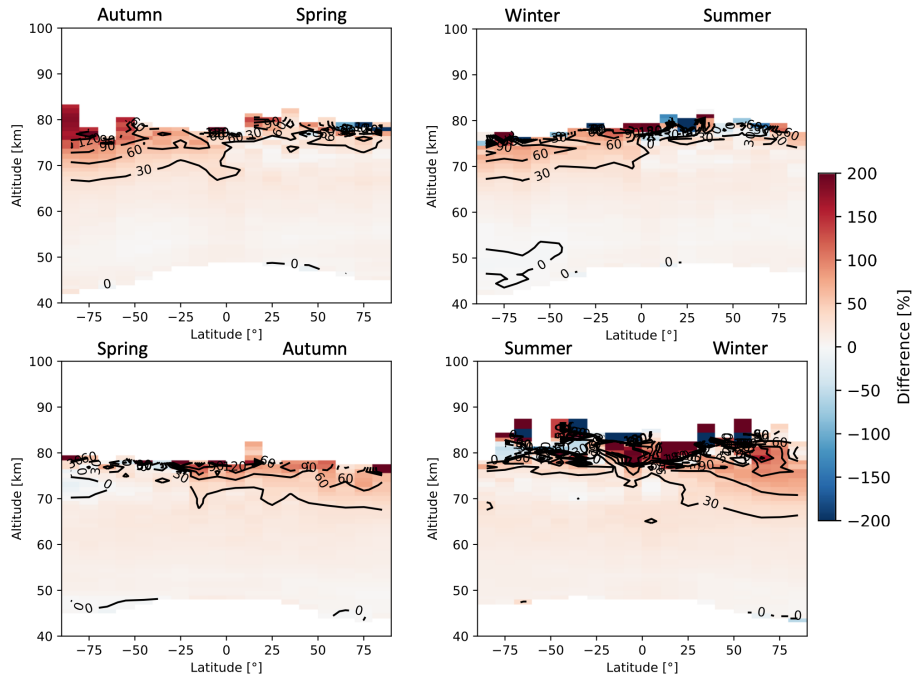


Figure A5. Seasonal zonal means of O_3 FM19 SMR v3.0–v2.1 relative differences averaged over the whole time period between February 2001 and April 2019. The seasons are intended as the time between solstice and equinox.

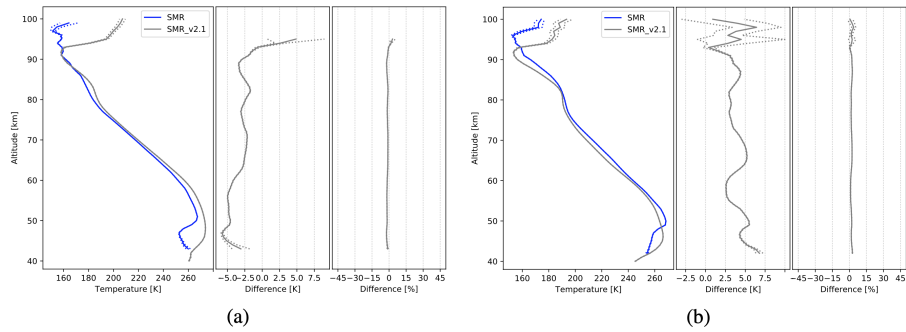


Figure A6. Comparison of SMR v3.0 and v2.1 Temperatures from FM13 (a) and FM19 (b). The data plotted are global averages over the whole time period between February 2001 and April 2019. Figures characteristics are the same as in Figure 6.

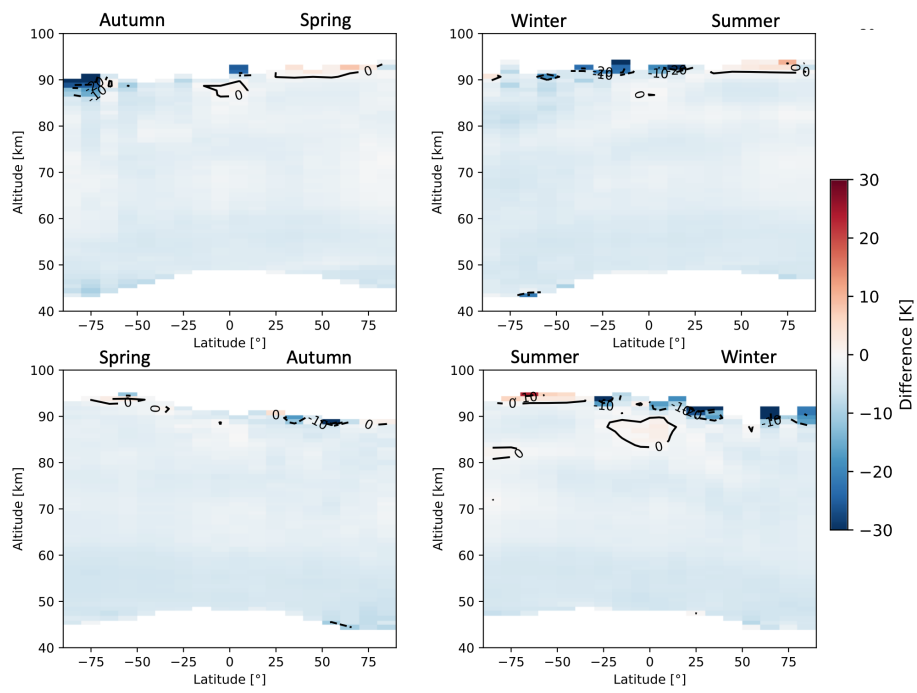


Figure A7. Seasonal zonal means of Temperature FM13 SMR v3.0–v2.1 relative differences averaged over the whole time period between February 2001 and April 2019. The seasons are intended as the time between solstice and equinox.

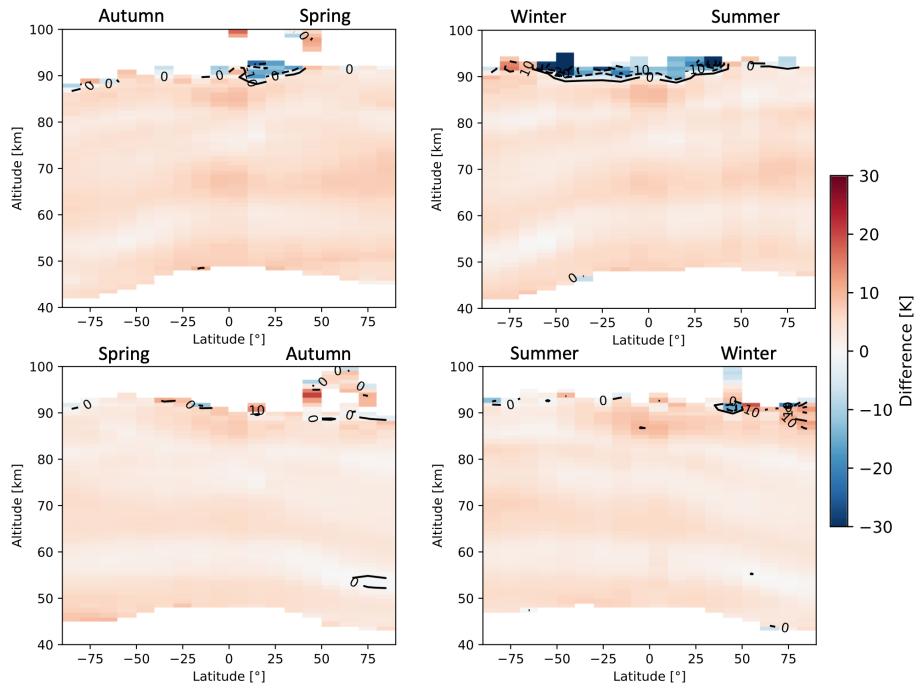


Figure A8. Seasonal zonal means of Temperature FM19 SMR v3.0–v2.1 relative differences averaged over the whole time period between February 2001 and April 2019. The seasons are intended as the time between solstice and equinox.

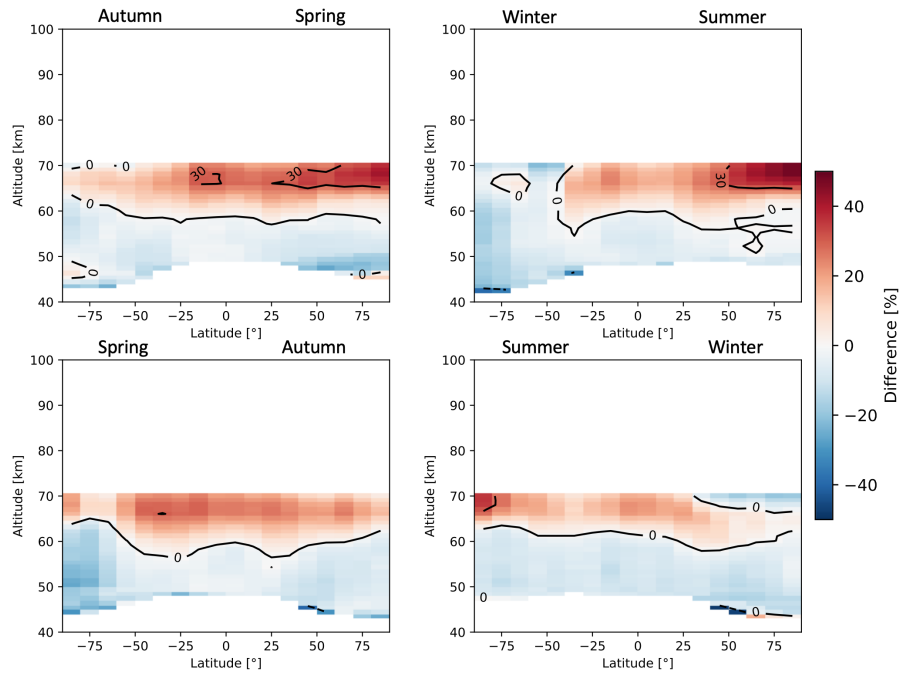


Figure A9. Seasonal zonal means of H₂O FM13 SMR–MIPAS Nominal relative differences averaged over the time period indicated in Table 2. The seasons are intended as the time between solstice and equinox.

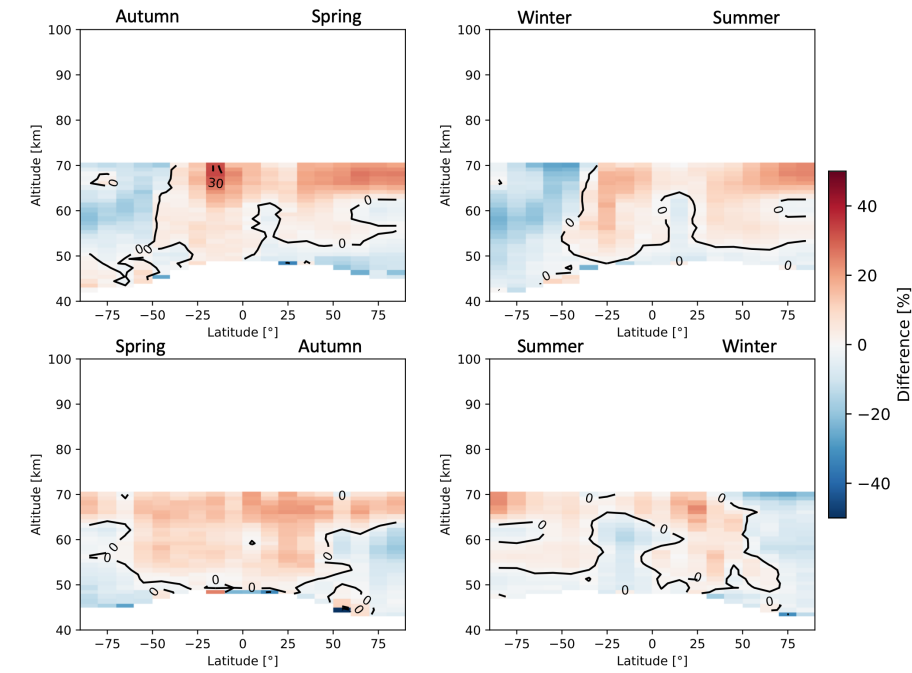


Figure A10. Seasonal zonal means of H₂O FM19 SMR–MIPAS Nominal relative differences averaged over the time period indicated in Table 2. The seasons are intended as the time between solstice and equinox.

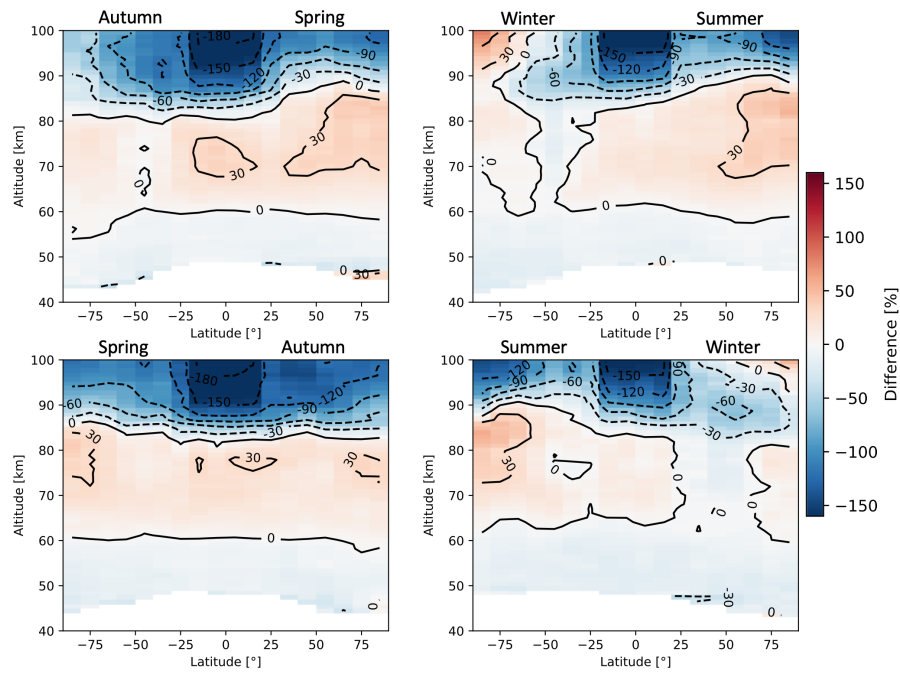


Figure A11. Seasonal zonal means of H_2O FM13 SMR-MIPAS Middle Atmosphere relative differences averaged over the time period indicated in Table 2. The seasons are intended as the time between solstice and equinox.

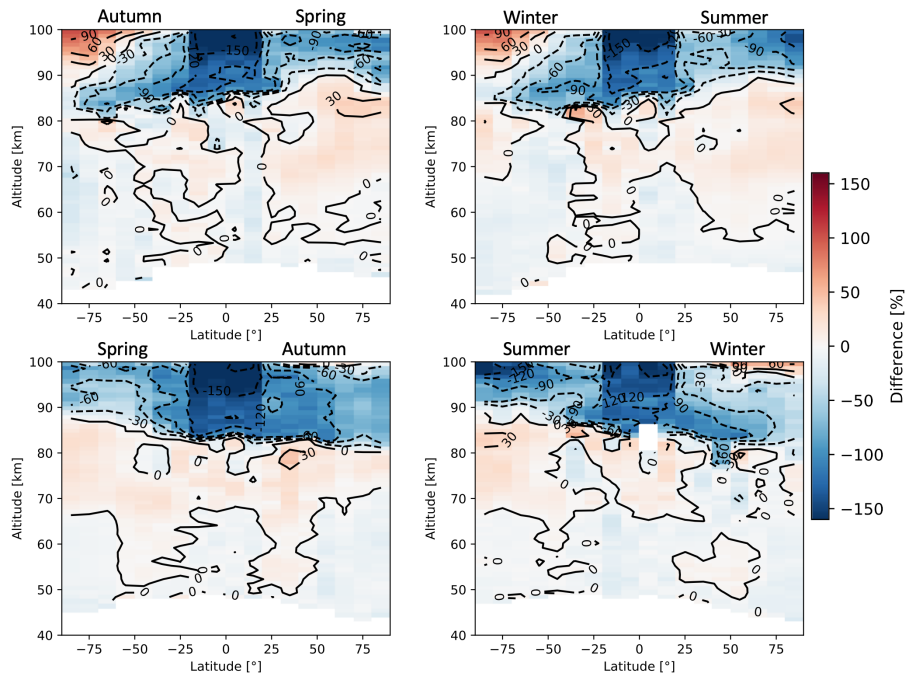


Figure A12. Seasonal zonal means of H_2O FM19 SMR–MIPAS Middle Atmosphere relative differences averaged over the time period indicated in Table 2. The seasons are intended as the time between solstice and equinox.

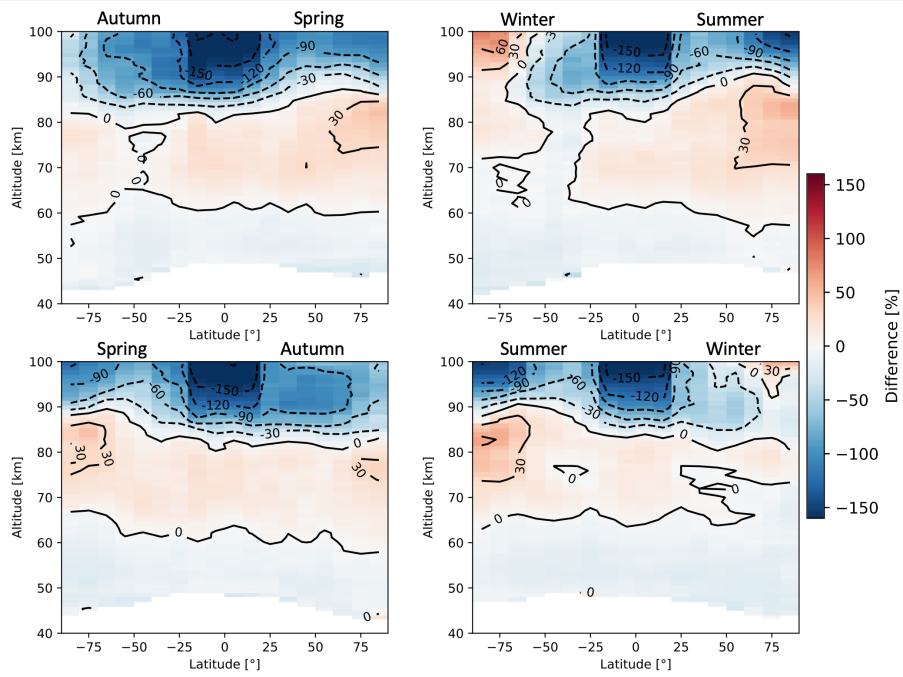


Figure A13. Seasonal zonal means of H₂O FM13 SMR-MIPAS Upper Atmosphere relative differences averaged over the time period indicated in Table 2. The seasons are intended as the time between solstice and equinox.

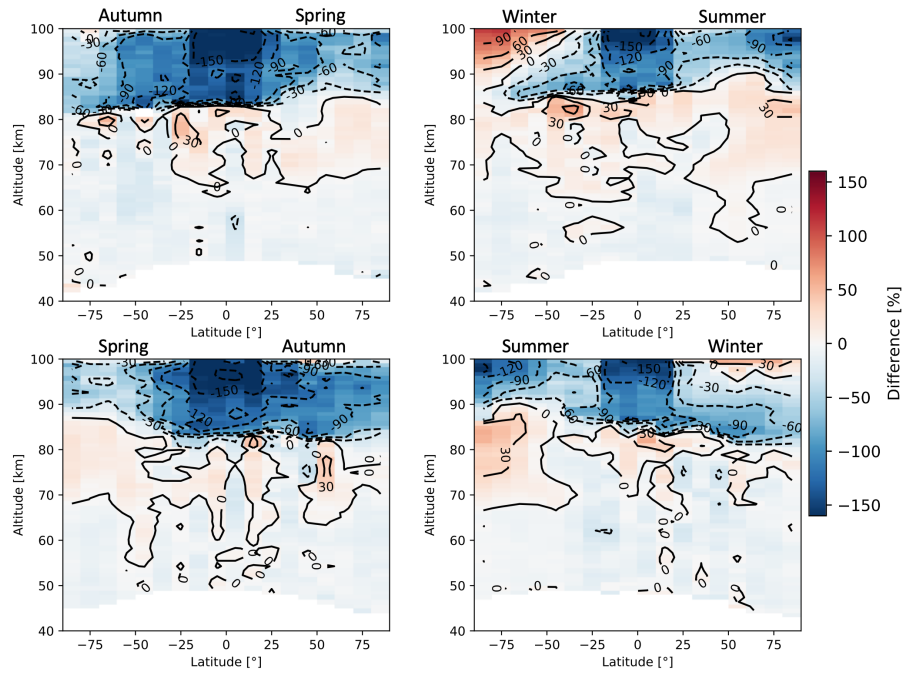


Figure A14. Seasonal zonal means of H₂O FM19 SMR-MIPAS Upper Atmosphere relative differences averaged over the time period indicated in Table 2. The seasons are intended as the time between solstice and equinox.

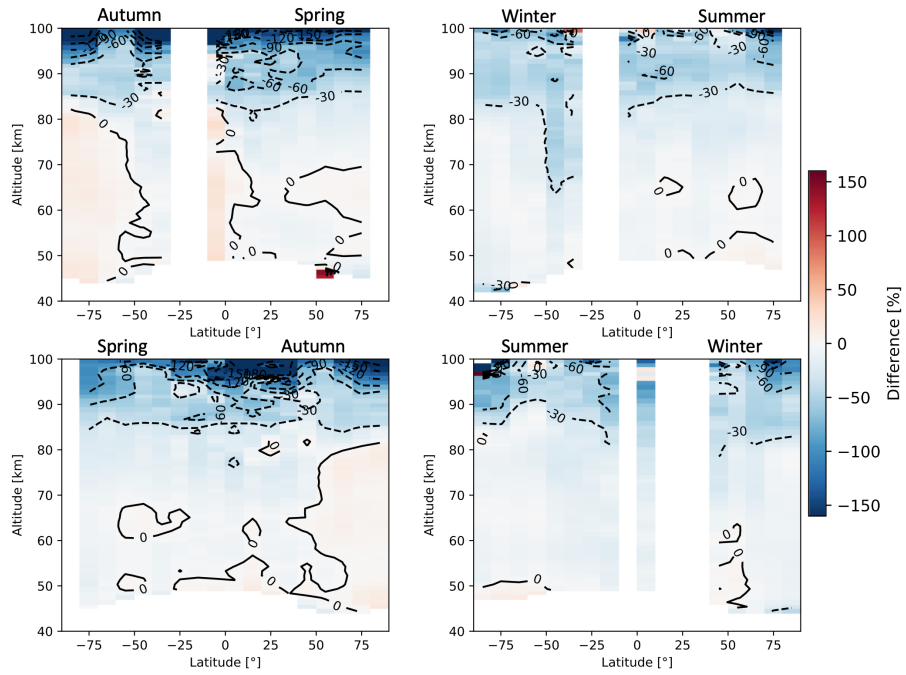


Figure A15. Seasonal zonal means of H_2O FM13 SMR-ACE relative differences averaged over the time period between February 2004 and April 2019. The seasons are intended as the time between solstice and equinox.

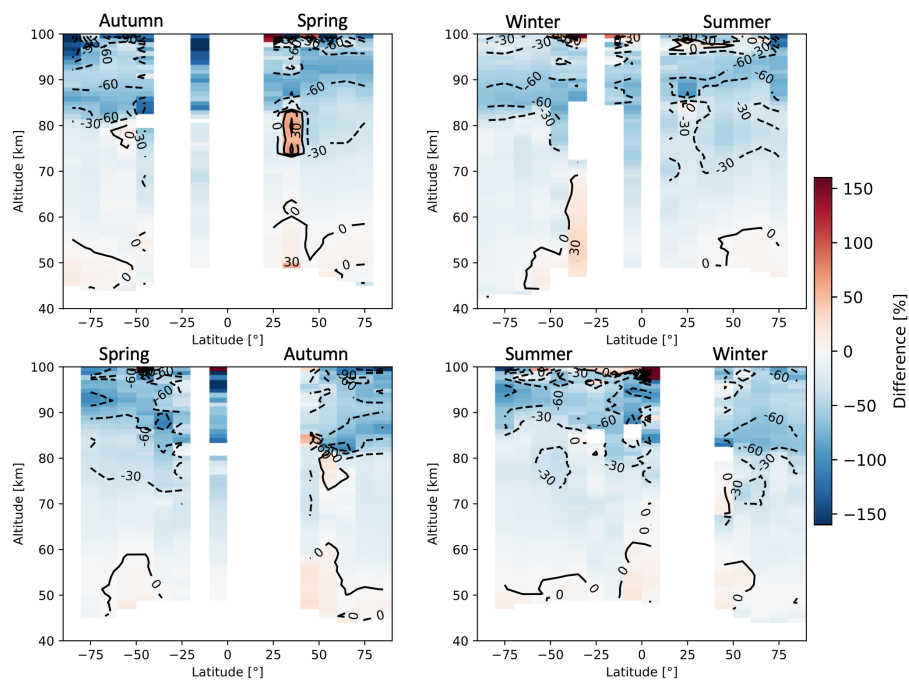


Figure A16. Seasonal zonal means of H_2O FM19 SMR-ACE relative differences averaged over the time period between February 2004 and April 2019. The seasons are intended as the time between solstice and equinox.

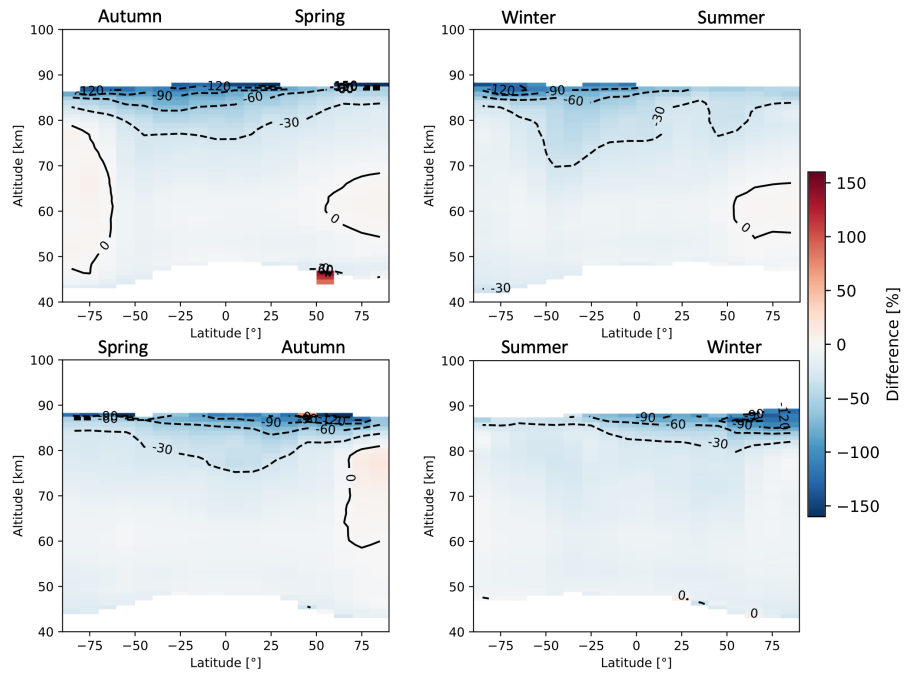


Figure A17. Seasonal zonal means of H₂O FM13 SMR-MLS relative differences averaged over the time period between July 2004 and April 2019. The seasons are intended as the time between solstice and equinox.

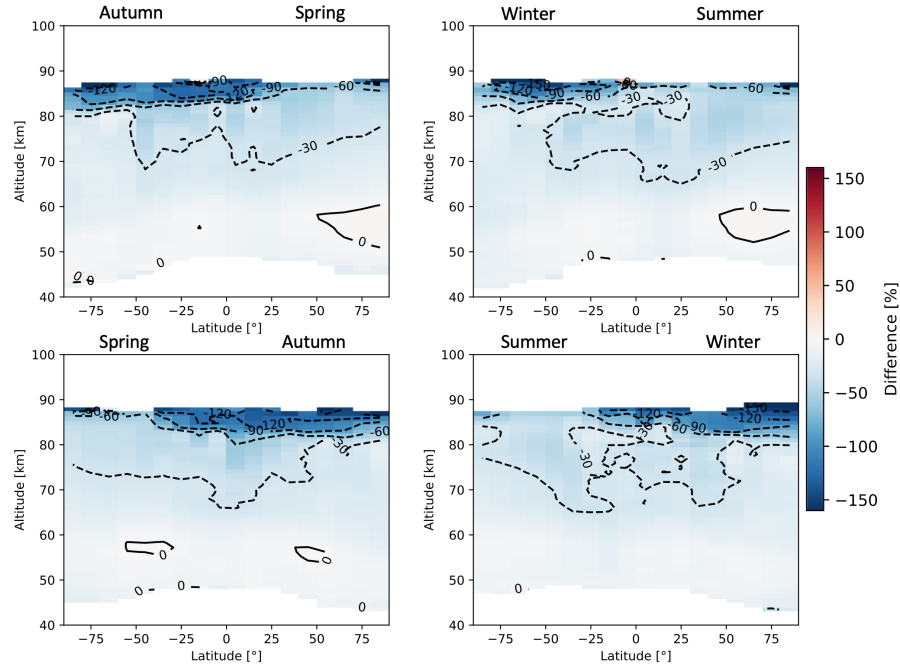


Figure A18. Seasonal zonal means of H₂O FM19 SMR-MLS relative differences averaged over the time period between July 2004 and April 2019. The seasons are intended as the time between solstice and equinox.

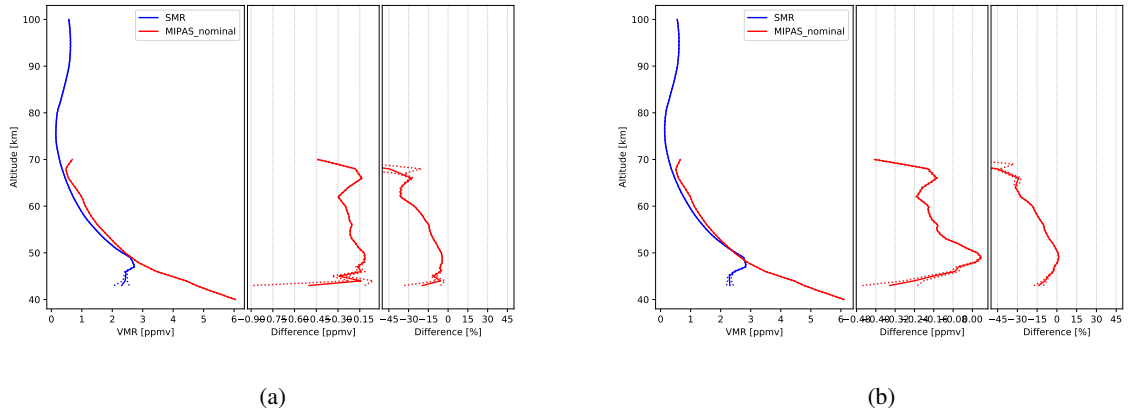


Figure A19. Comparison of SMR daytime O₃ concentrations, from FM13 (a) and FM19 (b), with the ones from MIPAS Nominal Mode retrievals. The data plotted are global averages over the whole time periods indicated in Table 2. Figures characteristics are the same as in Figure 6.

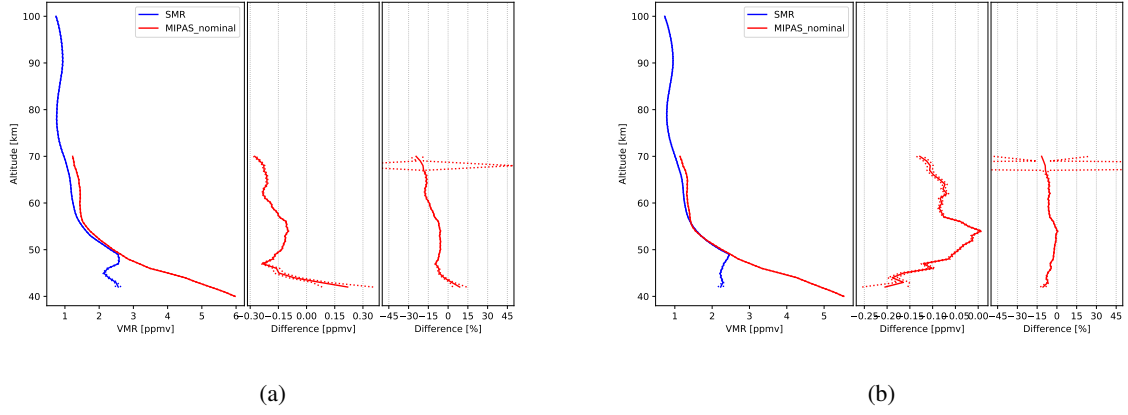


Figure A20. Comparison of SMR nighttime O₃ concentrations, from FM13 (a) and FM19 (b), with the ones from MIPAS Nominal Mode retrievals. The data plotted are global averages over the whole time periods indicated in Table 2. Figures characteristics are the same as in Figure 6.

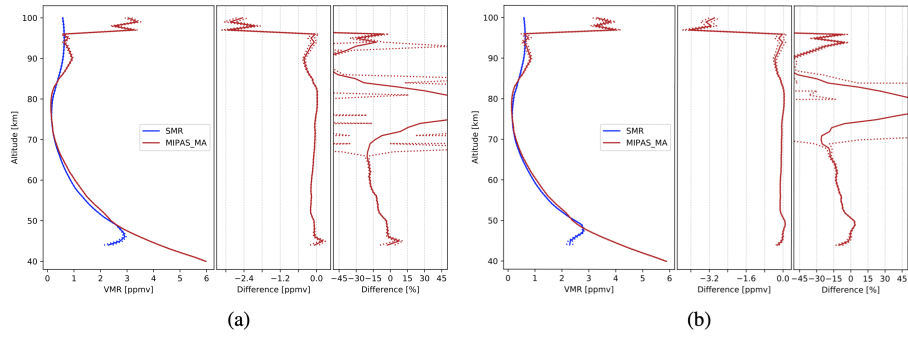


Figure A21. Comparison of SMR daytime O₃ concentrations, from FM13 (a) and FM19 (b), with the ones from MIPAS Middle Atmosphere Mode retrievals. The data plotted are global averages over the whole time periods indicated in Table 2. Figures characteristics are the same as in Figure 6.

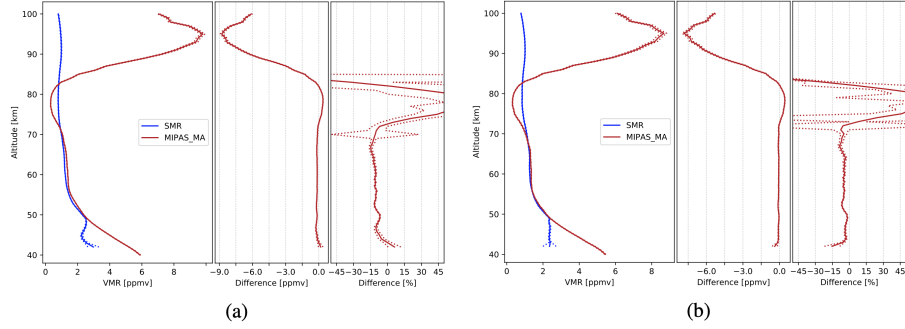


Figure A22. Comparison of SMR nighttime O_3 concentrations, from FM13 (a) and FM19 (b), with the ones from MIPAS Middle Atmosphere Mode retrievals. The data plotted are global averages over the whole time periods indicated in Table 2. Figures characteristics are the same as in Figure 6.

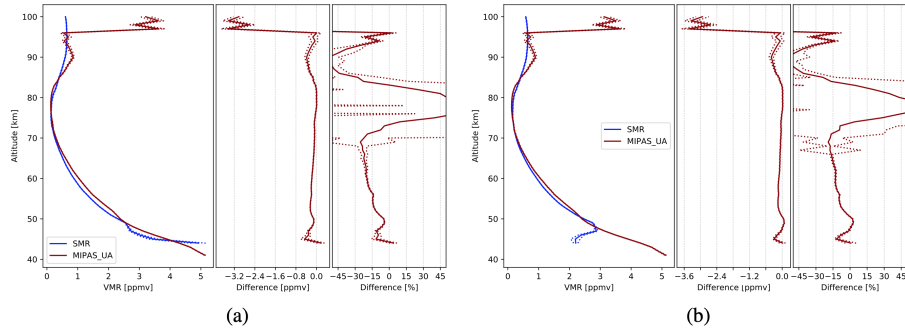


Figure A23. Comparison of SMR daytime O_3 concentrations, from FM13 (a) and FM19 (b), with the ones from MIPAS Upper Atmosphere Mode retrievals. The data plotted are global averages over the whole time periods indicated in Table 2. Figures characteristics are the same as in Figure 6.

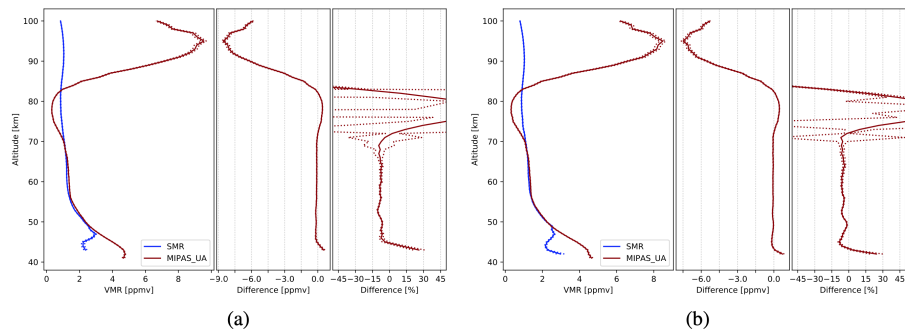


Figure A24. Comparison of SMR nighttime O_3 concentrations, from FM13 (a) and FM19 (b), with the ones from MIPAS Upper Atmosphere Mode retrievals. The data plotted are global averages over the whole time periods indicated in Table 2. Figures characteristics are the same as in Figure 6.

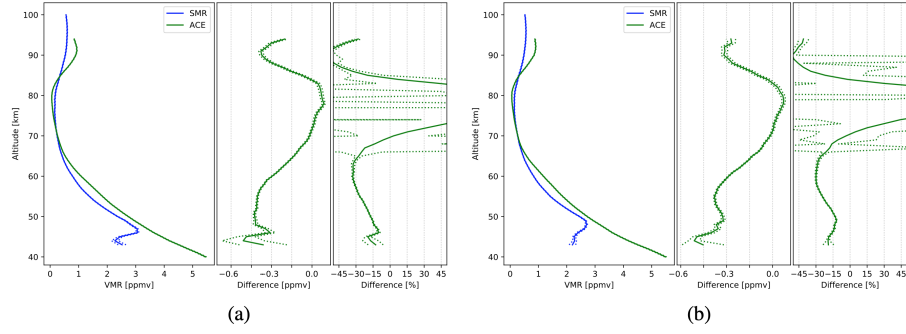


Figure A25. Comparison of SMR daytime O_3 concentrations, from FM13 (a) and FM19 (b), with the ones from ACE-FTS retrievals. The data plotted are global averages over the time period between February 2004 and April 2019. Figures characteristics are the same as in Figure 6.

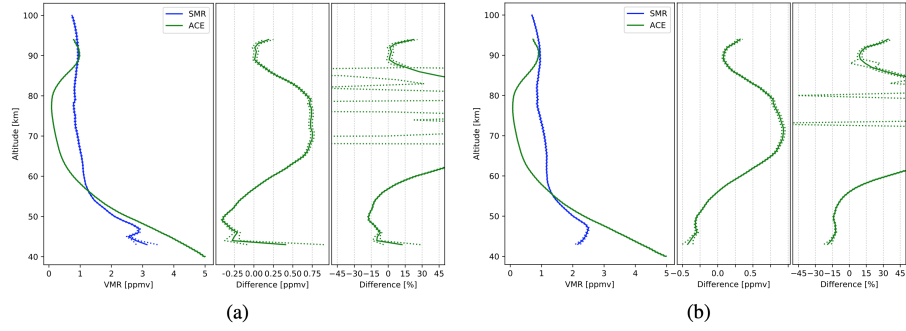


Figure A26. Comparison of SMR nighttime O_3 concentrations, from FM13 (a) and FM19 (b), with the ones from ACE-FTS retrievals. The data plotted are global averages over the time period between February 2004 and April 2019. Figures characteristics are the same as in Figure 6.

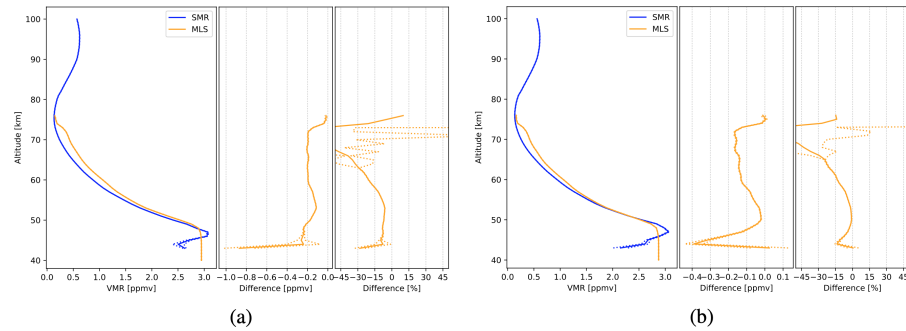


Figure A27. Comparison of SMR daytime O_3 concentrations, from FM13 (a) and FM19 (b), with the ones from MLS retrievals. The data plotted are global averages over the time period between July 2004 and April 2019. Figures characteristics are the same as in Figure 6.

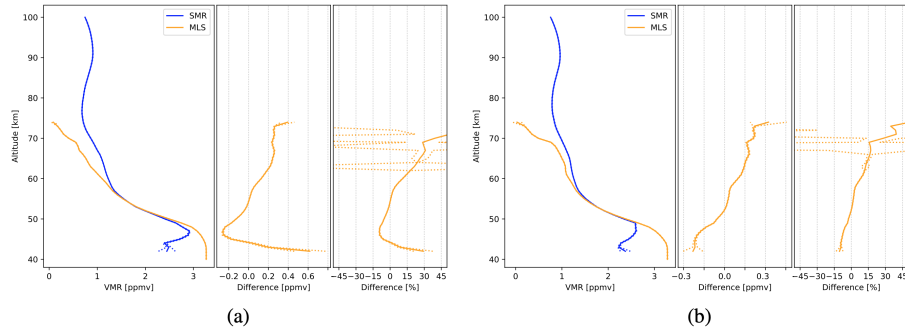


Figure A28. Comparison of SMR nighttime O_3 concentrations, from FM13 (a) and FM19 (b), with the ones from MLS retrievals. The data plotted are global averages over the time period between July 2004 and April 2019. Figures characteristics are the same as in Figure 6.

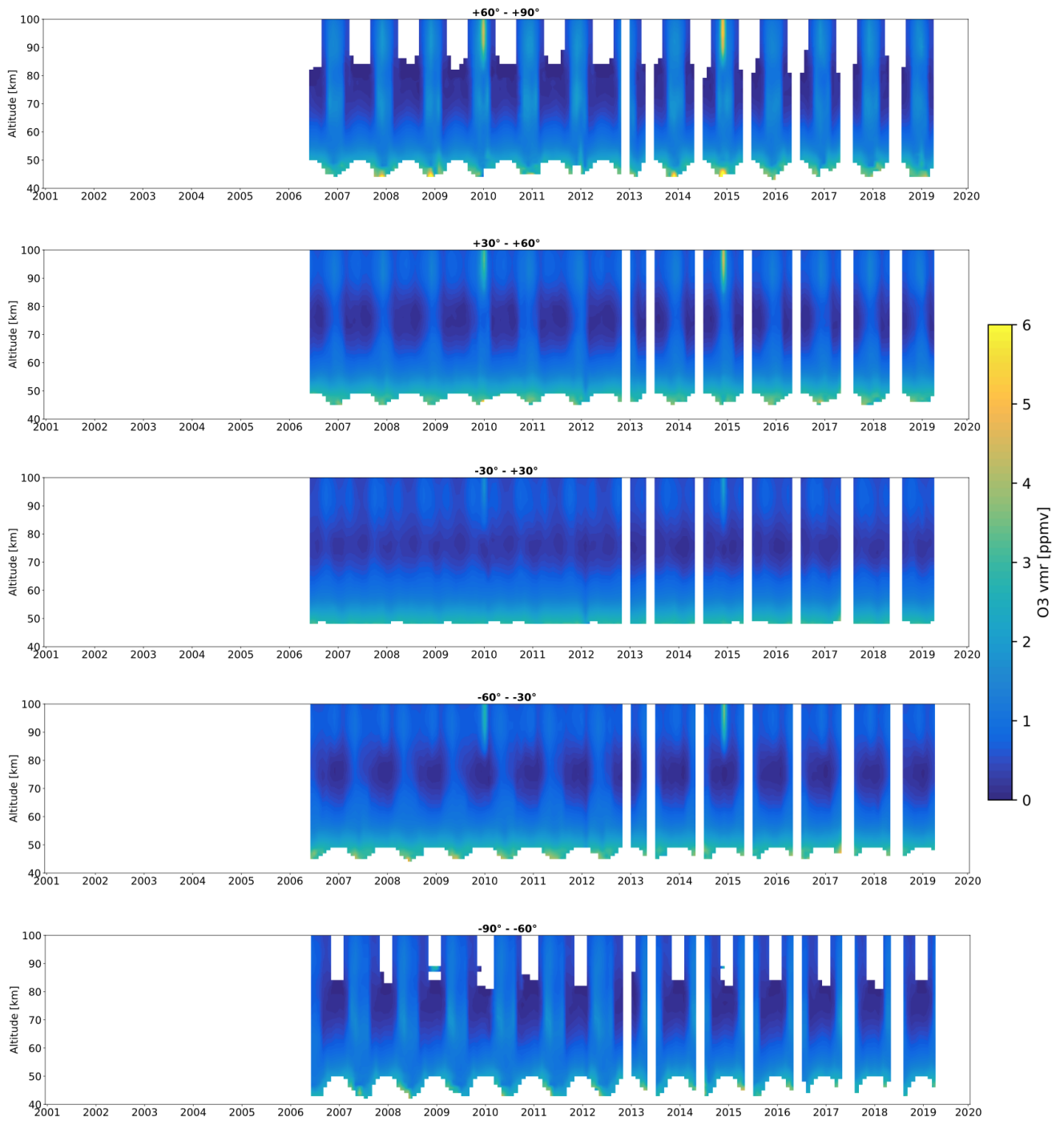


Figure A29. Time series of FM13 O₃ volume mixing ratios measured by SMR for different latitude bands. The white bands indicate periods during which the number of scans in the given latitude band is lower than 10. The ticks on the x-axis correspond to the beginning of each year.

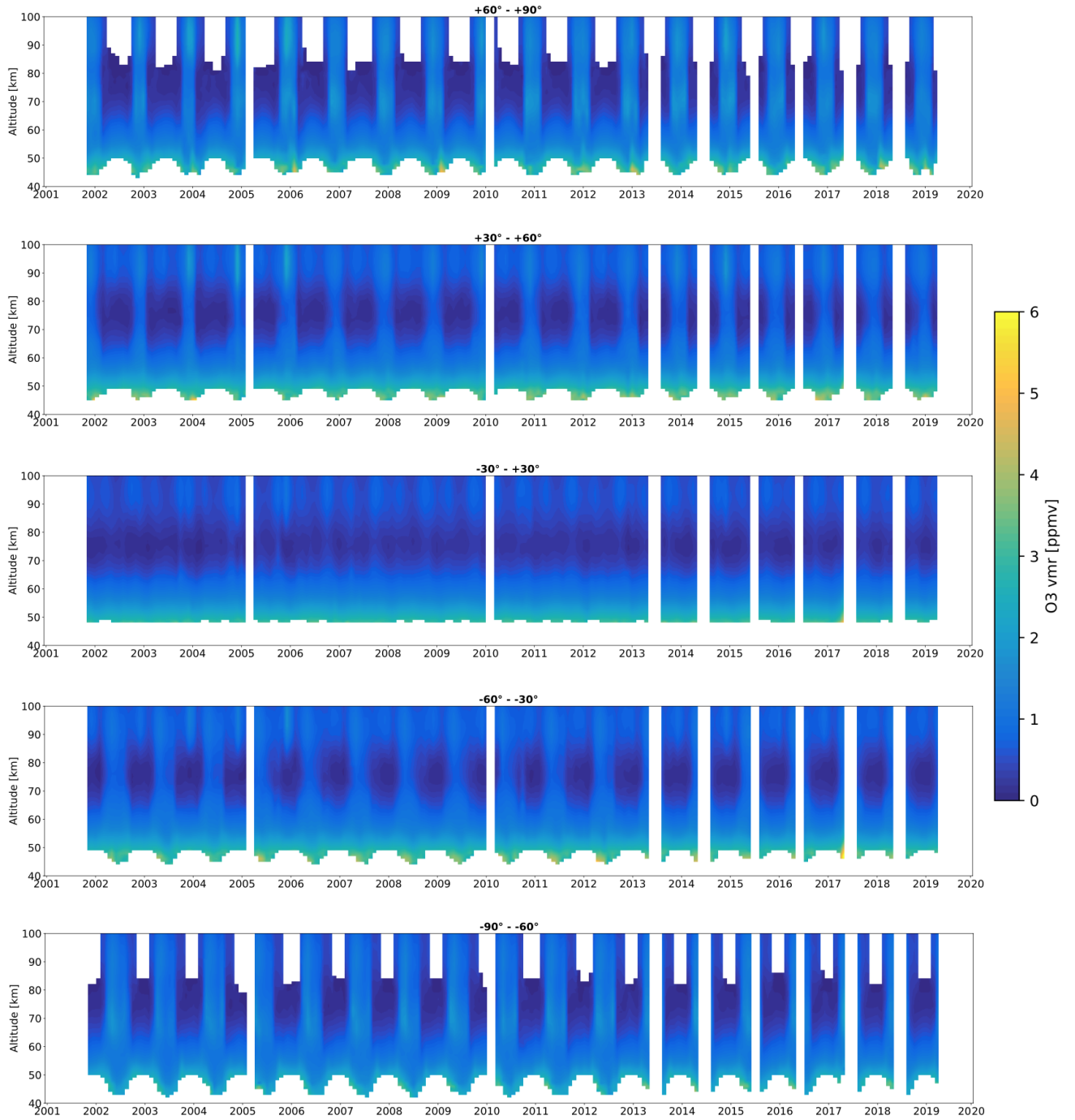


Figure A30. Time series of FM19 O₃ volume mixing ratios measured by SMR for different latitude bands. The white bands indicate periods during which the number of scans in the given latitude band is lower than 10. The ticks on the x-axis correspond to the beginning of each year.

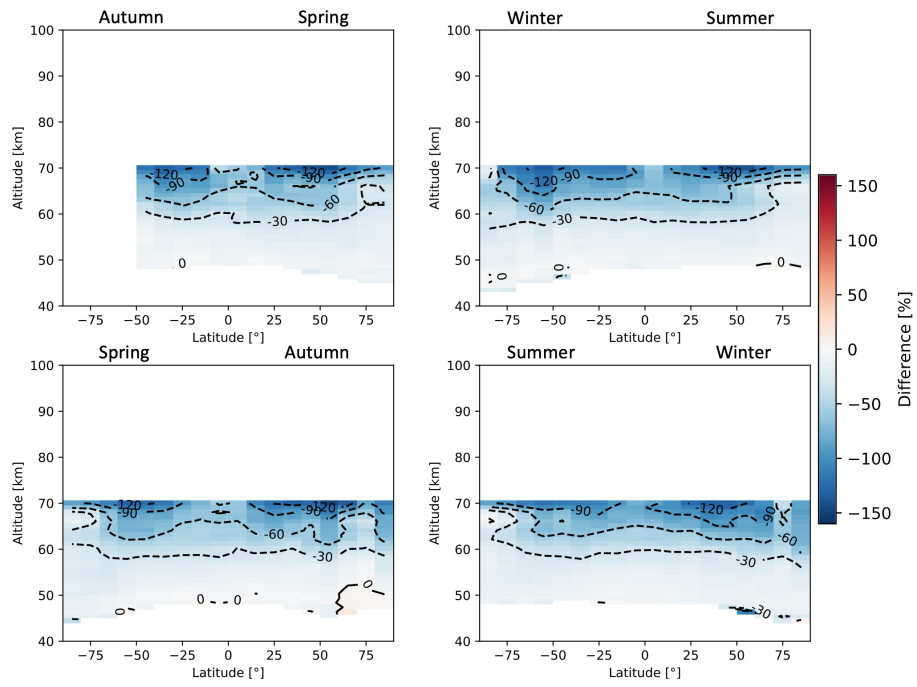


Figure A31. Seasonal zonal means of daytime O₃ FM13 SMR–MIPAS Nominal relative differences averaged over the time period indicated in Table 2. The seasons are intended as the time between solstice and equinox.

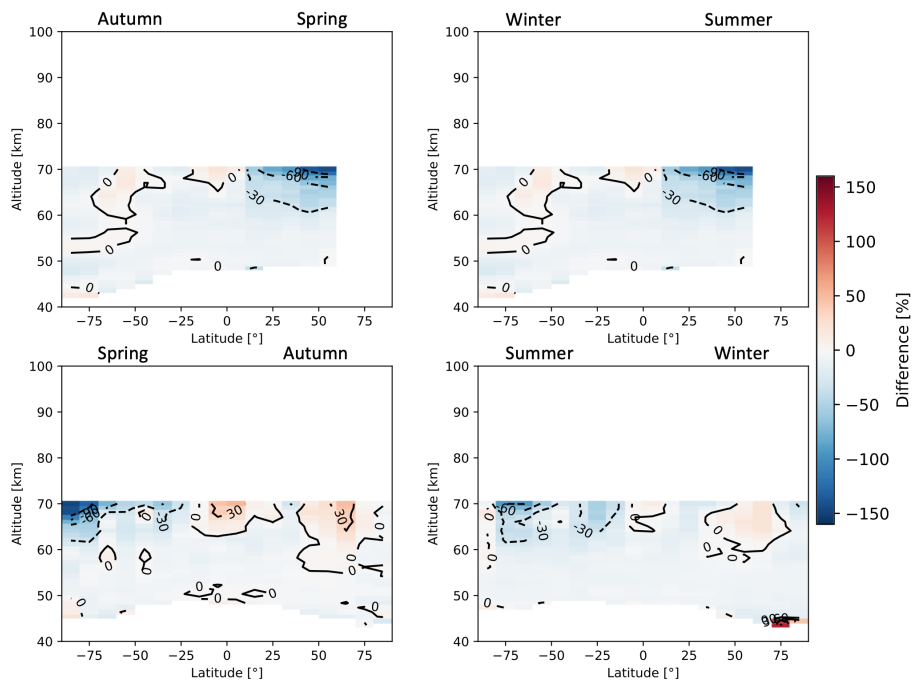


Figure A32. Seasonal zonal means of nighttime O₃ FM13 SMR–MIPAS Nominal relative differences averaged over the time period indicated in Table 2. The seasons are intended as the time between solstice and equinox.

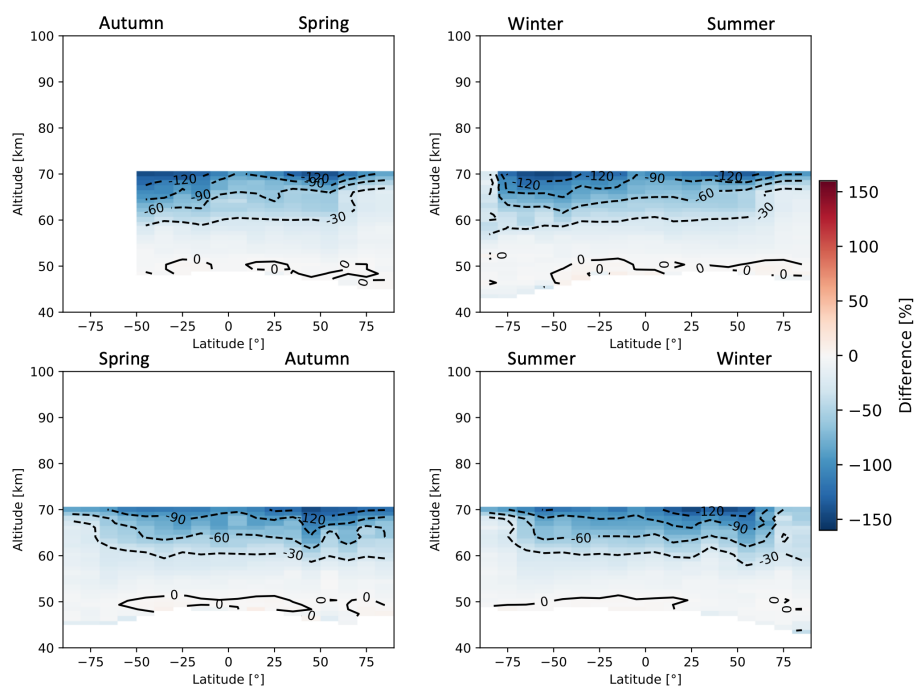


Figure A33. Seasonal zonal means of daytime O₃ FM19 SMR–MIPAS Nominal relative differences averaged over the time period indicated in Table 2. The seasons are intended as the time between solstice and equinox.

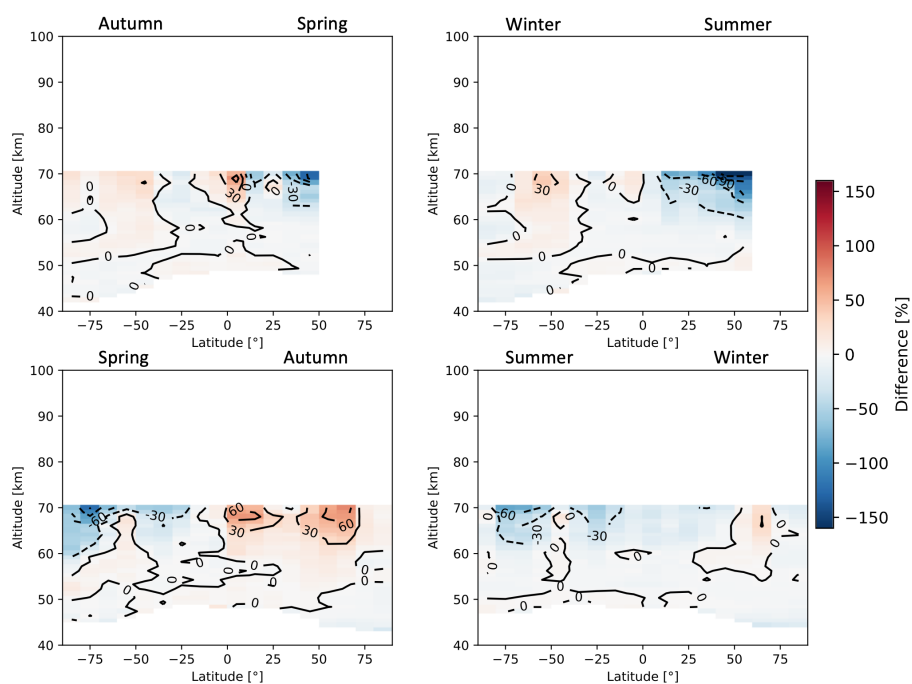


Figure A34. Seasonal zonal means of nighttime O₃ FM19 SMR–MIPAS Nominal relative differences averaged over the time period indicated in Table 2. The seasons are intended as the time between solstice and equinox.

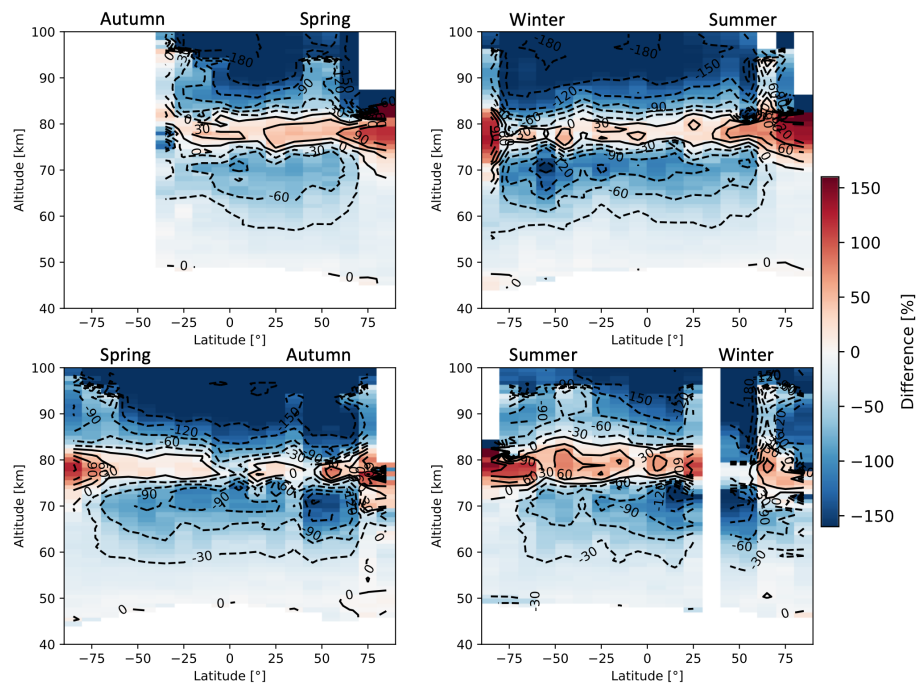


Figure A35. Seasonal zonal means of daytime O₃ FM13 SMR–MIPAS Middle Atmosphere relative differences averaged over the time period indicated in Table 2. The seasons are intended as the time between solstice and equinox.

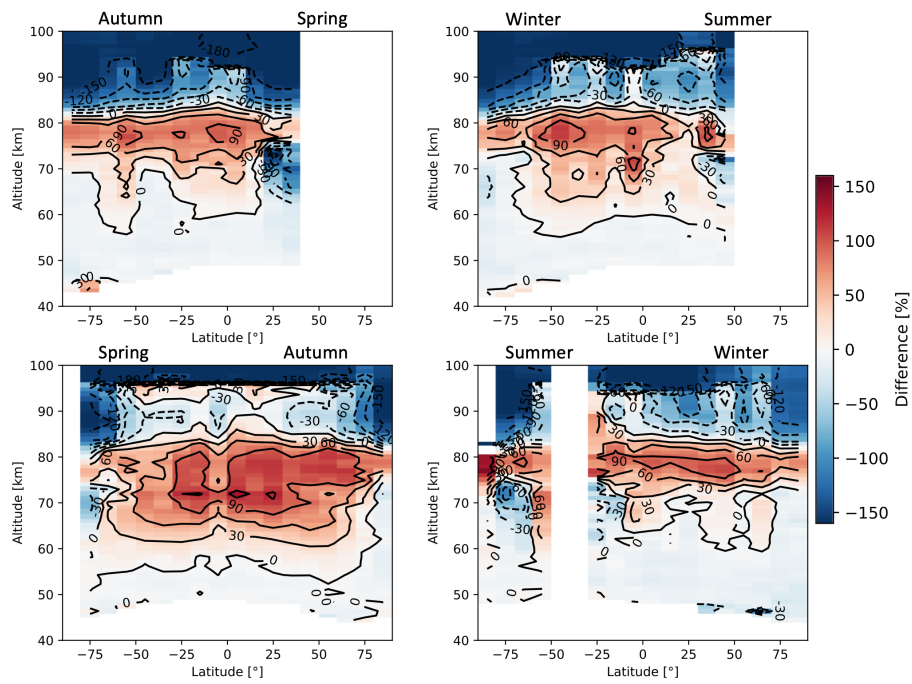


Figure A36. Seasonal zonal means of nighttime O₃ FM13 SMR-MIPAS Middle Atmosphere relative differences averaged over the time period indicated in Table 2. The seasons are intended as the time between solstice and equinox.

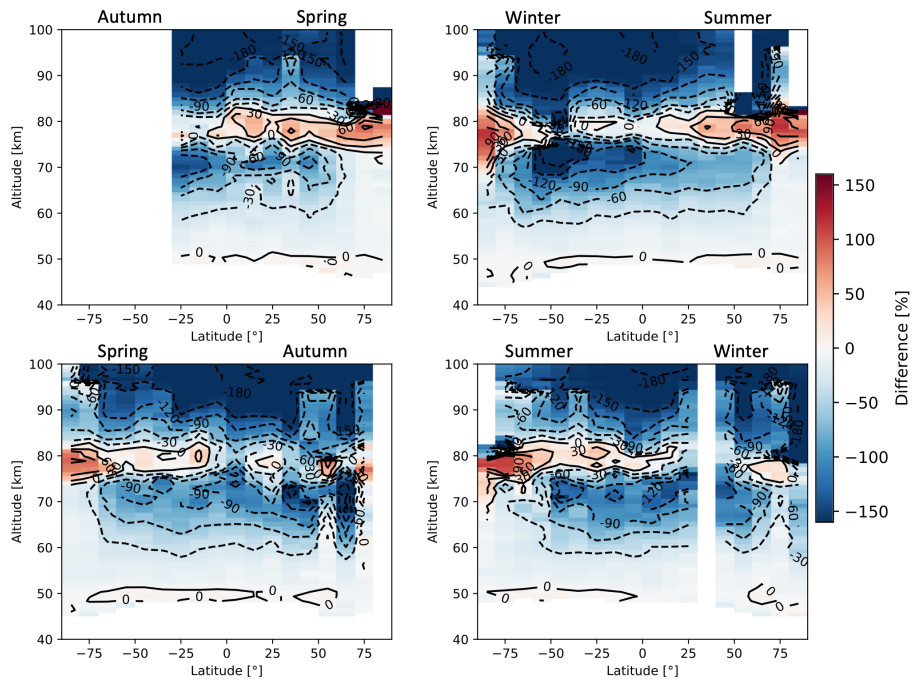


Figure A37. Seasonal zonal means of daytime O₃ FM19 SMR–MIPAS Middle Atmosphere relative differences averaged over the time period indicated in Table 2. The seasons are intended as the time between solstice and equinox.

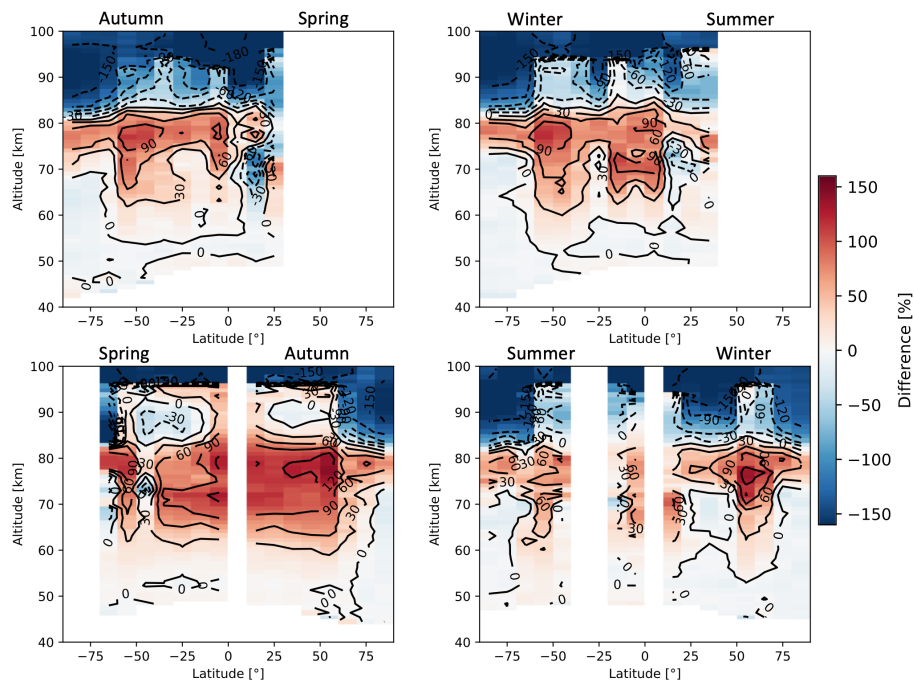


Figure A38. Seasonal zonal means of nighttime O₃ FM19 SMR-MIPAS Middle Atmosphere relative differences averaged over the time period indicated in Table 2. The seasons are intended as the time between solstice and equinox.

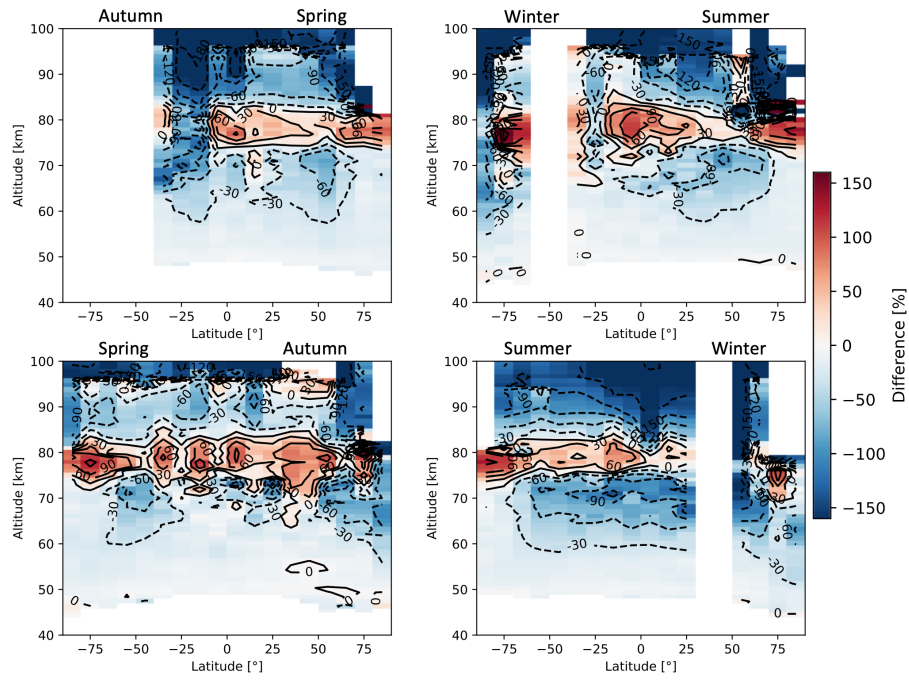


Figure A39. Seasonal zonal means of daytime O₃ FM13 SMR–MIPAS Upper Atmosphere relative differences averaged over the time period indicated in Table 2. The seasons are intended as the time between solstice and equinox.

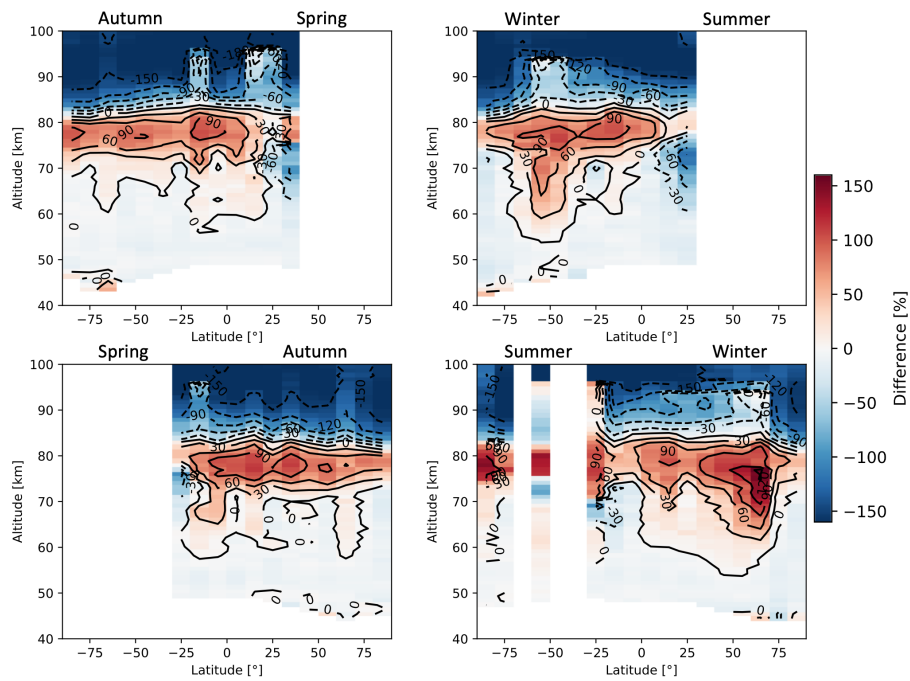


Figure A40. Seasonal zonal means of nighttime O₃ FM13 SMR-MIPAS Upper Atmosphere relative differences averaged over the time period indicated in Table 2. The seasons are intended as the time between solstice and equinox.

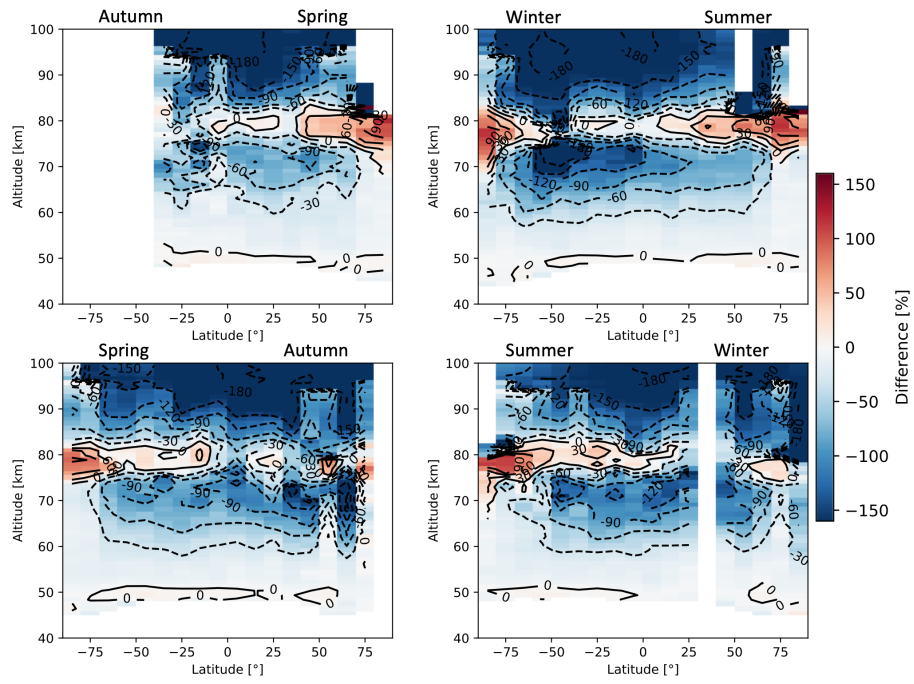


Figure A41. Seasonal zonal means of daytime O₃ FM19 SMR–MIPAS Upper Atmosphere relative differences averaged over the time period indicated in Table 2. The seasons are intended as the time between solstice and equinox.

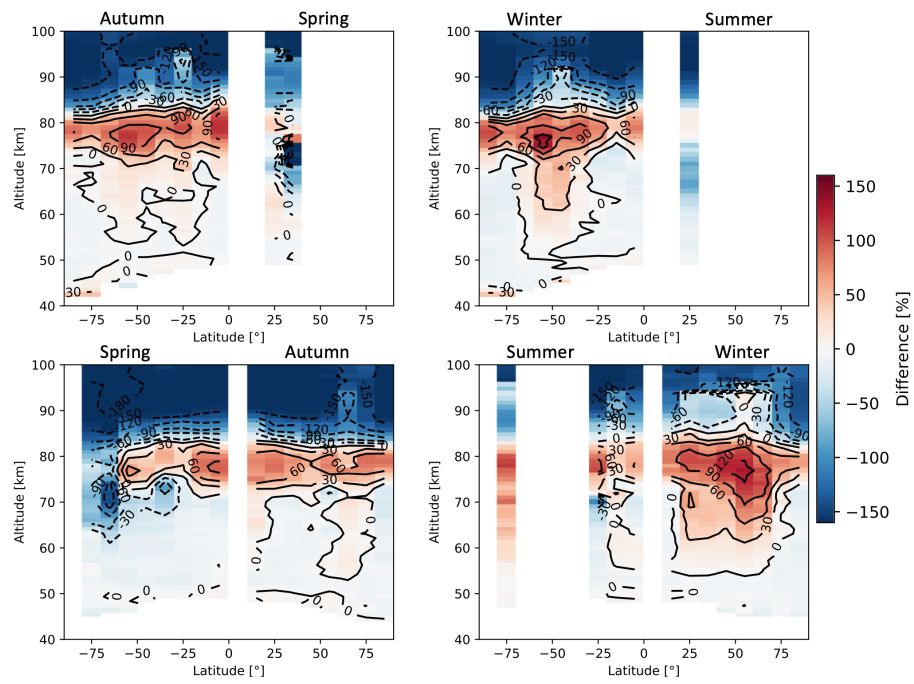


Figure A42. Seasonal zonal means of nighttime O₃ FM19 SMR-MIPAS Upper Atmosphere relative differences averaged over the time period indicated in Table 2. The seasons are intended as the time between solstice and equinox.

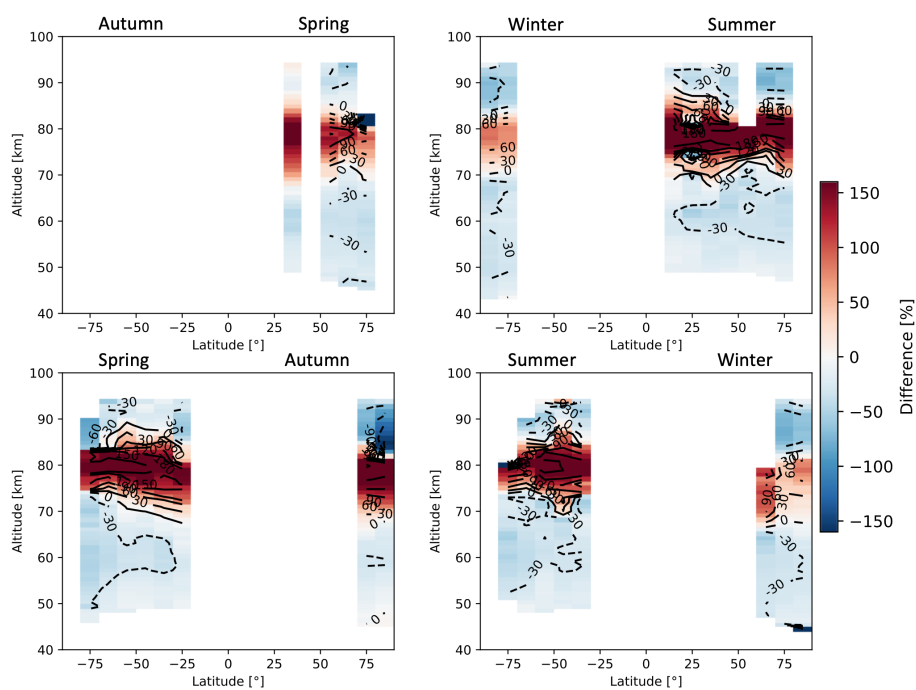


Figure A43. Seasonal zonal means of daytime O₃ FM13 SMR–ACE relative differences averaged over the time period between February 2004 and April 2019. The seasons are intended as the time between solstice and equinox.

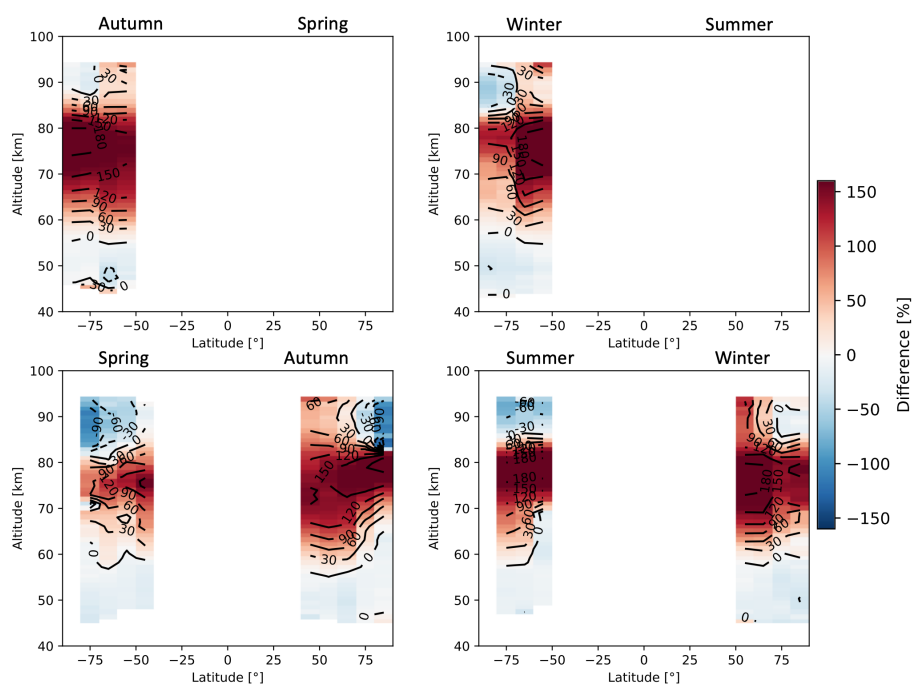


Figure A44. Seasonal zonal means of nighttime O₃ FM13 SMR–ACE relative differences averaged over the time period between February 2004 and April 2019. The seasons are intended as the time between solstice and equinox.

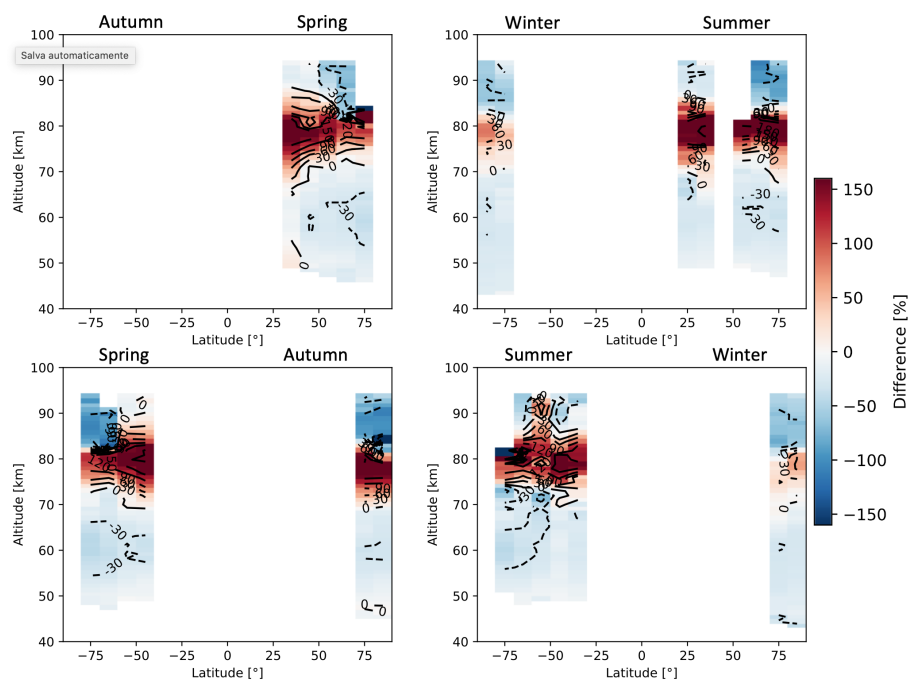


Figure A45. Seasonal zonal means of daylight O₃ FM19 SMR–ACE relative differences averaged over the time period between February 2004 and April 2019. The seasons are intended as the time between solstice and equinox.

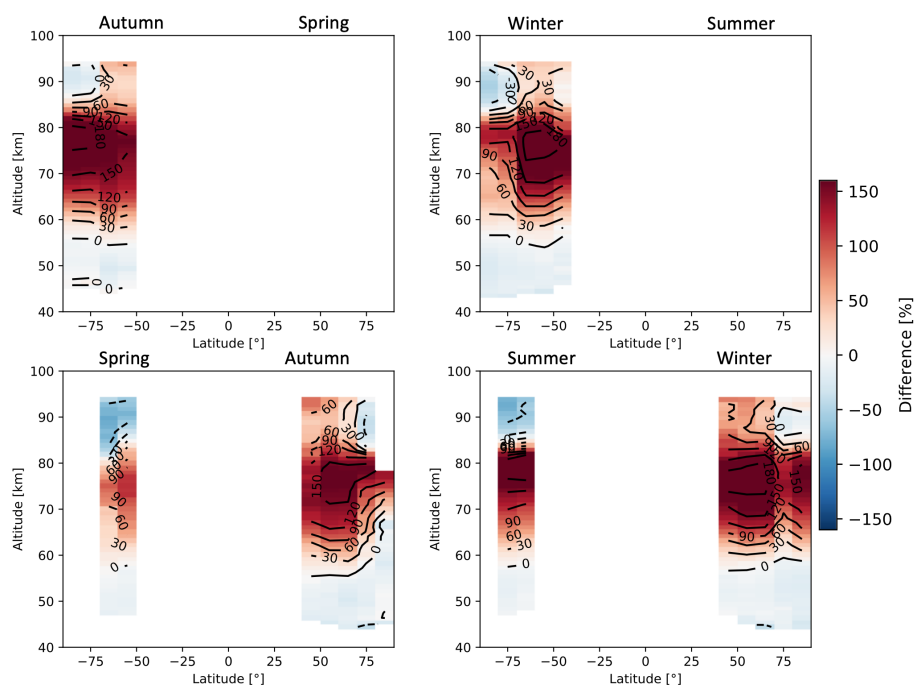


Figure A46. Seasonal zonal means of nighttime O₃ FM19 SMR-ACE relative differences averaged over the time period between February 2004 and April 2019. The seasons are intended as the time between solstice and equinox.

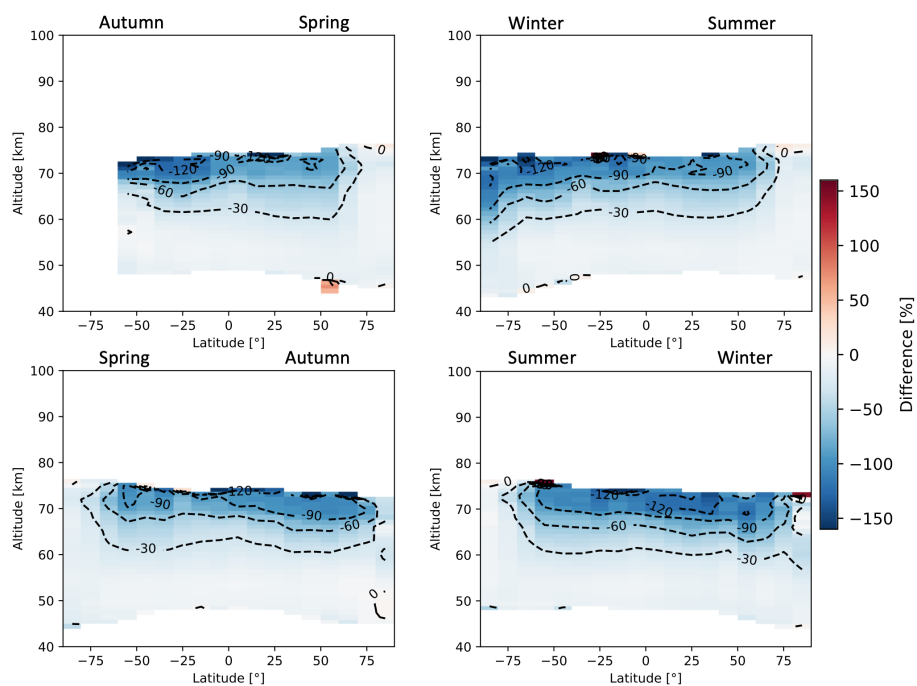


Figure A47. Seasonal zonal means of daytime O₃ FM13 SMR–MLS relative differences averaged over the time period between July 2004 and April 2019. The seasons are intended as the time between solstice and equinox.

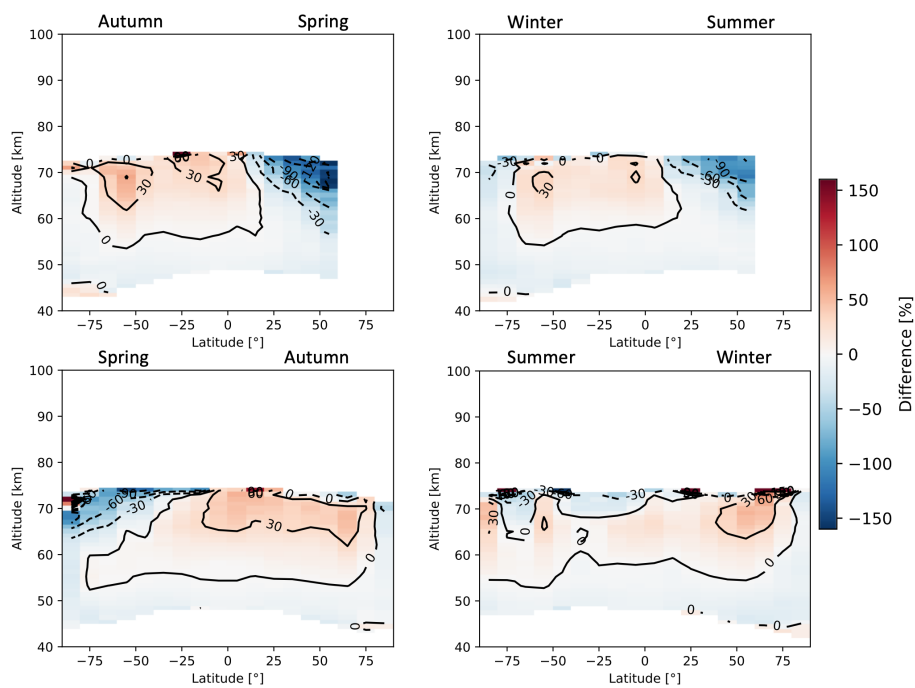


Figure A48. Seasonal zonal means of nighttime O₃ FM13 SMR–MLS relative differences averaged over the time period between July 2004 and April 2019. The seasons are intended as the time between solstice and equinox.

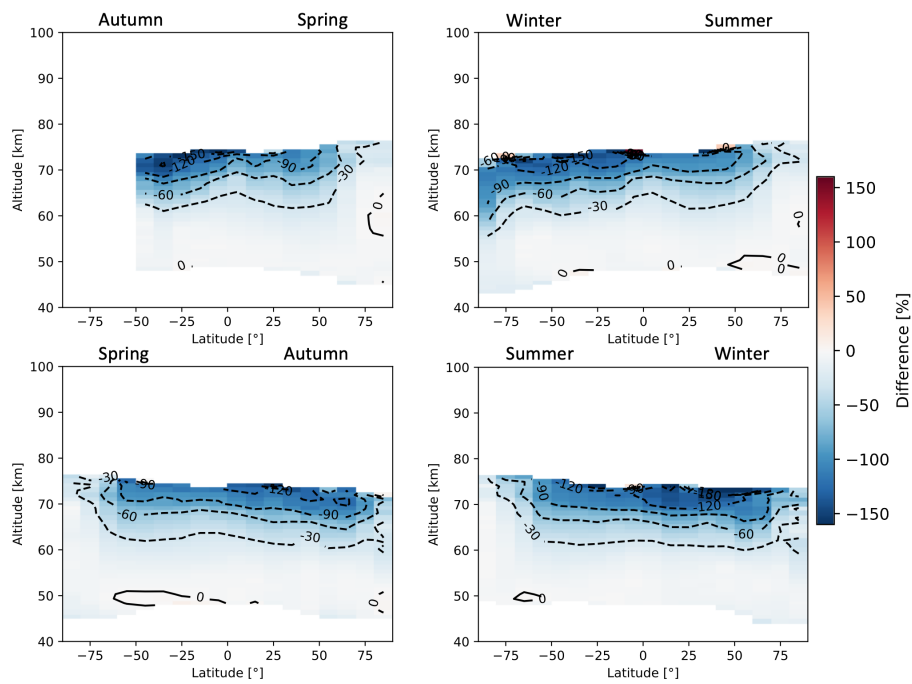


Figure A49. Seasonal zonal means of daytime O₃ FM19 SMR–MLS relative differences averaged over the time period between July 2004 and April 2019. The seasons are intended as the time between solstice and equinox.

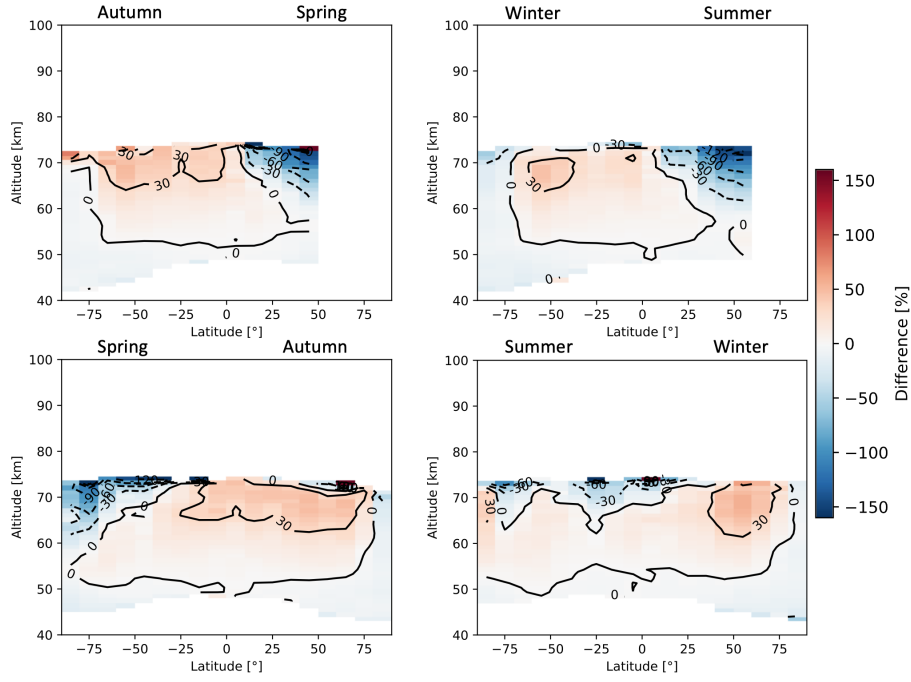


Figure A50. Seasonal zonal means of nighttime O₃ FM19 SMR–MLS relative differences averaged over the time period between July 2004 and April 2019. The seasons are intended as the time between solstice and equinox.

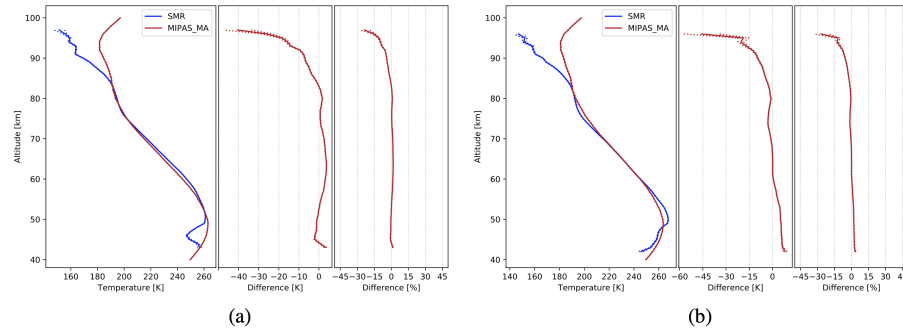


Figure A51. Comparison of SMR Temperatures, from FM13 (a) and FM19 (b), with the ones from MIPAS Middle Atmosphere Mode retrievals. The data plotted are global averages over the whole time periods indicated in Table 2. Figures characteristics are the same as in Figure 6.

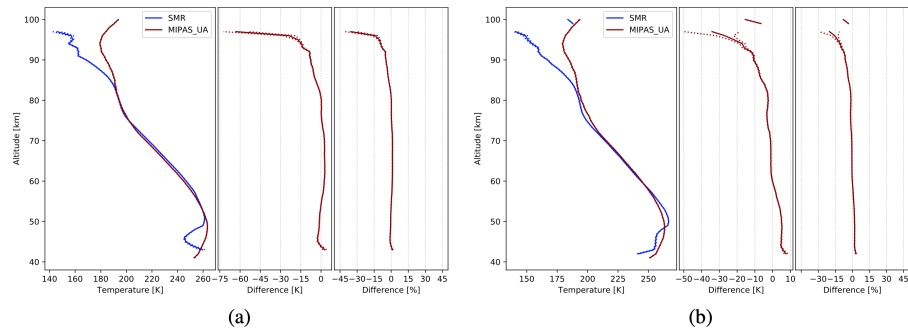


Figure A52. Comparison of SMR Temperatures, from FM13 (a) and FM19 (b), with the ones from MIPAS Upper Atmosphere Mode retrievals. The data plotted are global averages over the whole time periods indicated in Table 2. Figures characteristics are the same as in Figure 6.

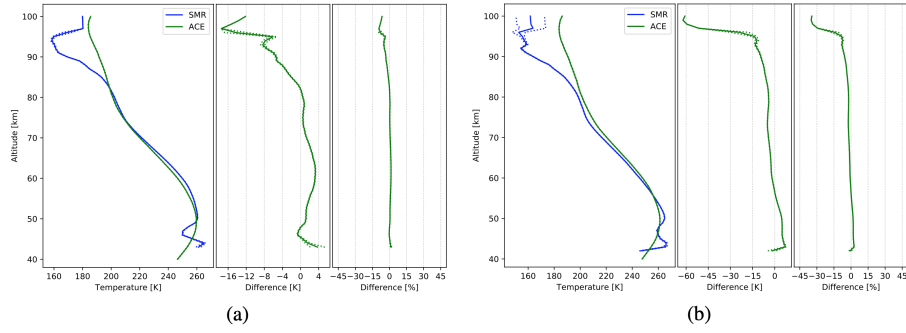


Figure A53. Comparison of SMR Temperatures, from FM13 (a) and FM19 (b), with the ones from ACE-FTS retrievals. The data plotted are global averages over the time period between February 2004 and April 2019. Figures characteristics are the same as in Figure 6.

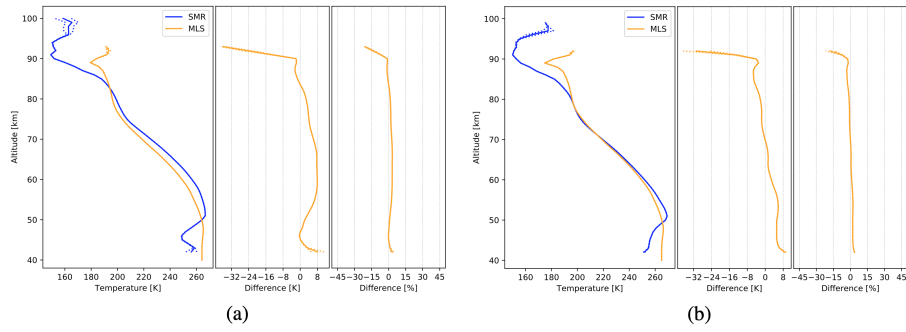


Figure A54. Comparison of SMR Temperatures, from FM13 (a) and FM19 (b), with the ones from MLS retrievals. The data plotted are global averages over the time period between July 2004 and April 2019. Figures characteristics are the same as in Figure 6.

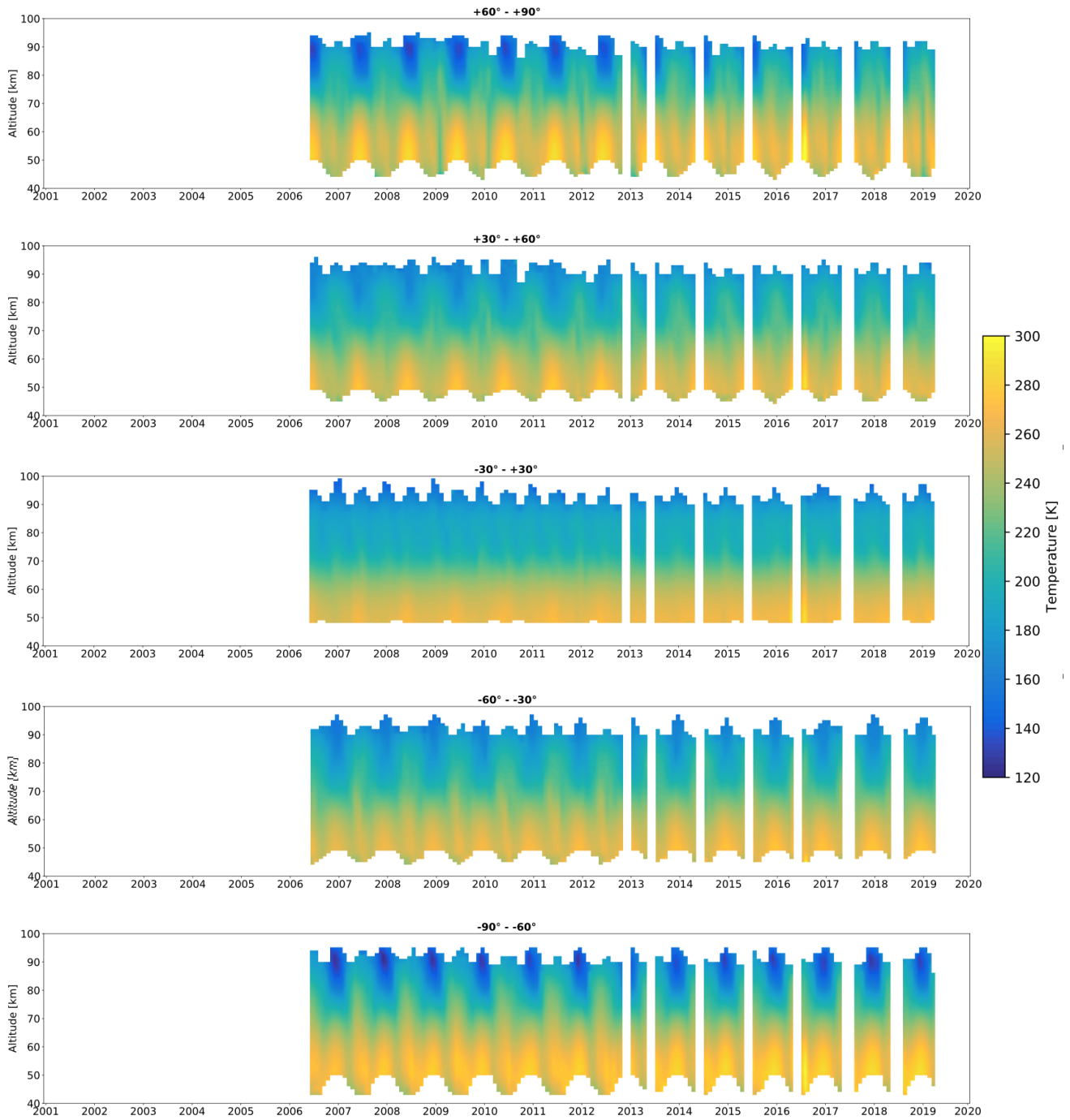


Figure A55. Time series of FM13 Temperature measured by SMR for different latitude bands. The white bands indicate periods during which the number of scans in the given latitude band is lower than 10. The ticks on the x-axis correspond to the beginning of each year.

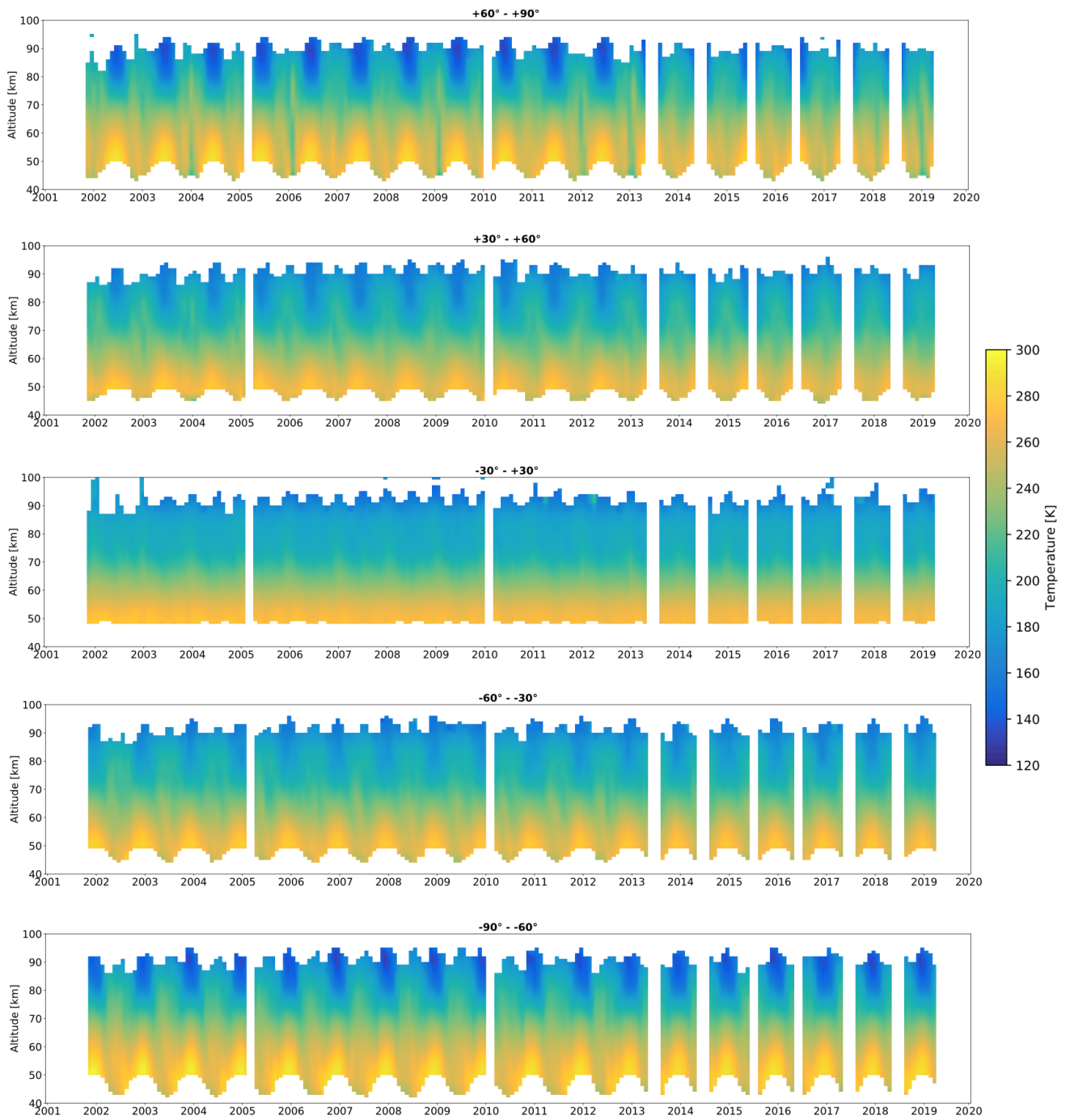


Figure A56. Time series of FM19 Temperature measured by SMR for different latitude bands. The white bands indicate periods during which the number of scans in the given latitude band is lower than 10. The ticks on the x-axis correspond to the beginning of each year.

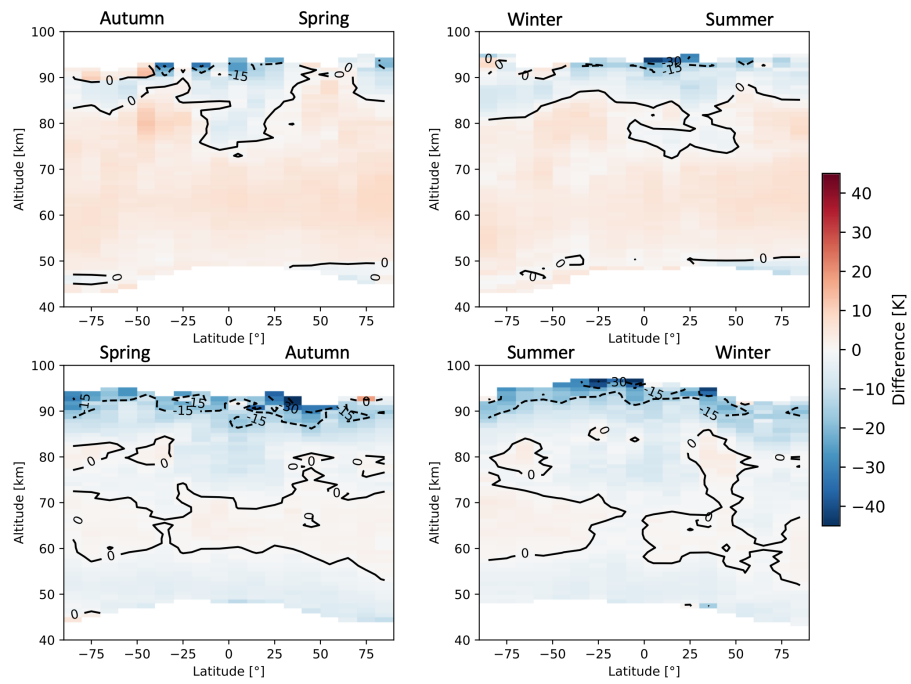


Figure A57. Seasonal zonal means of Temperature FM13 SMR–MIPAS Middle Atmosphere absolute differences averaged over the time period indicated in Table 2. The seasons are intended as the time between solstice and equinox.

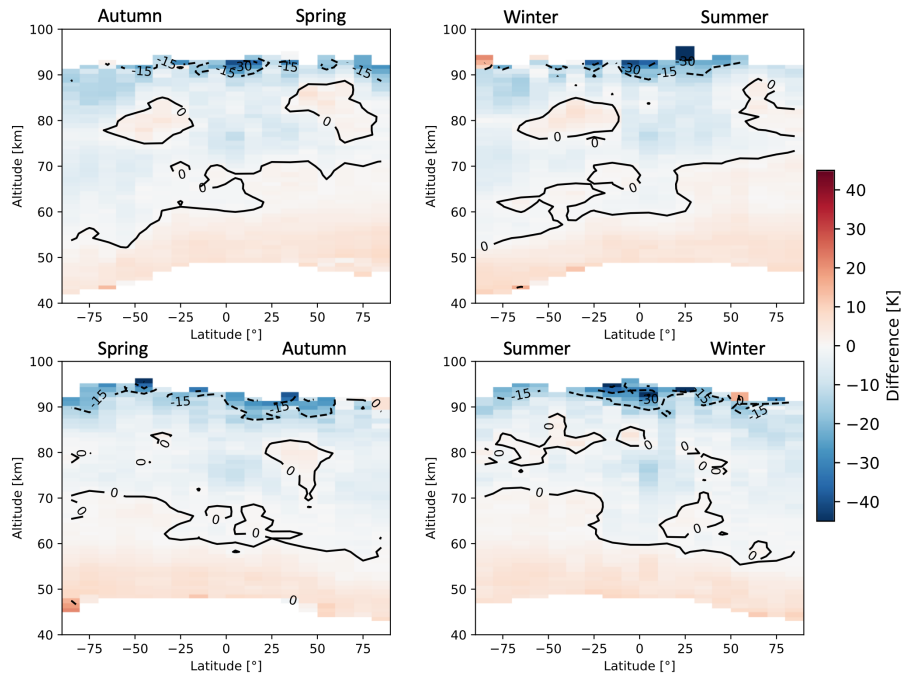


Figure A58. Seasonal zonal means of Temperature FM19 SMR–MIPAS Middle Atmosphere absolute differences averaged over the time period indicated in Table 2. The seasons are intended as the time between solstice and equinox.

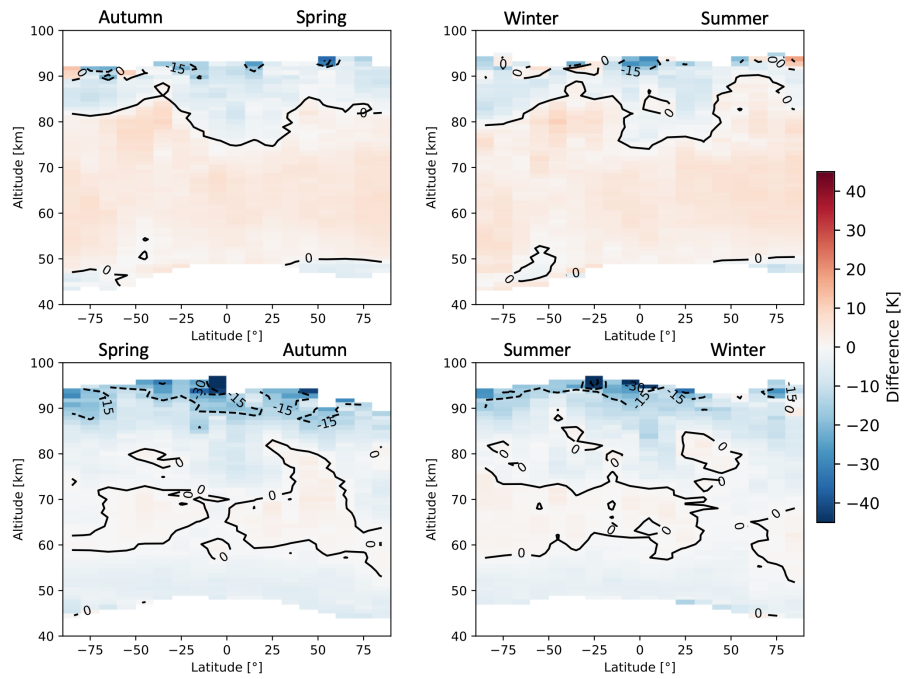


Figure A59. Seasonal zonal means of Temperature FM13 SMR–MIPAS Upper Atmosphere absolute differences averaged over the time period indicated in Table 2. The seasons are intended as the time between solstice and equinox.

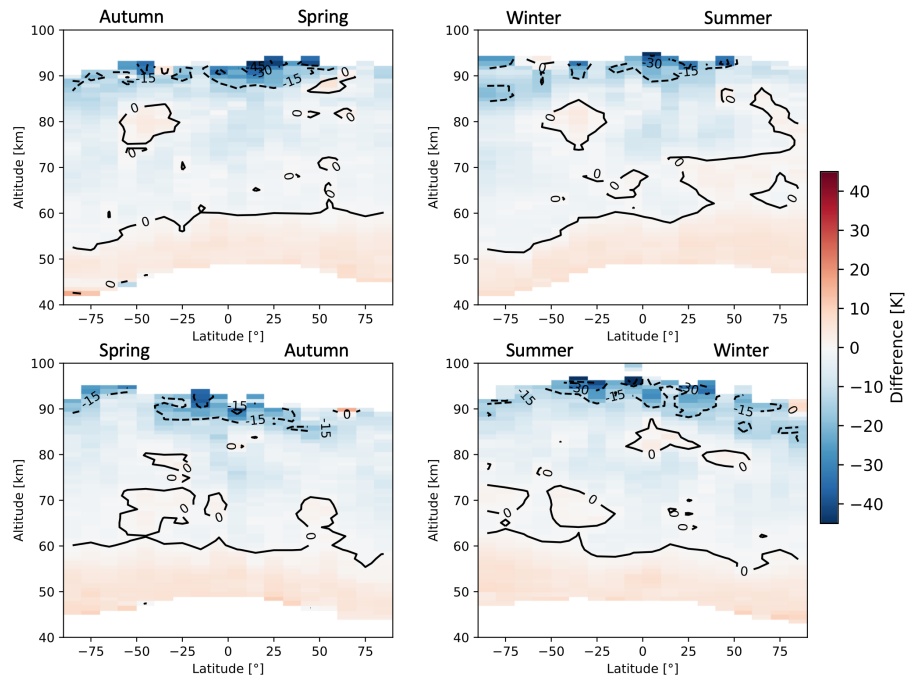


Figure A60. Seasonal zonal means of Temperature FM19 SMR-MIPAS Upper Atmosphere absolute differences averaged over the time period indicated in Table 2. The seasons are intended as the time between solstice and equinox.

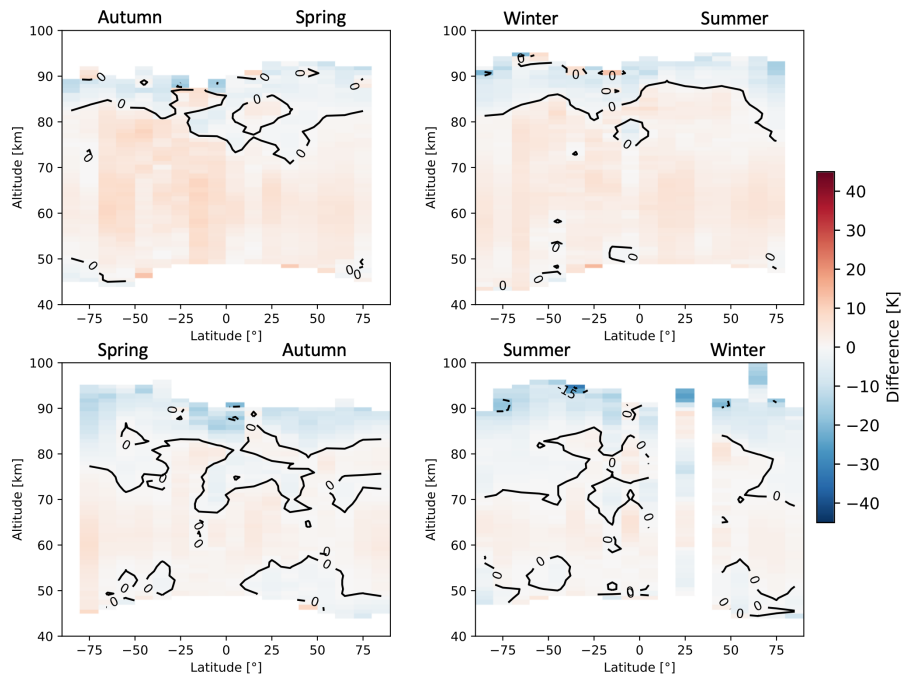


Figure A61. Seasonal zonal means of Temperature FM13 SMR–ACE absolute differences averaged over the time period between February 2004 and April 2019. The seasons are intended as the time between solstice and equinox.

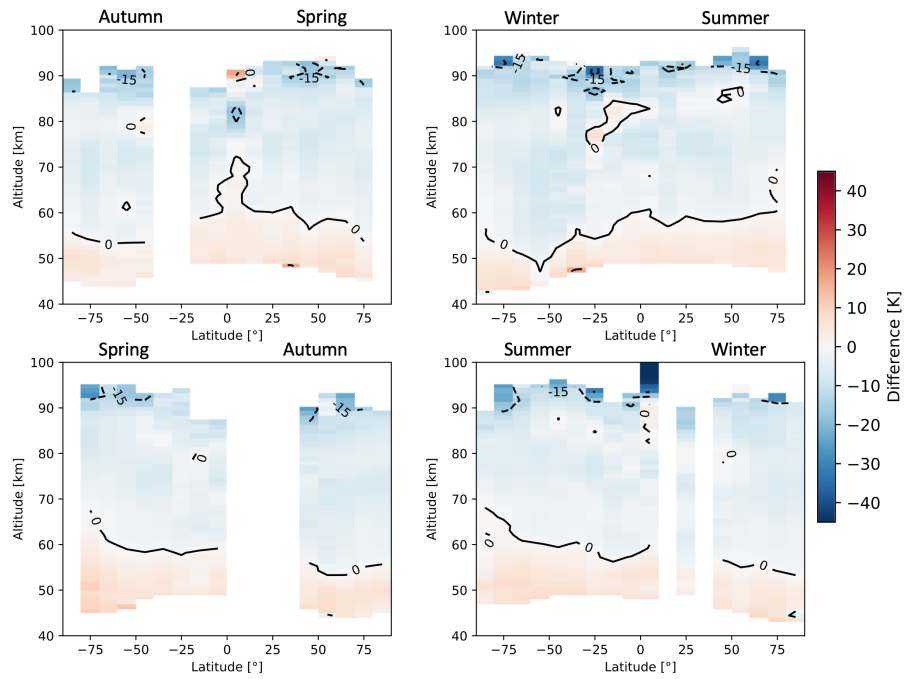


Figure A62. Seasonal zonal means of Temperature FM19 SMR–ACE absolute differences averaged over the time period between February 2004 and April 2019. The seasons are intended as the time between solstice and equinox.

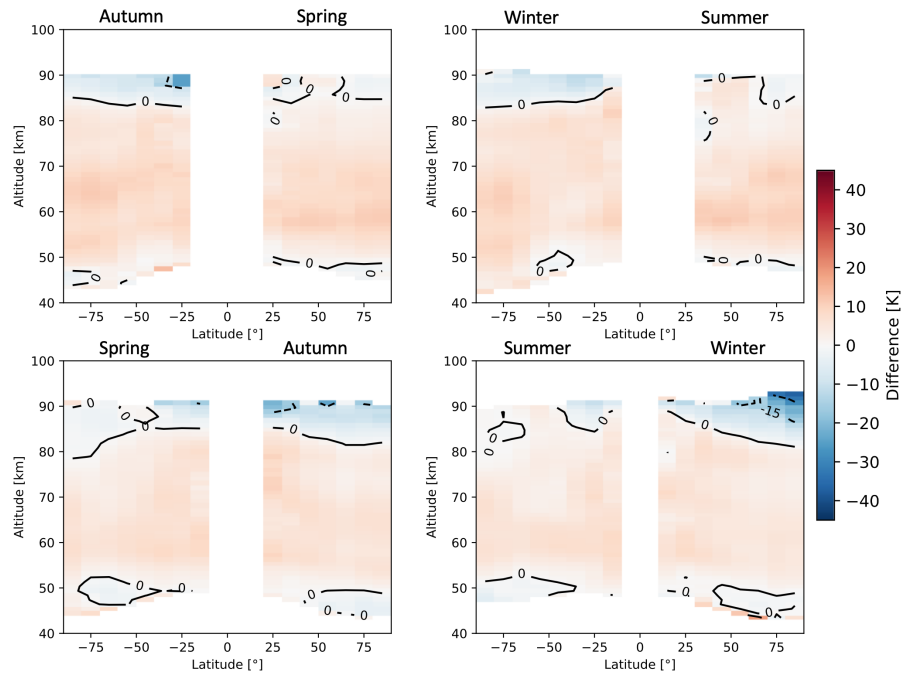


Figure A63. Seasonal zonal means of Temperature FM13 SMR–MLS absolute differences averaged over the time period between July 2004 and April 2019. The seasons are intended as the time between solstice and equinox.

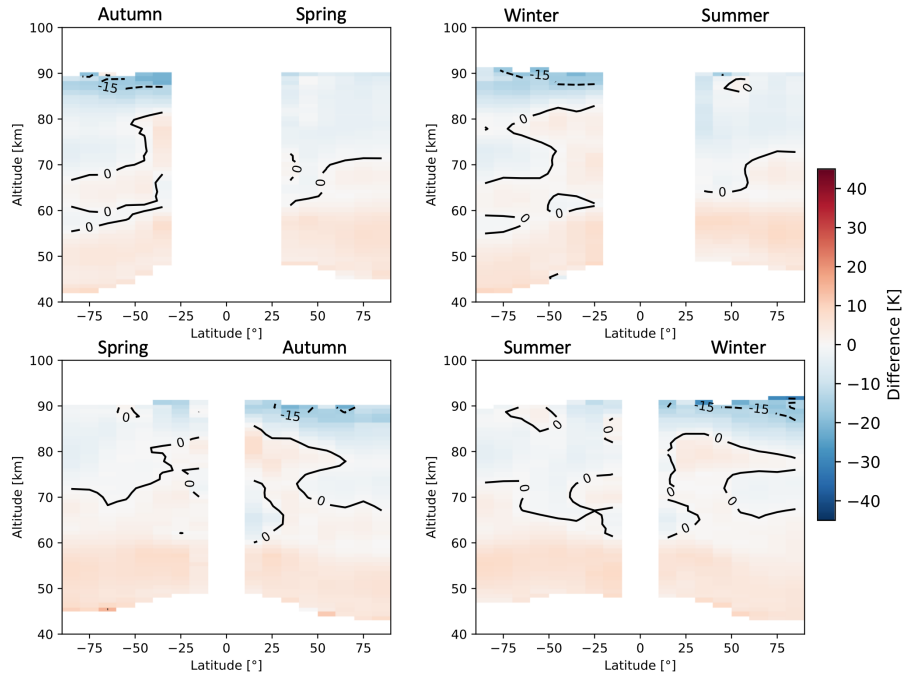


Figure A64. Seasonal zonal means of Temperature FM19 SMR–MLS absolute differences averaged over the time period between July 2004 and April 2019. The seasons are intended as the time between solstice and equinox.

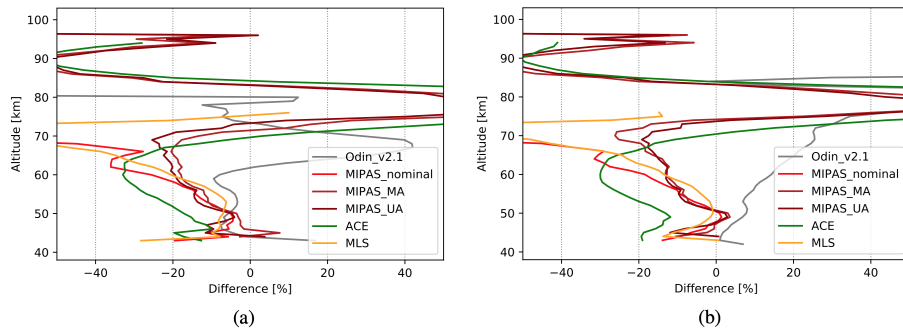


Figure A65. Summary of relative differences between SMR v3.0 O₃ daytime concentrations and SMR v2.1 ones as well as those retrieved by all other instruments considered in this study. For the sake of clarity, errors and labels are not shown, the latter being the same as in Figure 12. Panel a: FM13 comparison. Panel b: FM19 comparison.

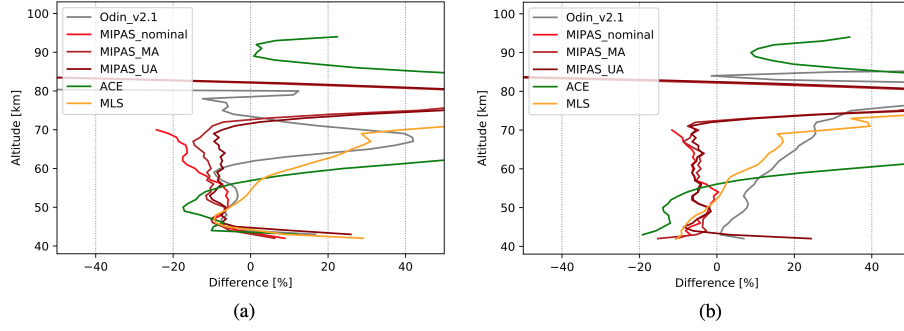


Figure A66. Summary of relative differences between SMR v3.0 O₃ nighttime concentrations and SMR v2.1 ones as well as those retrieved by all other instruments considered in this study. For the sake of clarity, errors and labels are not shown, the latter being the same as in Figure 12. Panel a: FM13 comparison. Panel b: FM19 comparison.

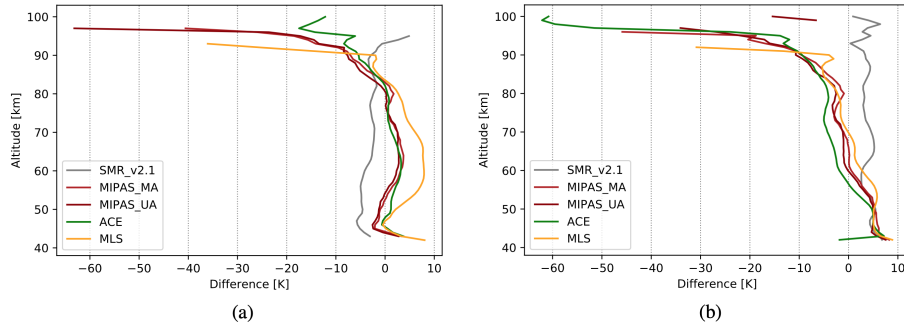


Figure A67. Summary of absolute differences between SMR v3.0 Temperatures and SMR v2.1 ones as well as those retrieved by all other instruments considered in this study. For the sake of clarity, errors are not shown. Panel a: FM13 comparison. Panel b: FM19 comparison.

Acknowledgements. The Chalmers team acknowledges support from the Swedish National Space Agency (Dnr 88/14 and 72/17). Odin is a Swedish-led satellite mission, and is also part of the European Space Agency's (ESA) third party mission programme. The reprocessing of the SMR data was supported by ESA (MesosphEO and Odin/SMR reprocessing projects). BF acknowledges support by the Spanish MCINN (ESP2017-87143-R) and EC FEDER funds. The Atmospheric Chemistry Experiment is a Canadian-led mission mainly supported by the

5 Canadian Space Agency. MLS research in Edinburgh was funded by NERC.

References

- Brasseur, G. and Solomon, S.: *Aeronomy of the Middle Atmosphere*, Springer, The Netherlands, 3rd edition, 2005.
- Charlton, A. and Polvani, L.: A New Look at Stratospheric Sudden Warmings. Part I: Climatology and Modeling Benchmarks, *J. Climate*, 20, 449–469, <https://doi.org/doi:10.1175/JCLI3996.1>, 2007.
- 5 Eriksson, P. and Urban, J.: Post launch characterisation of Odin-SMR sideband filter properties, Technical report, Chalmers University of Technology, 2006.
- Eriksson, P., Buehler, S., Davis, C., Emde, C., and Lemke, O.: ARTS, the atmospheric radiative transfer simulator, version 2, *Journal of Quantitative Spectroscopy and Radiative Transfer*, 112, 1551 – 1558, <https://doi.org/https://doi.org/10.1016/j.jqsrt.2011.03.001>, 2011.
- Feofilov, A. G., Kutepov, A. A., Pesnell, W. D., Goldberg, R. A., Marshall, B. T., Gordley, L. L., García-Comas, M., López-Puertas, M.,
10 Manuilova, R. O., Yankovsky, V. A., Petelina, S. V., and Russell III, J. M.: Daytime SABER/TIMED observations of water vapor in the mesosphere: retrieval approach and first results, *Atmospheric Chemistry and Physics*, 9, 8139–8158, <https://doi.org/10.5194/acp-9-8139-2009>, <https://www.atmos-chem-phys.net/9/8139/2009/>, 2009.
- Frisk, U., Hagström, M., Ala-Laurinaho, J., Andersson, S., Berges, J.-C., Chabaud, J.-P., Dahlgren, M., Emrich, A., Florén, H.-G., Florin, G., Fredrixon, M., Gaier, T., Haas, R., Hirvonen, T., Å. Hjalmarsson, Jakobsson, B., Jukkala, P., Kildal, P. S., Kollberg, E., Lassing, J.,
15 Lecacheux, A., Lehtinen, P., Lehto, A., Mallat, J., Marty, C., Michet, D., Narbonne, J., Nexon, M., Olberg, M., Olofsson, A. O. H., Olofsson, G., Origné, A., Petersson, M., Piironen, P., Pons, R., Pouliquen, D., Ristorcelli, I., Rosolen, C., Rouaix, G., Räisänen, A. V., Serra, G., Sjöberg, F., Stenmark, L., Torchinsky, S., Tuovinen, J., Ullberg, C., Vinterhav, E., Wadefalk, N., Zirath, H., Zimmermann, P., and Zimmermann, R.: The Odin satellite I. Radiometer design and test, *A&A*, 402, L27–L34, <https://doi.org/10.1051/0004-6361:20030335>, 2003.
- 20 Hamilton, K.: MIDDLE ATMOSPHERE I Semiannual Oscillation, in: *Encyclopedia of Atmospheric Sciences (Second Edition)*, pp. 26 – 29, Academic Press, Oxford, second edition edn., <https://doi.org/https://doi.org/10.1016/B978-0-12-382225-3.00233-4>, <http://www.sciencedirect.com/science/article/pii/B9780123822253002334>, 2015.
- Karlsson, B., Gumbel, J., Stegman, J., Lautier, N., Murtagh, D., and Team, O.: Studies of Noctilucent Clouds by the Odin Satellite, in: *Proceedings of the 35th COSPAR Scientific Assembly*, 35, 2004.
- 25 Kiefer, M. and Lossow, S.: MIPAS-IMK/IAA L2 Data ReadMe, FMI-TN-MesosphEO-WP4-003, Version 1.0, 2017.
- Livesey, N., Read, W., Wagner, P., Froidevaux, L., Lambert, A., Manney, G., Valle, L. M., Pumphrey, H., Santee, M., Schwartz, M., Wang, S., Fuller, R., Jarnot, R., Knosp, B., Martinez, E., and Lay, R.: Earth Observing System (EOS) Aura Microwave Limb Sounder (MLS) Version 4.2x Level 2 data quality and description document, Tech. Rep. D-33509 Rev. D, JPL, 2018.
- Lossow, S., Urban, J., Eriksson, P., Murtagh, D., and Gumbel, J.: Critical parameters for the retrieval of mesospheric wa-
30 ter vapour and temperature from Odin/SMR limb measurements at 557 GHz, *Advances in Space Research*, 40, 835–845, <https://doi.org/10.1016/j.asr.2007.05.026>, 2007.
- Lossow, S., Urban, J., Gumbel, J., Eriksson, P., and Murtagh, D.: Observations of the mesospheric semi-annual oscillation (MSAO) in water vapour by Odin/SMR, *Atmospheric Chemistry and Physics*, 8, 6527–6540, <https://doi.org/10.5194/acp-8-6527-2008>, <https://www.atmos-chem-phys.net/8/6527/2008/>, 2008.
- 35 Lossow, S., Urban, J., Schmidt, H., Marsh, D. R., Gumbel, J., Eriksson, P., and Murtagh, D.: Wintertime water vapor in the polar upper mesosphere and lower thermosphere: First satellite observations by Odin submillimeter radiometer, *Journal of Geophysical Research: Atmospheres*, 114, <https://doi.org/10.1029/2008JD011462>, 2009.

- Lossow, S., Khosrawi, F., Nedoluha, G. E., Azam, F., Bramstedt, K., Burrows, Dinelli, B. M., Eriksson, P., Espy, P. J., García-Comas, M., Gille, J. C., Kiefer, M., Noël, S., Raspollini, P., Read, W. G., Rosenlof, K. H., Rozanov, A., Sioris, C. E., Stiller, G. P., Walker, K. A., and Weigel, K.: The SPARC water vapour assessment II: comparison of annual, semi-annual and quasi-biennial variations in stratospheric and lower mesospheric water vapour observed from satellites, *Atmospheric Measurement Techniques*, 10, 1111–1137, <https://doi.org/10.5194/amt-10-1111-2017>, 2017.
- Lossow, S., Khosrawi, F., Kiefer, M., Walker, K. A., Bertaux, J.-L., Blanot, L., Russell, J. M., Remsberg, E. E., Gille, J. C., Sugita, T., Sioris, C. E., Dinelli, B. M., Papandrea, E., Raspollini, P., García-Comas, M., Stiller, G. P., von Clarmann, T., Dudhia, A., Read, W. G., Nedoluha, G. E., Damadeo, R. P., Zawodny, J. M., Weigel, K., Rozanov, A., Azam, F., Bramstedt, K., Noël, S., Burrows, J. P., Sagawa, H., Kasai, Y., Urban, J., Eriksson, P., Murtagh, D. P., Hervig, M. E., Högberg, C., Hurst, D. F., and Rosenlof, K. H.: The SPARC water vapour assessment II: profile-to-profile comparisons of stratospheric and lower mesospheric water vapour data sets obtained from satellites, *Atmospheric Measurement Techniques*, 12, 2693–2732, <https://doi.org/10.5194/amt-12-2693-2019>, <https://www.atmos-meas-tech.net/12/2693/2019/>, 2019.
- Montoux, N., Hauchecorne, A., Pommereau, J.-P., Lefèvre, F., Durr, G., Jones, R. L., Rozanov, A., Dhomse, S., Burrows, J. P., Morel, B., and Bencherif, H.: Evaluation of balloon and satellite water vapour measurements in the Southern tropical and subtropical UTLS during the HIBISCUS campaign, *Atmospheric Chemistry and Physics*, 9, 5299–5319, <https://doi.org/10.5194/acp-9-5299-2009>, <https://www.atmos-chem-phys.net/9/5299/2009/>, 2009.
- Munro, R. and Rodgers, C. D.: Latitudinal and season variations of water vapour in the middle atmosphere, *Geophysical Research Letters*, 21, 661–664, <https://doi.org/10.1029/94GL00183>, 1994.
- Murtagh, D., Skyman, A., Rydberg, B., and Eriksson, P.: Odin/SMR Diagnostic Dataset: Technical Note, Technical report, Chalmers University of Technology, Department of Space, Earth and Environment, <http://odin.rss.chalmers.se/#documents>, 2018.
- Nassar, R., Bernath, P. F., Boone, C. D., Manney, G. L., McLeod, S. D., Rinsland, C. P., Skelton, R., and Walker, K. A.: Stratospheric abundances of water and methane based on ACE-FTS measurements, *Geophysical Research Letters*, 32, <https://doi.org/10.1029/2005GL022383>, 2005.
- Oelhaf, H.: MIPAS Mission Plan, Issue 4, Version 3, ESA Technical Note ENVI-SPPA-EOPG-TN-07-0073, 2008.
- Pérot, K., Urban, J., and Murtagh, D.: Unusually strong nitric oxide descent in the Arctic middle atmosphere in early 2013 as observed by Odin/SMR, *Atmos. Chem. Phys.*, 14, 8009–8015, <https://doi.org/10.5194/acpd-14-3563-2014>, 2014.
- Randall, C., Rusch, D., Bevilacqua, R., Hoppel, K., Lumpe, J., Shettle, E., Thompson, E., Deaver, L., Zawodny, J., Kyrö, E., Johnson, B., Kelder, H., Dorokhov, V., König-Langlo, G., and Gil, M.: Validation of POAM III ozone: comparison with ozonesonde and satellite data, *J. Geophys. Res.*, 108, 4367, <https://doi.org/10.1029/2002JD002944>, 2003.
- Remsberg, E., Russell, J. M., Gordley, L. L., Gille, J. C., and Bailey, P. L.: Implications of the Stratospheric Water Vapor Distribution as Determined from the Nimbus 7 LIMS Experiment, *Journal of the Atmospheric Sciences*, 41, 2934–2948, [https://doi.org/10.1175/1520-0469\(1984\)041<2934:IOTSWV>2.0.CO;2](https://doi.org/10.1175/1520-0469(1984)041<2934:IOTSWV>2.0.CO;2), 1984.
- Rodgers, C.: Inverse methods for atmospheric sounding: Theory and practise, World Scientific Publishing, 1st edition, 2000.
- Rydberg, B., Eriksson, P., Kiviranta, J., Ringsby, J., Skyman, A., and Murtagh, D.: Odin/SMR Algorithm Theoretical Basis Document: Level 1 Processing, Technical Report, Chalmers University of Technology, Department of Space, Earth and Environment, <http://odin.rss.chalmers.se/#documents>, 2017.
- Schoeberl, M. and Newman, P.: MIDDLE ATMOSPHERE | Polar Vortex, in: *Encyclopedia of Atmospheric Sciences (Second Edition)*, pp. 12 – 17, Academic Press, Oxford, second edition edn., <https://doi.org/10.1016/B978-0-12-382225-3.00228-0>, 2015.

- Schoeberl, M., Douglass, A., Hilsenrath, E., Bhartia, P., Beer, R., Waters, J., Gunson, M., Froidevaux, L., Gille, J., Barnett, J., Levelt, P., and DeCola, P.: Overview of the EOS Aura Mission, *IEEE Trans. Geosci. Remote Sensing*, 44, 1066 – 1074, <https://doi.org/doi:10.1109/TGRS.2005.861950>, 2006.
- Sheese, P., Boone, C., and Walker, K.: Detecting physically unrealistic outliers in ACE-FTS atmospheric measurements, *Atmos. Meas. Tech.*, 8, 741–750, <https://doi.org/10.5194/amt-8-741-2015>, 2015.
- Sheese, P. E., Walker, K. A., Boone, C. D., Bernath, P. F., Froidevaux, L., Funke, B., Raspollini, P., and von Clarmann, T.: ACE-FTS ozone, water vapour, nitrous oxide, nitric acid, and carbon monoxide profile comparisons with MIPAS and MLS, *Journal of Quantitative Spectroscopy and Radiative Transfer*, 186, 63 – 80, <https://doi.org/10.1016/j.jqsrt.2016.06.026>, satellite Remote Sensing and Spectroscopy: Joint ACE-Odin Meeting, October 2015, 2017.
- 10 Sioris, C., Zou, J., McElroy, C., McLinden, C., and Vömel, H.: High vertical resolution water vapour profiles in the upper troposphere and lower stratosphere retrieved from MAESTRO solar occultation spectra, *Advances in Space Research*, 46, 642 – 650, <https://doi.org/https://doi.org/10.1016/j.asr.2010.04.040>, 2010.
- Urban, J., Lautié, N., Murtagh, D., Eriksson, P., Kasai, Y., Lossow, S., Dupuy, E., de La Noë, J., Frisk, U., Olberg, M., Flochmoën, E. L., and Ricaud, P.: Global observations of middle atmospheric water vapour by the Odin satellite: An overview, *Planetary and Space Science*, 55, 1093 – 1102, <https://doi.org/https://doi.org/10.1016/j.pss.2006.11.021>, highlights in *Planetary Science*, 2007.
- 15 Vignon, E. and Mitchell, D.: The stratopause evolution during different types of sudden stratospheric warming event, *Clim Dyn*, 44, <https://doi.org/10.1007/s00382-014-2292-4>, 2015.
- Waters, J. W., Froidevaux, L., Harwood, R. S., Jarnot, R. F., Pickett, H. M., Read, W. G., Siegel, P. H., Cofield, R. E., Filipiak, M. J., Flower, D. A., Holden, J. R., Lau, G. K., Livesey, N. J., Manney, G. L., Pumphrey, H. C., Santee, M. L., Wu, D. L., Cuddy, D. T., Lay, R. R., Loo, M. S., Perun, V. S., Schwartz, M. J., Stek, P. C., Thurstans, R. P., Boyles, M. A., Chandra, K. M., Chavez, M. C., Gun-Shing Chen, Chudasama, B. V., Dodge, R., Fuller, R. A., Girard, M. A., Jiang, J. H., Yibo Jiang, Knosp, B. W., LaBelle, R. C., Lam, J. C., Lee, K. A., Miller, D., Oswald, J. E., Patel, N. C., Pukala, D. M., Quintero, O., Scaff, D. M., Van Snyder, W., Tope, M. C., Wagner, P. A., and Walch, M. J.: The Earth observing system microwave limb sounder (EOS MLS) on the aura Satellite, *IEEE Transactions on Geoscience and Remote Sensing*, 44, 1075–1092, 2006.
- 20 Weigel, K., Rozanov, A., Azam, F., Bramstedt, K., Damadeo, R., Eichmann, K.-U., Gebhardt, C., Hurst, D., Kraemer, M., Lossow, S., Read, W., Spelten, N., Stiller, G. P., Walker, K. A., Weber, M., Bovensmann, H., and Burrows, J. P.: UTLS water vapour from SCIAMACHY limb measurements V3.01 (2002–2012), *Atmospheric Measurement Techniques*, 9, 133–158, <https://doi.org/10.5194/amt-9-133-2016>, <https://www.atmos-meas-tech.net/9/133/2016/>, 2016.
- 30 Wetzel, G., Oelhaf, H., Berthet, G., Bracher, A., Cornacchia, C., Feist, D. G., Fischer, H., Fix, A., Iarlori, M., Kleinert, A., Lengel, A., Milz, M., Mona, L., Müller, S. C., Ovarlez, J., Pappalardo, G., Piccolo, C., Raspollini, P., Renard, J.-B., Rizi, V., Rohs, S., Schiller, C., Stiller, G., Weber, M., and Zhang, G.: Validation of MIPAS-ENVISAT H₂O operational data collected between July 2002 and March 2004, *Atmospheric Chemistry and Physics*, 13, 5791–5811, <https://doi.org/10.5194/acp-13-5791-2013>, <https://www.atmos-chem-phys.net/13/5791/2013/>, 2013.